Publication Year	2016
Acceptance in OA@INAF	2020-05-31T16:59:29Z
Title	Planck 2015 results. XXV. Diffuse low-frequency Galactic foregrounds
Authors	Planck Collaboration; Ade, P. A. R.; Aghanim, N.; Alves, M. I. R.; Arnaud, M.; et al.
DOI	10.1051/0004-6361/201526803
Handle	http://hdl.handle.net/20.500.12386/25310
Journal	ASTRONOMY & ASTROPHYSICS
Number	594

Publication Year	2016
Acceptance in OA@INAF	2020-05-31T16:59:29Z
Title	Planck 2015 results. XXV. Diffuse low-frequency Galactic foregrounds
Authors	Planck Collaboration; Ade, P. A. R.; Aghanim, N.; Alves, M. I. R.; Arnaud, M.; et al.
DOI	10.1051/0004-6361/201526803
Handle	http://hdl.handle.net/20.500.12386/25310
Journal	ASTRONOMY & ASTROPHYSICS
Number	594

A&A 594, A25 (2016)
DOI: 10.1051/0004-6361/201526803
© ESO 2016

Planck 2015 results

Astronomy & Astrophysics
Special feature

Planck 2015 results

XXV. Diffuse low-frequency Galactic foregrounds

Planck Collaboration: P. A. R. Ade[95], N. Aghanim[64], M. I. R. Alves[105,11,64], M. Arnaud[79], M. Ashdown[75,6], J. Aumont[64], C. Baccigalupi[93], A. J. Banday[105,11], R. B. Barreiro[70], J. G. Bartlett[1,72], N. Bartolo[33,71], E. Battaner[107,108], K. Benabed[65,104], A. Benoît[62], A. Benoit-Lévy[27,65,104], J.-P. Bernard[105,11], M. Bersanelli[36,52], P. Bielewicz[89,11,93], J. J. Bock[72,13], A. Bonaldi[73], L. Bonavera[70], J. R. Bond[10], J. Borrill[16,99], F. R. Bouchet[65,97], F. Boulanger[64], M. Bucher[1], C. Burigana[51,34,53], R. C. Butler[51], E. Calabrese[101], J.-F. Cardoso[80,1,65], A. Catalano[81,78], A. Challinor[67,75,14], A. Chamballu[79,18,64], R.-R. Chary[61], H. C. Chiang[30,7], P. R. Christensen[90,39], S. Colombi[65,104], L. P. L. Colombo[26,72], C. Combet[81], F. Couchot[77], A. Coulais[78], B. P. Crill[72,13], A. Curto[70,6,75], F. Cuttaia[51], L. Danese[93], R. D. Davies[73], R. J. Davis[73], P. de Bernardis[35], A. de Rosa[51], G. de Zotti[48,93], J. Delabrouille[1], J.-M. Delouis[65,104], F.-X. Désert[58], C. Dickinson[73,*], J. M. Diego[70], H. Dole[64,63], S. Donzelli[52], O. Doré[72,13], M. Douspis[64], A. Ducout[65,60], X. Dupac[41], G. Efstathiou[67], F. Elsner[27,65,104], T. A. Enßlin[85], H. K. Eriksen[68], E. Falgarone[78], J. Fergusson[14], F. Finelli[51,53], O. Forni[105,11], M. Frailis[50], A. A. Fraisse[30], E. Franceschi[51], A. Frejsel[90], S. Galeotta[50], S. Galli[74], K. Ganga[1], T. Ghosh[64], M. Giard[105,11], Y. Giraud-Héraud[1], E. Gjerløw[68], J. González-Nuevo[22,70], K. M. Górski[72,110], S. Gratton[75,67], A. Gregorio[37,50,57], A. Gruppuso[51], J. E. Gudmundsson[102,91,30], F. K. Hansen[68], D. Hanson[87,72,10], D. L. Harrison[67,75], G. Helou[13], S. Henrot-Versillé[77], C. Hernández-Monteagudo[15,85], D. Herranz[70], S. R. Hildebrandt[72,13], E. Hivon[65,104], M. Hobson[6], W. A. Holmes[72], A. Hornstrup[19], W. Hovest[85], K. M. Huffenberger[28], G. Hurier[64], A. H. Jaffe[60], T. R. Jaffe[105,11], W. C. Jones[30], M. Juvela[29], E. Keihänen[29], R. Keskitalo[16], T. S. Kisner[83], R. Kneissl[40,8], J. Knoche[85], M. Kunz[20,64,3], H. Kurki-Suonio[29,46], G. Lagache[5,64], A. Lähteenmäki[2,46], J.-M. Lamarre[78], A. Lasenby[6,75], M. Lattanzi[34,54], C. R. Lawrence[72], J. P. Leahy[73,⋆], R. Leonardi[9], J. Lesgourgues[66,103], F. Levrier[78], M. Liguori[33,71], P. B. Lilje[68], M. Linden-Vørnle[19], M. López-Caniego[41,70], P. M. Lubin[31], J. F. Macías-Pérez[81], G. Maggio[50], D. Maino[36,52], N. Mandolesi[51,34], A. Mangilli[64,77], M. Maris[50], D. J. Marshall[79], P. G. Martin[10], E. Martínez-González[70], S. Masi[35], S. Matarrese[33,71,43], P. McGehee[61], P. R. Meinhold[31], A. Melchiorri[35,55], L. Mendes[41], A. Mennella[36,52], M. Migliaccio[67,75], S. Mitra[59,72], M.-A. Miville-Deschênes[64,10], A. Moneti[65], L. Montier[105,11], G. Morgante[51], D. Mortlock[60], A. Moss[96], D. Munshi[95], J. A. Murphy[88], F. Nati[30], P. Natoli[34,4,54], C. B. Netterfield[23], H. U. Nørgaard-Nielsen[19], F. Noviello[73], D. Novikov[84], I. Novikov[90,84], E. Orlando[109], C. A. Oxborrow[19], F. Paci[93], L. Pagano[35,55], F. Pajot[64], R. Paladini[61], D. Paoletti[51,53], B. Partridge[45], F. Pasian[50], G. Patanchon[1], T. J. Pearson[13,61], M. Peel[73], O. Perdereau[77], L. Perotto[81], F. Perrotta[93], V. Pettorino[44], F. Piacentini[35], M. Piat[1], E. Pierpaoli[26], D. Pietrobon[72], S. Plaszczynski[77], E. Pointecouteau[105,11], G. Polenta[4,49], G. W. Pratt[79], G. Prézeau[13,72], S. Prunet[65,104], J.-L. Puget[64], J. P. Rachen[24,85], W. T. Reach[106], R. Rebolo[69,17,21], M. Reinecke[85], M. Remazeilles[73,64,1], C. Renault[81], A. Renzi[38,56], I. Ristorcelli[105,11], G. Rocha[72,13], C. Rosset[1], M. Rossetti[36,52], G. Roudier[1,78,72], J. A. Rubiño-Martín[69,21], B. Rusholme[61], M. Sandri[51], D. Santos[81], M. Savelainen[29,46], G. Savini[92], D. Scott[25], M. D. Seiffert[72,13], E. P. S. Shellard[14], L. D. Spencer[95], V. Stolyarov[6,100,76], R. Stompor[1], A. W. Strong[86], R. Sudiwala[95], R. Sunyaev[85,98], D. Sutton[67,75], A.-S. Suur-Uski[29,46], J.-F. Sygnet[65], J. A. Tauber[42], L. Terenzi[94,51], L. Toffolatti[22,70,51], M. Tomasi[36,52], M. Tristram[77], M. Tucci[20], J. Tuovinen[12], G. Umana[47], L. Valenziano[51], J. Valiviita[29,46], F. Van Tent[82], M. Vidal[73], P. Vielva[70], F. Villa[51], L. A. Wade[72], B. D. Wandelt[65,104,32], R. Watson[73], I. K. Wehus[72,68], A. Wilkinson[73], D. Yvon[18], A. Zacchei[50], and A. Zonca[31]

(Affiliations can be found after the references)

Received 22 June 2015 / Accepted 20 April 2016

ABSTRACT

We discuss the Galactic foreground emission between 20 and 100 GHz based on observations by *Planck* and WMAP. The total intensity in this part of the spectrum is dominated by free-free and spinning dust emission, whereas the polarized intensity is dominated by synchrotron emission. The `Commander` component-separation tool has been used to separate the various astrophysical processes in total intensity. Comparison with radio recombination line templates verifies the recovery of the free-free emission along the Galactic plane. Comparison of the high-latitude Hα emission with our free-free map shows residuals that correlate with dust optical depth, consistent with a fraction ($\approx$30%) of Hα having been scattered by high-latitude dust. We highlight a number of diffuse spinning dust morphological features at high latitude. There is substantial spatial variation in the spinning dust spectrum, with the emission peak (in I_ν) ranging from below 20 GHz to more than 50 GHz. There is a strong tendency for the spinning dust component near many prominent H II regions to have a higher peak frequency, suggesting that this increase in peak frequency is associated with dust in the photo-dissociation regions around the nebulae. The emissivity of spinning dust in these diffuse regions is of the same order as previous detections in the literature. Over the entire sky, the `Commander` solution finds more anomalous microwave emission (AME) than the WMAP component maps, at the expense of synchrotron and free-free emission. This can be explained by the difficulty in separating multiple broadband components with a limited number of frequency maps. Future surveys, particularly at 5–20 GHz, will greatly improve the separation by constraining the synchrotron spectrum. We combine *Planck* and WMAP data to make the highest signal-to-noise ratio maps yet of the intensity of the all-sky polarized synchrotron emission at frequencies above a few GHz. Most of the high-latitude polarized emission is associated with distinct large-scale loops and spurs, and we re-discuss their structure. We argue that nearly all the emission at $40^\circ > l > -90^\circ$ is part of the Loop I structure, and show that the emission extends much further in to the southern Galactic hemisphere than previously recognised, giving Loop I an ovoid rather than circular outline. However, it does not continue as far as the "*Fermi* bubble/microwave haze", making it less probable that these are part of the same structure. We identify a number of new faint features in the polarized sky, including a dearth of polarized synchrotron emission directly correlated with a narrow, roughly 20° long filament seen in Hα at high Galactic latitude. Finally, we look for evidence of polarized AME, however many AME regions are significantly contaminated by polarized synchrotron emission, and we find a 2σ upper limit of 1.6% in the Perseus region.

Key words. diffuse radiation – ISM: general – radiation mechanisms: general – radio continuum: ISM – polarization – local insterstellar matter

* Corresponding authors: C. Dickinson, `clive.dickinson@manchester.ac.uk`; J. P. Leahy, `j.p.leahy@manchester.ac.uk`

1. Introduction

Diffuse Galactic radio emission consists of a number of distinct components that emit via different emission mechanisms (notably synchrotron, free-free, and spinning dust). There is considerable interest in understanding these components in order to subtract foregrounds cleanly from cosmic microwave background (CMB) data and as a probe of the physics of the interstellar medium (ISM) and Galactic structure. The separation of the diffuse foregrounds into their separate constituent components is extremely difficult, since their spectra (except for free-free emission) are not well-known, and they have comparable intensities at microwave frequencies (Leach et al. 2008).

At low frequencies ($\lesssim$10 GHz), synchrotron radiation from electrons spiralling in the Galactic magnetic field dominates the sky. At frequencies around 1 GHz the spectral index ($T \propto \nu^{\beta}$) is $\beta \approx -2.7$, while at higher frequencies it appears to steepen to $\beta \approx -3.0$. This broadly agrees with theoretical calculations, such as those from the GALPROP[1] code (Orlando & Strong 2013); however, a detailed comparison has not been made up to now, due to difficulties in the component separation process. Synchrotron radiation is intrinsically highly polarized and is a strong polarized CMB foreground up to around 100 GHz. Free-free emission emits over a range of radio frequencies and can be significant up to about 100 GHz owing to its flatter spectral index ($\beta = -2.1$). Anomalous microwave emission (AME) is an additional foreground that has been detected at frequencies 10–60 GHz (Leitch et al. 1997; de Oliveira-Costa et al. 2004; Finkbeiner 2004; Davies et al. 2006; Planck Collaboration XX 2011; Planck Collaboration XXI 2011; Planck Collaboration Int. XV 2014) above the expected levels of synchrotron and free-free emission. The most plausible origin for AME is electric dipole radiation from tiny, rapidly spinning dust grains (Draine & Lazarian 1998), which provides an excellent fit to the data, particularly from well-studied molecular clouds (Planck Collaboration XX 2011). However, the diffuse emission at high latitudes has still to be definitively identified, and other possibilities exist, such as magneto-dipole radiation from thermal fluctuations of magnetized grains (Draine & Lazarian 1999; Liu et al. 2014). The polarization of AME is of great interest to CMB cosmologists, since a significant level of polarization could hamper measurements of B modes. Current measurements place upper limits on the polarization of AME at a few per cent or below (Dickinson et al. 2011; Macellari et al. 2011; Rubiño-Martín et al. 2012a).

In the 2013 *Planck*[2] results based on spectral fitting, the component separation procedure did not achieve a separation of the distinct low-frequency components, instead lumping these into a single low-frequency foreground (Planck Collaboration XII 2014). However, other methods have been used to do this under specific assumptions; Planck Collaboration Int. XII (2013) used correlated component analysis in the southern Gould Belt region where synchrotron emission is relatively smooth and weak, while Planck Collaboration Int. XXII (2015) used template fitting to separate components that were correlated with each spatial template. In the 2015 analysis (Planck Collaboration X 2016) we include the WMAP (Bennett et al. 2013a) and 408 MHz (Haslam et al. 1982) all-sky maps to enable a separation of synchrotron, free-free, and AME. The separation is based on fitting a spectral model to each sky pixel using Commander, a Gibbs sampling code (Eriksen et al. 2008).

The current *Planck* data release also includes polarization information. At angular scales larger than 1° the polarized emission is dominated by synchrotron and thermal dust radiation. Synchrotron radiation is more important at low frequencies and dominates the polarized *Planck* maps at 30 and 44 GHz. This synchrotron emission comes mainly from the Galactic plane and also from filamentary structures that can extend over 100° across the sky. While these "loops" and "spurs" have long been known in total intensity (Quigley & Haslam 1965; Berkhuijsen et al. 1971; Berkhuijsen 1971), their pattern is clarified by the new polarization maps. Vidal et al. (2015) present an analysis of the filaments using WMAP data. They have catalogued them, studied the polarization angle distribution and polarized spectral indices, and presented a model to explain the origin of some of them. Here, with the new *Planck* polarization data, we expand on this, identifying new polarized features and understanding better the already known ones, thanks to the improved signal-to-noise ratio (S/N) of the data.

We begin in Sect. 2 by summarizing the data sets employed, including a brief discussion of some of the most important systematic effects. We then take a first look at the intensity foregrounds in Sect. 3 by employing a constrained internal linear combination (ILC) algorithm to remove the CMB and free-free emission components whose spectra are well known. In Sect. 4 we then discuss each of the low frequency foreground components (AME, free-free, and synchrotron emission) as determined by the Commander algorithm. We use these new maps to investigate the distribution and spectra of these foregrounds. In Sect. 5 we use WMAP/*Planck* polarization maps to study the distribution of the low frequency polarized foregrounds. We make a high S/N synchrotron map by combining the WMAP/*Planck* data into a single product, assuming a power-law model for synchrotron emission. We discuss in detail the large-scale features in the low frequency polarized sky including the well-known loops and spurs. Other results will be published in separate articles, including the diffuse synchrotron power spectrum and further analysis of AME polarization constraints from Galactic clouds. We conclude in Sect. 6.

2. Data

Table 1 lists the primary radio data sets used in our analysis, with properties that are important here. We note that brightness temperatures are in the Rayleigh-Jeans convention unless otherwise stated (WMAP and *Planck* data are natively in CMB thermodynamic temperature). We now briefly discuss these data sets and particular issues that are relevant to our analysis.

2.1. WMAP and Planck data

The primary data used in the analysis are the 9-year WMAP maps (Bennett et al. 2013a) and the 2015 release of *Planck* maps (Planck Collaboration I 2016; Planck Collaboration II 2016; Planck Collaboration VIII 2016) from the Low Frequency Instrument (LFI) and High Frequency Instrument (HFI). Details of the map preparation, including smoothing to 1° full-width half-maximum (FWHM) resolution and correction of residual offsets and gain errors, are given in

[1] http://galprop.stanford.edu; http://sourceforge.net/projects/galprop/

[2] *Planck* (http://www.esa.int/Planck) is a project of the European Space Agency (ESA) with instruments provided by two scientific consortia funded by ESA member states and led by Principal Investigators from France and Italy, telescope reflectors provided through a collaboration between ESA and a scientific consortium led and funded by Denmark, and additional contributions from NASA (USA).

Table 1. Summary of radio data sets used, with selected properties.

Map	Instrument	ν_0 [GHz] [a]	$\eta_{\Delta T}(\nu_0)$ [b]	σ_I [c] [μK]	w_0 [d]	w_1 [d]	w_2 [d]	w_3 [d]
Haslam	Effelsberg/Jodrell/Parkes	0.408	1.000	3×10^6	...	...	...	...
K band	WMAP	22.8	0.987	6.00	...	1.007	...	1.549
30 GHz	*Planck* LFI	28.4	0.979	2.49	1.013	...	3.585	−0.485
*K*a band	WMAP	33.0	0.972	4.44	...	...	...	−0.788
Q band	WMAP	40.6	0.958	3.86	...	...	...	−1.342
44 GHz	*Planck* LFI	44.1	0.951	2.80	...	...	−9.571	−2.457
V band	WMAP	60.8	0.910	4.32	...	...	...	...
70 GHz	*Planck* LFI	70.4	0.881	2.22	...	...	...	...
W band	WMAP	93.5	0.802	5.14	...	...	...	...
100 GHz	*Planck* HFI	100	0.777	0.86	...	...	...	...
143 GHz	*Planck* HFI	143	0.592	0.37	−1.052	−1.088	6.194	3.648
217 GHz	*Planck* HFI	217	0.334	0.51	...	...	...	...
353 GHz	*Planck* HFI	353	0.075	1.69	0.039	0.038	−0.208	−0.126
545 GHz	*Planck* HFI	545	0.006	0.51[e]	...	...	...	...
857 GHz	*Planck* HFI	857	6×10^{-5}	0.48[e]	...	...	...	...

Notes. [(a)] Reference frequency. [(b)] Conversion factor from differential thermodynamic temperature to Rayleigh-Jeans brightness temperature. [(c)] Median rms per beam for the 1° smoothed Stokes *I* maps. [(d)] Weights for the linear combination images shown in Figs. 1a and 2a (w_0), Fig. 2b (w_1), Fig. 3a (w_2), and Fig. 3b (w_3). [(e)] Units MJy sr^{-1}.

Planck Collaboration X (2016). The products are at `HEALPix` $N_{\rm side} = 256$. In addition, for polarization analysis we have prepared maps at 2° resolution, using the same methodology as for the 1° maps. Component separation depends critically on the accuracy of the input data, and so we briefly review data quality issues here.

Thermal noise. This is accurately characterized in the *Planck* and WMAP data. For both missions, the noise is quite variable over the sky. We have calculated the thermal noise in our smoothed maps via propagation of errors, assuming the noise is independent between pixels at our full resolution. After smoothing, the noise in nearby pixels is strongly correlated.

Confusion. Confusion noise denotes the uncertainties caused by faint compact sources within each beam. It has been estimated from source counts made at much higher angular resolution. To some extent, confusion is automatically fitted out as part of component separation. This would be exactly true if the source had a spectrum that could be well fitted by our model, and was non-variable. In fact, typical sources responsible for confusion in our maps are blazars, characterized by strong variability and "flat" ($\beta \approx -2$) spectra, which are similar to free-free emission, but may contain multiple peaks (e.g., Planck Collaboration XIII 2011). Hence a fraction of the confusion is an effective noise component in our fitting.

Calibration. Uncertainties for both WMAP and *Planck* due to calibration are about 0.2% for most frequencies and this contributes negligibly to our error budget. The two highest-frequency HFI channels have raw uncertainties of $\lesssim$10% (Planck Collaboration VIII 2016), and corrections were derived as part of the component separation fit; these uncertainties have very little impact on the low-frequency components discussed in this paper. The global calibration uncertainty of the Haslam et al. (1982) map is about 10%, but this only impacts our estimate for the break in the synchrotron spectrum. There is also an additional source of error that arises from the broad bandwidths of the *Planck* and WMAP detectors. We can take these into account by applying "colour corrections" that depend on the spectral response of the instrument and the spectrum of the sky signal (Jarosik et al. 2011; Planck Collaboration II 2014; Planck Collaboration IX 2014; Planck Collaboration II 2016; Planck Collaboration VII 2016). For *Planck* LFI these corrections are typically 1–3% while they are 5–10% for HFI. The residual errors from such corrections are likely to be $\lesssim$1%, especially for the LFI channels of interest here. We implement WMAP colour corrections using the same approach as for the LFI, allowing for the secular drift of the centre frequency (Bennett et al. 2013a) and the small bandpass shifts derived in Planck Collaboration X (2016). Uncertainties due to residual beam asymmetry in the smoothed WMAP/*Planck* data will be, relative to other uncertainties, minimal because we have used the deconvolved WMAP data and the additional smoothing to 1° FWHM resolution will symmeterize the beam.

Offsets. Neither *Planck* nor WMAP measured the absolute zero level in total intensity, and so there is an arbitrary offset in each map. There is also a small but obvious residual dipole in differences between *Planck* and WMAP maps. In the analysis in Sect. 3 we use the approach of Wehus et al. (2016) that uses *T*–*T* plots to estimate the dipole and monopole amplitudes for each map (exact values were updated based on the 2015 release *Planck* maps); the approach used for the `Commander` analysis is described in Planck Collaboration X (2016). The zero levels in the polarization maps (Stokes *Q* and *U*) are much better defined, and are recovered with negligible error by *Planck*. In contrast, two large angular scale modes in the WMAP *Q* and *U* maps are sensitive to zero-level uncertainties in the raw data. These "poorly constrained modes" were down-weighted by the WMAP team in their power spectrum analysis (Bennett et al. 2013a), but this approach is not available when attempting to model the spectrum pixel-by-pixel. They are strong enough to seriously affect the absolute polarized brightness over most of the sky, except for the regions of strongest polarized intensity, such as the Galactic plane and the North Polar Spur.

Polarization leakage. Various processes cause leakage of total intensity into the polarization signal, notably mismatch between the beamshapes for the two polarizations in each horn, and bandpass mismatch (e.g., Leahy et al. 2010). The WMAP scanning strategy allows a rather accurate correction for these effects, but a more indirect approach is needed for *Planck* (Planck Collaboration II 2016) and the corrections applied are believed to be accurate to a few tenths of a percent of the total intensity. This is a significant problem along the Galactic plane, where the fractional polarization is very low and so the residual bandpass leakage error is relatively high. Beam mismatch leakage is also strong on the plane, due to the steep intensity gradients there. But for most of the sky, the residual leakage is essentially negligible.

Unmodelled emission. This includes the Sunyaev-Zeldovich (SZ) effect over most of the sky[3], most spectral lines, and the spectrum of extragalactic point sources. Hundreds of transitions are known in the part of the spectrum of interest here, but over most of the sky they are expected to be very weak compared to the continuum in our broad bands. However, they are not always negligible: rich line spectra are generated in photo-dissociation regions (PDRs) surrounding H II regions, and also in the X-ray dominated region around the Galactic centre (Takekawa et al. 2014). While this spectral contamination is certainly unusual, there are no blind spectral line surveys in most of our bands that would allow us to set reliable upper limits to line contamination. The `Commander` fit actually includes line emission (CO and HCN) in four of our bands.

2.2. Ancillary data

Below 20 GHz, several radio maps are available. Reich et al. (2004) have presented a preliminary map at 1.4 GHz, but the combination of instrumental artefacts and calibration uncertainties in the survey do not meet our stringent requirements on the error budget, which also caused us to drop a number of *Planck* data sets as described in Planck Collaboration X (2016). We do use the 408-MHz map of Haslam et al. (1982), as re-processed by Remazeilles et al. (2015) to reduce instrumental striping and provide better point-source subtraction than previous versions. The noise in the Haslam et al. (1982) map is not characterized in detail, but in any case is much less than residual scanning artefacts. We assume an rms error of 1 K, including both effects. We also assume a 10% uncertainty in the overall intensity scale.

The Galactic synchrotron spectrum shows significant curvature below 10 GHz, while free-free absorption sets in for bright H II regions below a few hundred MHz. We therefore do not consider maps at frequencies below 408 MHz.

We use the full-sky dust-corrected Hα map of Dickinson et al. (2003) to compare with our free-free solution at high latitudes where dust absorption is relatively small. The fraction of dust lying between us and the Hα-emitting gas is assumed to be 1/3 ($f_{\rm d}$ = 0.33). We also use the Finkbeiner (2003) Hα map to test the results. At low latitudes, we make use of the radio recombination line (RRL) survey recovered from the HIPASS data at 1.4 GHz (Alves et al. 2015). This survey detects RRLs from ionized gas along the narrow Galactic plane with a resolution of 15′. Although of limited sensitivity, it provides the radio equivalent of Hα maps without absorption along the line of sight.

[3] The largest SZ signals, due to the Coma and Virgo clusters, are explicitly fitted by `Commander`, but this is only feasible because other foreground components are very faint in these regions.

We use the IRIS reprocessed far infrared (FIR) map from the IRAS survey at 100, 60, 25, and 12 μm (Miville-Deschênes & Lagache 2005). The intensity scale is good to 13% and instrumental noise is effectively insignificant after smoothing to 1° resolution. We also use the H I map from the LAB survey (Kalberla et al. 2005).

We also make use of the ROSAT diffuse sky survey maps. The original images provided by the Max-Planck-Institut für Extraterrestrische Physik (MPE)[4] are stored as six panels that between them cover the whole sky, with slight overlaps between adjacent panels. The pixel size is 12′. The 0.1–2 keV energy range is divided into six bands. The publicly available FITS images are derived from the analysis by Snowden et al. (1997) of the 1990–1991 ROSAT survey observations, and do not include the make-up data collected in 1997 and presented by Freyberg & Egger (1999); consequently they show narrow strips of missing data. After correcting erroneous field centres in the MPE FITS headers, we found the pixel coordinates in the original images of `HEALPix` (Górski et al. 2005) pixels at $N_{\rm side}$ = 2048, so that the original pixels are highly oversampled. Nearest-neighbour interpolation was used for placing the intensity and uncertainty values into the `HEALPix` grid. We averaged the data and uncertainties onto an $N_{\rm side}$ = 256 pixel grid (pixel size 13.′7, comparable to the original), weighting each raw pixel by the area contributed to the output `HEALPix` pixel. We then merged the `HEALPix` maps of the six original panels into a single all-sky map, using simple averaging for pixels covered by two or more panels[5].

3. A first look at the low-frequency foregrounds using constrained internal linear combinations

Of all the emission mechanisms contributing to the cm-wavelength sky, the CMB is the most accurately measured, since the data are calibrated directly on the CMB dipole, and it is also the only component with a precisely known spectrum. It can therefore be straightforwardly eliminated by constructing linear combinations of the individual frequency maps. Therefore, as a first look, we apply a linear combination to the WMAP/*Planck* maps to investigate the range of spectral indices and morphologies at frequencies around 20–50 GHz. Our approach (Appendix A) is similar to, but simpler and more limited than, standard ILC techniques.

Figure 1a shows the total foreground emission in the *Planck* 30 GHz band (reference frequency of 28.4 GHz), constructed via

$$T_{\rm foreground} = w_{30}T_{30} + w_{143}T_{143} + w_{353}T_{353} \quad (1)$$

where the subscripts refer to channel frequencies, the weights w_i are given in Table 1 and, as always in this section, are normalized to return a $\beta = -3$ power law unchanged. We use the *Planck* HFI 143 GHz band as our primary model of the CMB, since it has the lowest noise and is dominated by only two components, the CMB itself and thermal dust emission. The latter is cleaned to adequate precision for display purposes using the HFI 353 GHz map. The dust is modelled as a uniform modified blackbody spectrum with $\beta_{\rm d}$ = 1.51 and $T_{\rm d}$ = 19.6 K

[4] `http://www.xray.mpe.mpg.de/rosat/survey/sxrb/12/ass.html`. Although these web pages display GIF images including the 1997 make-up observations, the downloadable FITS images include only the 1990–91 data.

[5] All-sky `HEALPix` maps of the six ROSAT bands created as described here are available at `http://www.jb.man.ac.uk/research/cosmos/rosat/`

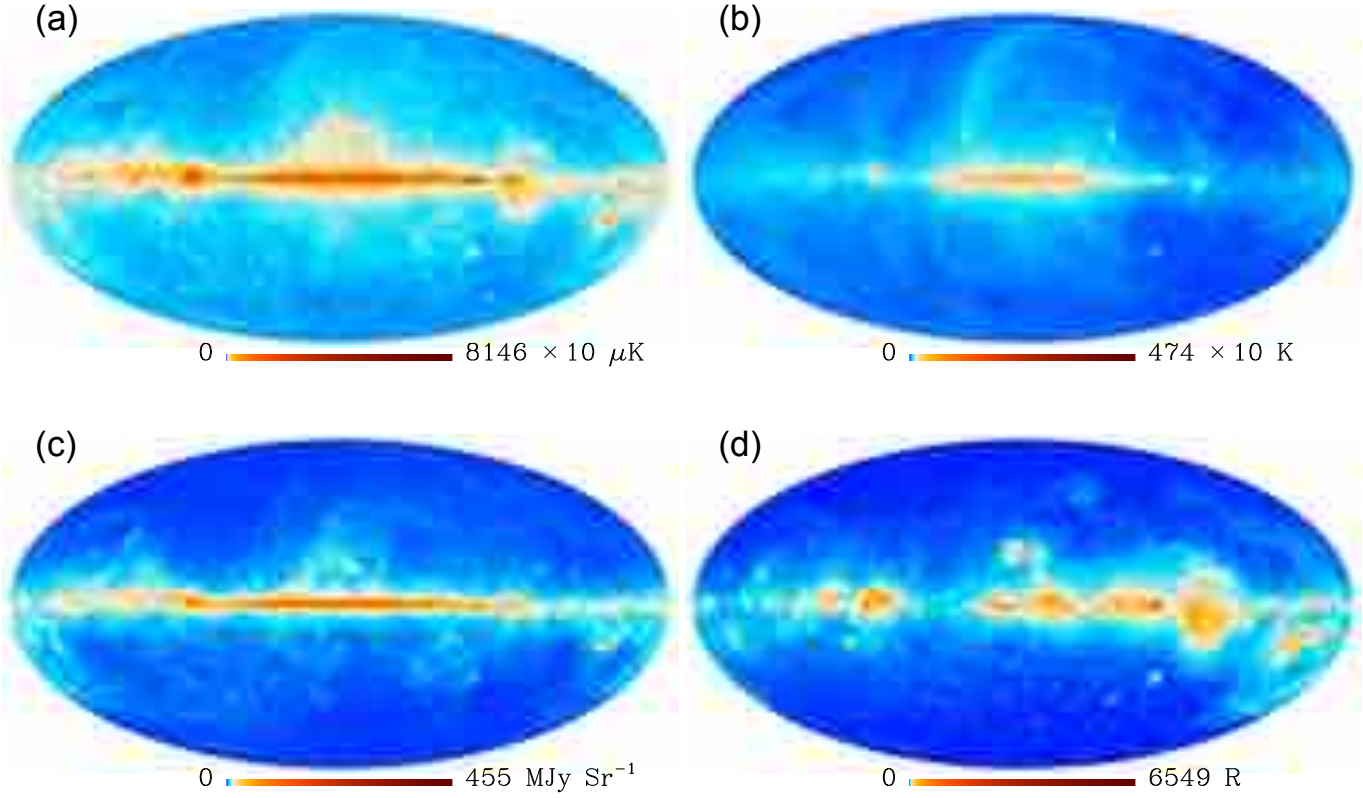

Fig. 1. a) CMB-nulled map at 28.4 GHz, constructed using the ILC method (see text), where in this map, $\beta = -3$ emission is unchanged by construction; **b)** 408 MHz map (Remazeilles et al. 2015), strongly dominated by synchrotron emission; **c)** 545 GHz *Planck* map, strongly dominated by thermal dust emission; and **d)** Hα map (Dickinson et al. 2003). An asinh(I) colour scale is used for all images, where I is the intensity in the units indicated. The coordinate along the colour bar is linear in I near zero and becomes logarithmic (ln(2I)) at high intensity. All maps are at 1° resolution.

(Planck Collaboration Int. XXII 2015). This combination fractionally diminishes the amplitude of free-free emission, but only by 0.7%, which is negligible for display purposes.

Figure 1 also shows our ancillary maps at 408 MHz (tracing synchrotron emission), Hα (tracing free-free emission), and the *Planck* 545 GHz map (tracing thermal dust emission). Features of all these templates appear in the 28.4 GHz foreground map: the brightest features along the Galactic plane are mostly free-free emission; at high latitudes in the northern hemisphere the North Polar synchrotron spur is prominent; while obvious dust-related features include the ρ Oph complex, the Chameleon/Musca complex of cold clouds arcing around the South Celestial Pole, the Polaris Flare, and the comet-shaped R CrA molecular cloud. In addition to the diffuse components, there are thousands of point sources. In fact, at this resolution the map is strongly confusion-limited (Fig. 2); the median thermal noise is 2.5 μK, but the rms in patches a few degrees across is about 10 μK, even in regions far from the plane where catalogued sources have been avoided. Consequently a signal is detected significantly in almost every pixel, and only a few SZ decrements (notably from the Coma Cluster) give a negative map intensity.

After the CMB, the next best determined spectrum is free-free emission. Assuming local thermodynamic equilibrium, the spectral shape depends, very weakly, on a single parameter, the electron temperature T_e; we use the approximation of Draine (2011) detailed in Sect. 4.1 below. For plausible values, $3000 < T_e < 15\,000$ K, the ratio of observed brightness between our 30 and 44 GHz bands varies only between 2.52 and 2.49 (including the effect of colour corrections). We can therefore null this component, taking $T_e = 7500$ K, by differencing CMB-corrected maps at 28.4 and 44.1 GHz. Figure 3a shows the result.

The drawback of this procedure is that the thermal noise is amplified by a factor of 11, partly because the differencing introduces noise from the 44 GHz image, and partly due to the renormalization. The situation can be considerably improved by including WMAP data: Fig. 3b shows a similar analysis that includes the three lowest-frequency WMAP bands, where we maximize the S/N of our reference $\beta = -3$ spectrum as well as eliminating CMB, free-free, and thermal dust. In this case the S/N is 5.5 times worse than in the original 28.4 GHz map; the better performance is partly due to the larger frequency ratio (22.8/44.1 vs. 28.4/44.1), which reduces the unwanted cancellation of the synchrotron emission.

Emission with a power-law spectrum steeper than free-free, i.e., $\beta < -2.1$, will show up as positive in the free-free nulled maps, and these show (albeit with higher noise) the characteristic synchrotron and AME features noted in our description of Fig. 1 above. Most of the extragalactic sources are nearly nulled, since their spectrum is similar to free-free; those remaining are mostly optically-thin synchrotron sources, but sources that varied between the WMAP and *Planck* mean epochs also show up (as negative residuals if they were brighter during the *Planck* observations).

In this double difference image the assumed thermal dust spectrum begins to have a significant impact; if we use $\beta_d = 1.66$ and $T_d = 19.0$ K (Planck Collaboration Int. XIV 2014) the inner Galactic plane becomes about 20% brighter. Given that T_d is known to vary significantly between the inner and outer Galaxy

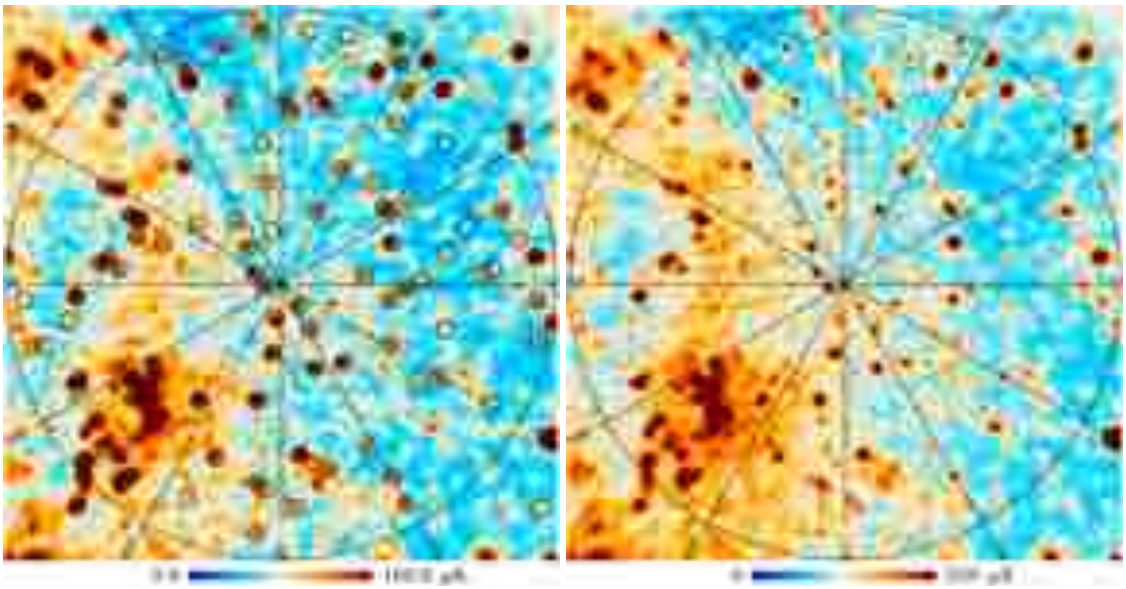

Fig. 2. *Left*: **a)** south polar region of the CMB-nulled 28.4 GHz map. Overplotted circles are the positions of 30-GHz sources from the second *Planck* Catalogue of Compact Sources (PCCS2, Planck Collaboration XXVI 2016). The 90% completeness limit for the catalogue (426 mJy) corresponds to a peak brightness of $\Delta T \approx 50\,\mu$K at the 1° resolution of this map. *Right*: **b)** same region in a CMB-nulled version of the WMAP *K*-band map (22.8 GHz). The diffuse arc in the range $30° < l < 150°$ is part of Loop II. The colour scales are linear here.

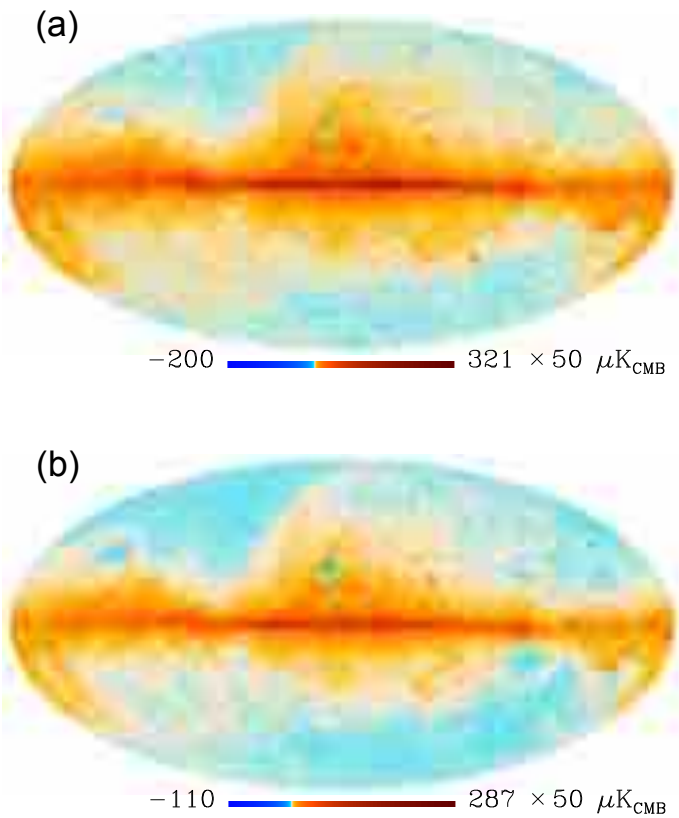

Fig. 3. Maps with CMB, free-free, and thermal dust emission nulled, scaled so that a $\beta = -3$ power-law spectrum is unchanged in amplitude. **a)** *Planck*-only map (28.4, 44.1, 143, 353 GHz), scaled to 28.4 GHz. **b)** Combined *Planck* and WMAP. Weights used are given in Table 1. An asinh colour scale is used and an offset of 80 μK$_{\rm CMB}$ has been subtracted to enhance the contrast.

(e.g., Planck Collaboration XI 2014), more sophisticated modelling is required to obtain the most from the data.

Nevertheless, the ILC approach does reveal an important complexity of the low-frequency foreground spectrum in a straightforward way, namely as prominent extended regions of negative intensity, notably coincident with the Sh2-27 H II region at $(l, b) = (6°, 24°)$, and in the southern part of the Gum nebula, around $(l, b) = (257°, -14°)$. These are regions with excess flux compared to the free-free spectrum near 40 GHz. They can be fitted with a spinning dust spectrum shifted to peak at higher frequencies than standard models, but still within the range of plausible interstellar parameters (e.g., Planck Collaboration XX 2011; Planck Collaboration Int. XV 2014).The Sh2-27 spinning dust is likely to be associated with the famous translucent cloud in which interstellar molecules were first discovered, as absorption lines in the spectrum of the ionizing star ζ Oph (Adams 1941). In fact, many bright H II regions show negative residuals, e.g., the California nebula $(l, b) = (161°, -13°)$, Orion A and B $(l, b) = (210°, -19°)$ and $(207°, -17°)$, and many of the bright nebulae along the Galactic plane.

These residuals are not due to errors in our assumed $T_{\rm e}$ values; pushing $T_{\rm e}$ as high as 15 000 K makes almost no difference to the spectrum and so leaves all these features in place. They are also insensitive to changes in estimated colour corrections between Planck Collaboration II (2014) and Planck Collaboration II (2016). They become less prominent for steeper assumed thermal dust spectra ($\beta_{\rm d}$), but this is mainly due to the impact of $\beta_{\rm d}$ on the underlying Galactic ridge emission noted above.

The systematic negative residuals suggest that high-frequency spinning dust may often be associated with the PDRs around H II regions. Dobler & Finkbeiner (2008b) also identified a potential high-frequency spinning dust component in WMAP data that was correlated with Hα from the Warm Ionized Medium. An alternative explanation in at least some cases (in particular the Galactic centre) might be significant line emission in the 39–46 GHz region common to WMAP Q and the LFI 44-GHz bands; however well-known lines in this band, such as SiO (1–0) and methanol masers, do not seem to be bright enough to cause the effect (Jordan et al. 2015; Jordan, priv. comm.). The

implications of the wide range in AME peak frequency are discussed in Sect. 4.2.

From this preliminary analysis we can draw two further lessons. First, separating components with similar spectra makes great demands on sensitivity; even separating free-free emission ($\beta = -2.1$) from synchrotron ($\beta \approx -3$) has dramatically reduced our effective S/N. The synchrotron spectral index varies by only a few tenths across the sky, and to map it with useful precision we need a substantial gain in sensitivity. This has been achieved mainly by working at low resolution (Fuskeland et al. 2014; Vidal et al. 2015); in the current paper we use a fixed template for the synchrotron spectrum (Sect. 4.3 below).

Second, low-frequency foregrounds have complicated spectra: at a minimum, we must solve for the amplitudes of free-free emission, synchrotron emission, and AME, and for the latter the peak frequency and spectral width. However, even including the WMAP data, we have only five frequency maps between 22 and 44 GHz to solve for these five parameters. With no spare degrees of freedom, we would be susceptible to both errors in the assumed spectral model and any artefacts in the data. We therefore need to use maps at higher and lower frequencies.

Above 44 GHz we have the *Planck* maps at 70 and 100 GHz and WMAP V- and W-bands (60 and 94 GHz). There is significant line contamination in the W- and 100 GHz-bands, which has to be included in the component separation. In all these maps the strongest foreground component is the low-frequency tail of the thermal dust emission, for which it is necessary to fit at least the temperature $T_{\rm d}$ and probably the emissivity index $\beta_{\rm d}$ as well. As a result, including these higher frequency maps gives us more data points but also require us to solve for more spectral parameters. Moreover, since the foreground emission is weakest at these frequencies, the maps have relatively poor S/N. The `Commander` approach discussed in the next section is our best attempt to date to handle these complexities.

4. Total intensity foregrounds with Commander

The analysis of Sect. 3 demonstrated the complexity of the low-frequency foreground spectrum, but for that very reason was unable to separate the various diffuse foreground components that contribute to the maps. A more sophisticated method is required, and numerous algorithms exist that utilize the spectral and/or morphological information in the data. One of the most powerful algorithms is parametric fitting via Gibbs sampling, which has been implemented in the `Commander` code (Eriksen et al. 2008). The details of the specific implementation to these data are described in Planck Collaboration X (2016). In this section, we discuss the models for the low-frequency components used by `Commander`, and compare the derived foreground products with previous results such as WMAP component-separation products. We also compare the results with expectations, either based on theory or extrapolations from ancillary data.

4.1. Free-free

The free-free radio continuum brightness can be estimated by the use of recombination lines. The most widely used is the Hα line (λ656.28 nm), which traces warm ionized gas and is proportional to the emission measure (EM), in the same way as free-free radio continuum (Dickinson et al. 2003). Thus Hα is a reliable estimator provided that the gas is in local thermodynamic equilibrium (LTE), that there is no significant dust absorption along the line-of-sight, that there is no significant scattered component of Hα light, and that the electron temperature is known. The relationship between the free-free brightness $T_{\rm b}^{\rm ff}$ [μK] and Hα intensity $I_{\rm H\alpha}$ [R] for the optically thin limit is given by

$$\frac{T_{\rm b}^{\rm ff}}{I_{\rm H\alpha}} = 1512\, T_4^{0.517}\, 10^{0.029/T_4}\, \nu_{\rm GHz}^{-2.0}\, g_{\rm ff}\,, \tag{2}$$

where T_4 is the electron temperature in units of 10^4 K, $\nu_{\rm GHz}$ the frequency in GHz, and $g_{\rm ff}$ is the Gaunt factor, which takes into account quantum mechanical effects. In the pre-factor we have included a factor of 1.08 to account for the He II contribution that adds to the free-free continuum[6]. Draine (2011) provides an approximation to $g_{\rm ff}$ that is accurate to within about 1% in the *Planck* frequency range:

$$g_{\rm ff}(\nu, T_{\rm e}) = \ln\left\{\exp\left[5.960 - \frac{\sqrt{3}}{\pi}\ln\left(\nu_{\rm GHz} T_4^{-3/2}\right)\right] + e\right\}\,. \tag{3}$$

At high Galactic latitudes, the absorption by dust is a small effect ($\lesssim$0.1 mag), and can be corrected for to first-order. The electron temperature is known to vary throughout the Galaxy, but has typical values of (7500 ± 1000) K in the local diffuse ISM (Shaver et al. 1983; Paladini et al. 2004; Alves et al. 2012). This corresponds to a theoretical radio-to-Hα ratio of (11.1 ± 0.9) μK R^{-1} at 22.8 GHz, assuming $T_{\rm e}$ = (7500 ± 1000) K. However, previous template fitting results have indicated that the measured ratio is lower than this value, at ≈7–10 μK R^{-1} (Davies et al. 2006; Ghosh et al. 2012).

This apparent discrepancy can be resolved with a lower electron temperature ($T_{\rm e} \approx 4000$ K), although this is outside the range expected for our position in the Galaxy. Dust absorption cannot explain it since it has the opposite effect: it would increase the derived Hα emissivity resulting in an even lower ratio. The most popular explanation is that a fraction of the observed Hα intensity is from light scattered by dust grains (assuming the gas is close to being in LTE). Previous estimates of this fraction suggested relatively low values (around 10%), while more recent analyses indicate that as much as half of the high latitude Hα intensity could be scattered (Witt et al. 2010). Other analyses give values around the 10–20% level (Wood & Reynolds 1999; Brandt & Draine 2012; Barnes et al. 2015). We attempt to estimate the scattered fraction in Sect. 4.1.1. We begin by comparing our derived free-free amplitude with the observed Hα. We note that there are essentially no constraints on $T_{\rm e}$ from the `Commander` solution, which is based on variations in the free-free spectral index, except in the inner Galactic plane (see Sect. 4.1.2).

Figure 4 (top panel) shows a T–T plot of the free-free amplitude against the Hα intensity for the Gum nebula region (which is known to be dominated by free-free emission), as defined in Fig. 5. A very good correlation can be seen, which indicates the robustness of the `Commander` free-free amplitude. The best-fitting slope is (8.9 ± 0.9) μK R^{-1}. This corresponds to an electron temperature of (5200 ± 900) K, which is consistent for the temperature measured around the same region using Hydrogen RRL by Woermann et al. (2000). We also measure the free-free-Hα correlation using a full-sky map, masking the more dusty regions (Fig. 4, bottom panel). The mask was defined by ignoring all pixels with an optical depth at 353 GHz, τ_{353}, larger than 1.5×10^{-5} (this corresponds to an extinction at

[6] We note that in Planck Collaboration X (2016), the equation for the free-free continuum brightness does not take into account this additional contribution from helium.

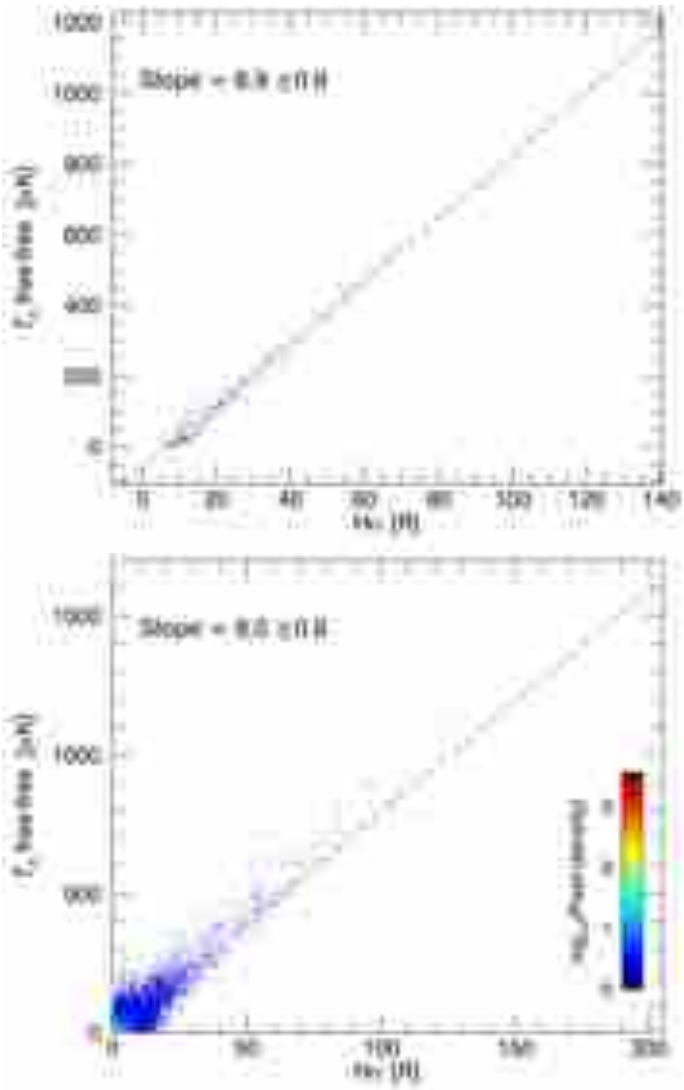

Fig. 4. *Top*: T–T plot of the free-free amplitude at 22.8 GHz against the Hα intensity [R] in the Gum Nebula (see Fig. 5 for the location of the region). *Bottom*: T–T plot for 85% of the sky. Regions that show large dust absorption have been masked out, mostly within $|b| \lesssim 7°$.

the Hα wavelength of $A(\mathrm{H}\alpha) = 0.54$ mag, assuming a reddening value $R_V = 3.1$; Planck Collaboration XI 2014), which results in a masked area of approximately 15% of the sky, mostly on the Galactic plane. In the region studied, we find a best-fitting slope between the Commander free-free map and the Hα map of $(8.0 \pm 0.8)\,\mu\mathrm{K}\,R^{-1}$. This is close to the value for the Gum nebula, and is consistent with previous analyses of the free-free-to-Hα ratio at this frequency (Banday et al. 2003; Davies et al. 2006; Ghosh et al. 2012). This gives us additional confidence that the component separation has worked relatively well for the free-free component. Assuming the theory is correct, this lower value for the free-free to Hα ratio suggests a lower value for T_e, of around 4500 K. However, it is likely that a fraction of the Hα intensity is from scattering of Hα light from the Galactic ridge by dust grains.

4.1.1. High latitude Hα scattering

In this section we estimate the fraction, f_scatt, of Hα light that is scattered by dust grains. This is believed to be responsible for

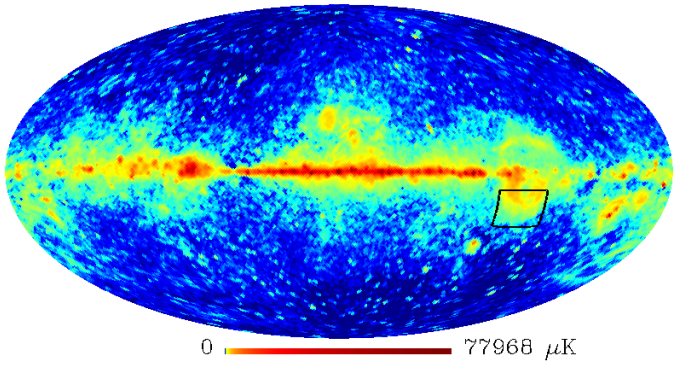

Fig. 5. Commander free-free full-sky map at 22.8 GHz. The box shows the region we selected in the Gum nebula for the scatter plot shown in Fig. 4.

the low free-free to Hα ratio discussed in the previous section, and could reduce the intrinsic Hα intensity by up to ≈50% (Witt et al. 2010). To do this, we must constrain T_e, since there is a one-to-one degeneracy between T_e and f_scatt. For high latitude sight-lines away from the Galactic plane, we can assume that the bulk of the gas is at the local value $T_\mathrm{e} = (7500 \pm 1000)$ K, thus breaking the degeneracy. We initially ignore variations in dust absorption, since we have masked out the regions that are most affected. We test the effect of this assumption by making a nominal correction for dust absorption.

First, we use the theoretical proportionality constant that relates the Hα intensity with the Commander free-free emission, $(11.1 \pm 0.9)\,\mu\mathrm{K}\,R^{-1}$, to scale the free-free template to Rayleigh units. We note that the uncertainty accounts for a ±1000 K uncertainty in T_e. We subtract this template from the Hα map to obtain the Hα emission that does not come from in-situ recombination, i.e., originating from Hα light scattered by dust grains. The top panel in Fig. 6 shows the residual map, with the pixels masked out shown in grey and the colour scale being truncated to $\pm 2\,R$, which saturates the brightest regions closer to the Galactic plane and the Gould Belt. A feature of this residual map is the blue central region, which resembles the microwave haze noted by Finkbeiner (2004), Dobler & Finkbeiner (2008a) and Planck Collaboration Int. IX (2013). This is not unexpected, since the haze was discovered by assuming that Hα is an accurate free-free template. This is an indication that component separation is ambiguous in this complex region, since mixed emission from the Gould Belt system makes the separation between AME, free-free, and synchrotron particularly difficult. There may also be component separation issues in other regions of the sky at a lower level, which could have a significant impact on these residuals.

However, we can still set an upper limit for the amount of scattered Hα light, based on the value of the free-free to Hα ratio measured over the sky. The mean value at 22.8 GHz that we measure over most of the sky is $(8.0 \pm 0.8)\,\mu\mathrm{K}\,R^{-1}$. From this, if we assume that the difference relative to the theoretical value of $(11.1 \pm 0.9)\,\mu\mathrm{K}\,R^{-1}$ is due to an excess of Hα emission from scattering, we can estimate the scattering fraction to be $f_\mathrm{scatt} = (28 \pm 12)\%$. This is an average value for the high latitude sky, so individual regions with different electron temperature might be present a level higher than this. It is consistent with previous estimates of around 20% of scattered light on average at high latitudes (Wood & Reynolds 1999; Witt et al. 2010; Dong & Draine 2011; Brandt & Draine 2012; Barnes et al. 2015). If we repeat the calculation using a dust-corrected Hα map, assuming

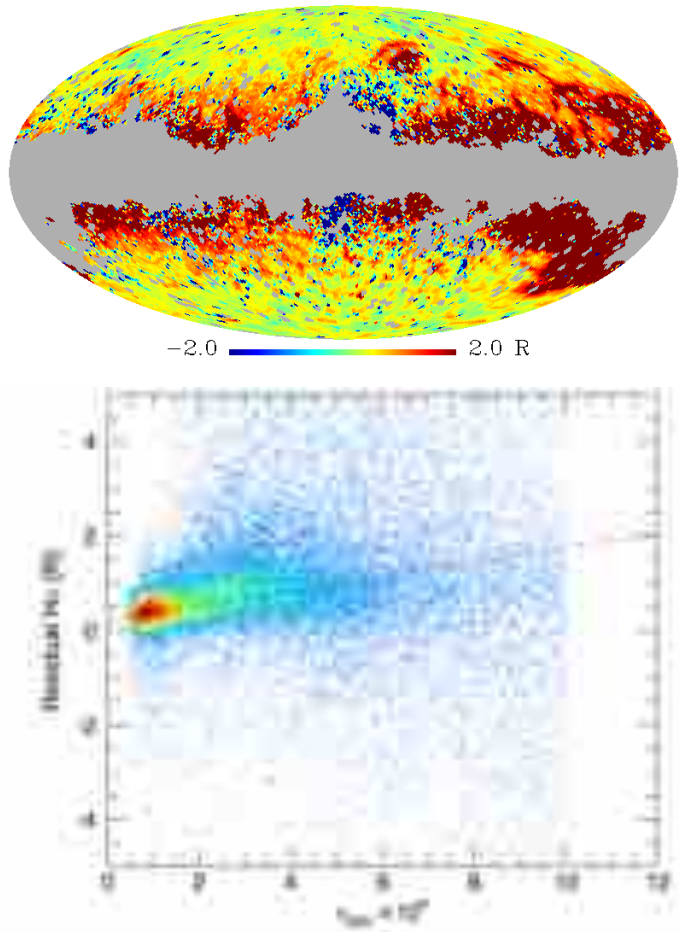

Fig. 6. *Top*: residual Hα emission after subtraction of the scaled free-free component. *Bottom*: scatter plot of the residual Hα intensity against the thermal dust optical depth at 353 GHz outside the mask shown above, corresponding to $A(\mathrm{H}\alpha) \lesssim 0.53$ ($\tau_{353} < 1 \times 10^{-5}$). The best-fitting linear relation is shown as a dashed line.

that 1/3 of the dust lies in front of the Hα-emitting gas (see Dickinson et al. 2003), we find $f_{\mathrm{scatt}} = (36 \pm 12)\%$.

Our constraints are clearly not very tight, and are dependent on our assumption on the mean electron temperature and on the level of dust absorption. Given the relatively large uncertainties, an electron temperature of about 5000 K would be enough to bring the ratios within the 1σ uncertainty of the observed range.

We now explore the correlation between the residual Hα emission and the dust optical depth at 353 GHz. Scattering by dust grains should produce a positive correlation between these two maps. We plot this in the bottom panel of Fig. 6, where for low values of the opacity, $\tau_{353} \lesssim 1 \times 10^{-5}$, the correlation is indeed positive. The large dispersion of the points in the figure is a consequence of the noise and variations of electron temperature at high Galactic latitude. In spite of that, a significant correlation is observed. This suggests that the effect of scattered Hα light might be real and that its effects must be taken into account to determine precise values of T_{e}. But we remind the reader that this could also partly be explained by the regions corresponding to ≈0.5–1 *R* (at high Galactic latitudes, $|b| \gtrsim 40°$, where the positive correlation is observed) having a lower than average value for T_{e}.

We do not find strong evidence for high latitude regions with a scattered light fraction of around 50%. We also do not see an anti-correlation of the free-free-to-Hα ratio with the thermal dust optical depth (a proxy for column density of dust), as would be expected if there were a significant fraction of scattered light. We hypothesize that the electron temperature at our exact Galactic position could be slightly lower than expected (say 6000 K), which would reduce f_{scatt} to ≈10%.

4.1.2. Free-free emission in the plane

Along the Galactic plane, the Hα line is highly absorbed by dust and thus fails to provide a reliable measure of the free-free emission (Dickinson et al. 2003). In this region of the sky, we can use RRLs to estimate the thermal continuum emission and compare with the `Commander` free-free solution. The integrated RRL brightness is proportional to the free-free continuum in exactly the same way as for the optical Hα recombination line.

We use the data from the H I Parkes All-Sky Survey (HIPASS; Barnes et al. 2001) of the southern sky, which have been re-analysed to extract RRLs at 1.4 GHz to produce the first continguous RRL survey of the Galactic plane (Alves et al. 2015). The full survey covers the longitude range 196° → 0° → 52° and $|b| \leq 5°$, with an angular resolution of 14′.4. The intensity calibration is good to better than 10%.

Figure 7 shows maps of the free-free emission from the `Commander` fit and from the RRLs. The free-free amplitude is converted from the RRL temperature assuming a simple model for T_{e}, based on an assumed temperature gradient of $(500 \pm 100)\,\mathrm{K\,kpc^{-1}}$ with distance from the Galactic centre (Alves et al. 2015). The Galactocentric distance at each longitude is estimated based on the Fich et al. (1989) rotation curve and using the central velocity of the RRLs. Obviously this is a crude approximation, since the RRL is a line-of-sight integral weighted by n_{e}^2 and individual lines of sight could have a range of values. We estimate that the electron temperatures for a given line-of-sight are uncertain at the ±1000 K level, which corresponds to an uncertainty in the free-free amplitude of up to 20%. Thus the overall uncertainty on the free-free amplitude from the RRL data is 25% at most. Nevertheless, there is an overall good level of agreement between the two estimates, both in terms of morphology and amplitude. A combination of bright compact sources (H II regions) and diffuse emission within about ±1° of the plane contribute, particularly in the inner Galaxy (l = 300° → 0° → 60°). In the outer Galaxy (l < 300°) the free-free emission is much weaker and only a few moderately bright H II regions can be seen.

The scatter plots of Fig. 8 indicate that the two data sets are highly correlated, which suggests that the component separation of the free-free emission from the other components has been relatively successful. However, there are clearly changes in slope from region to region. In general, the slopes are greater than 1, indicating that the `Commander` free-free map is, on average, brighter that the predicted RRL map. The best-fitting slopes are typically 50% higher than the predicted values.

Figure 9 shows longitudinal slices across the Galactic plane (b = 0°) at 1° resolution. The bright H II regions are clearly visible as bright peaks. Virtually all the bright peaks in the `Commander` free-free solution have a counterpart in the RRL prediction. These peaks sit on diffuse emission that should be subtracted before a comparison of peak temperatures is made; large-scale (≳4°) emission will not be reliable in the RRL data (Alves et al. 2015). Many of the peaks have comparable amplitudes, while some of them are discrepant by up to a factor of 2. We note that the Galactic centre (l = 0°) is low in the RRL map due to receiver saturation artefacts. The ratio of free-free to RRL brightness for the brightest 6 peaks in the first region

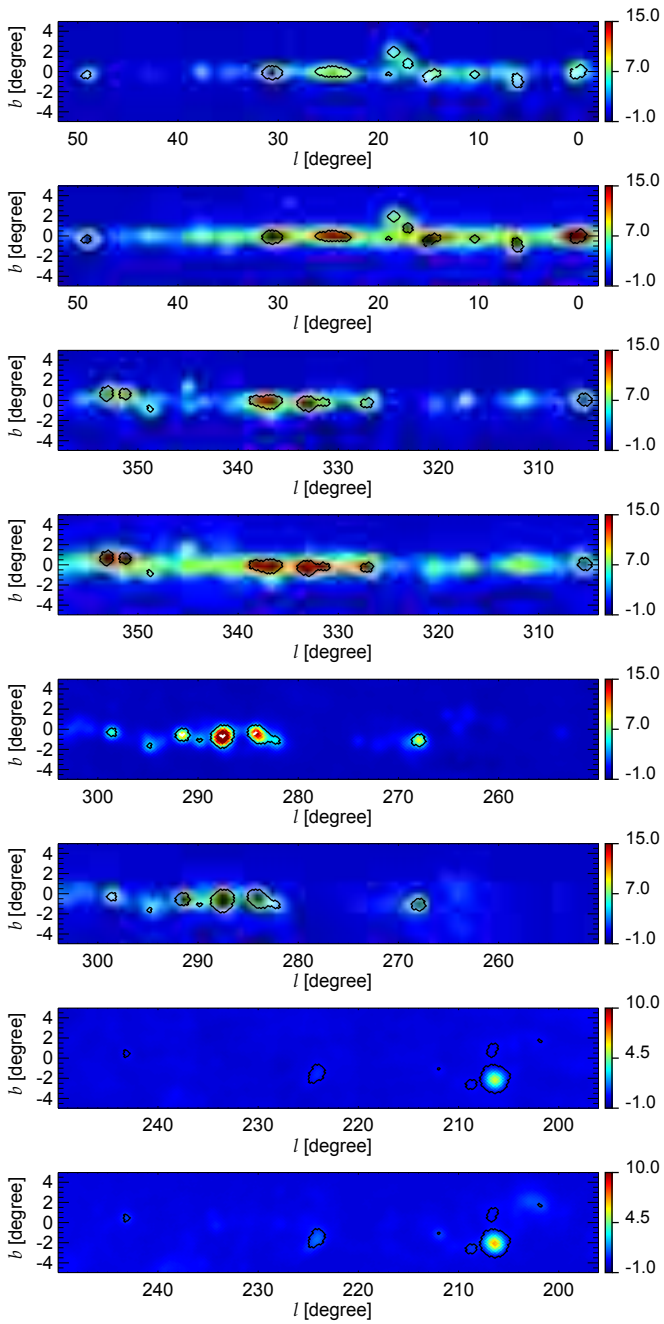

Fig. 7. Maps of the free-free emission along the Galactic plane, separated into four different longitude ranges. For each l-range, the RRL and Commander estimates are shown in the *top and bottom panels*, respectively. The maps are in units of K at 1.4 GHz and at 1° resolution. There is a single contour for each pair of panels, set at a value corresponding to the minimum temperature of the 2% brightest pixels of the RRL map, corresponding to 7.4, 9.6, 4.4, and 0.4 K, from *top to bottom*, respectively. The white pixels at the location of some bright H II regions in the maps of the first, third and fifth rows, correspond to saturated pixels in the RRL survey.

($l = 358° \rightarrow 0° \rightarrow 52°$, excluding the $l = 0°$ peak) is 1.14 ± 0.04, while the next 10 brightest peaks have a ratio of 1.36 ± 0.08 (the uncertainty is the rms scatter of the ratios).

The discrepancy between the two free-free estimates on bright H II regions, which has been noted before (Alves et al. 2010; Planck Collaboration Int. XIV 2014; Planck Collaboration Int. XXIII 2015), is presumably due to a combination of effects: (i) differences in the electron temperature used to estimate the free-free brightness; (ii) beam effects in the RRL map. The RRL data are calibrated in the full beam scale, such that the flux density of compact sources is underestimated by 10–30% depending on their size, although the longitude profiles of Fig. 9 suggest that the discrepancy between the Commander and RRL maps across individual sources does not depend on their extent; and (iii) residual emission in the Commander map, e.g., at $(l, b) = (46.^\circ8, -0.^\circ3)$ associated with the HC30 supernova remnant.

Compared to the brightest sources in each region, the weaker diffuse emission appears to have an even steeper slope, approaching 2, i.e., the discrepancy between the RRL and Commander solution is worse for very extended emission. This is likely to be due to excess synchrotron radiation at higher frequencies that has been accounted for in the simple Commander model by the free-free component. In particular, the synchrotron component is effectively modelled as a power law in frequency with a fixed spectral index, while there is considerable evidence for spectral flattening of synchrotron emission at low latitudes (Kogut et al. 2007; de Oliveira-Costa et al. 2008; Gold et al. 2011; Planck Collaboration Int. XXIII 2015). This will contribute to some level of excess emission at frequencies 20–100 GHz, which can result in an apparent increase in the free-free and/or AME amplitude in the Commander fits, an effect that can be seen as a broad background (zero-level) in the longitude plots of Fig. 9. We also note that the RRL data will not reliably trace large-scale ($\gtrsim 4°$) emission, since the observations were made in $8° \times 8°$ patches of sky.

In summary, the Commander free-free map appears to be a reliable tracer of the brightest H II regions, with an accuracy of around 20%. Weaker emission regions appears to be overestimated by up to a factor of 2, relative to estimates using RRL data. As mentioned in Planck Collaboration X (2016), including new data in the frequency range 2–20 GHz will yield improved component separation products, particularly for synchrotron and AME, which in turn will improve the accuracy of the free-free solution.

4.2. Anomalous microwave emission

Commander models the AME as spinning dust, which for uniform conditions (grain size distribution, ambient radiation) gives a relatively sharply peaked spectrum; specifically it uses the SpDust2 code (Ali-Haïmoud et al. 2009; Silsbee et al. 2011) to calculate a template spectrum using parameters typical for the diffuse cold neutral medium (Draine & Lazarian 1998). To tolerable accuracy for present purposes, models for other phases can be approximated by scaling the template in frequency.

As shown in Sect. 3, the AME spectrum is quite variable, with an apparent tendency to peak at substantially higher-than-average frequencies around some H II regions. Low-latitude lines-of-sight will therefore contain AME with a range of peak frequencies, which will give a broader spectrum that *cannot* be fitted by a frequency-shifted template. In fact, a superposition of AME spectra with a distribution of peak frequencies could approximate a power law over the frequency range of primary interest here (20–70 GHz). Such a general model could not be constrained by the available data, but we take a step in this direction by using two AME components in the Commander fit, each based on our SpDust2 template. One component (which generally dominates) is scaled in frequency at each pixel, with a Gaussian prior for the frequency of the intensity peak, $\nu_{\rm p1}$, of (19 ± 3) GHz. The peak frequency of the other component

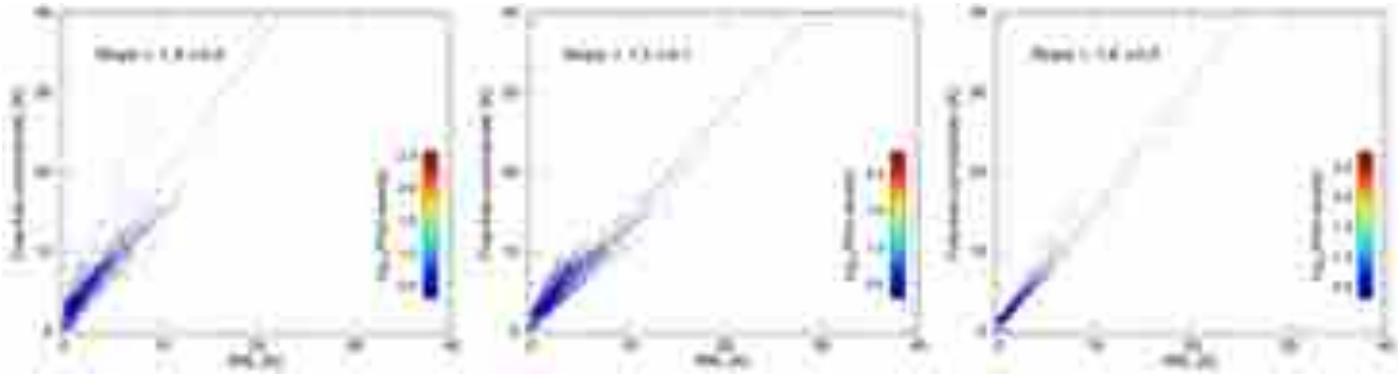

Fig. 8. Scatter plots of the Commander versus the RRL free-free map for three regions of the Galactic plane (the first three regions shown in Fig. 7). The slope values given in each panel result from a linear fit to all the data points.

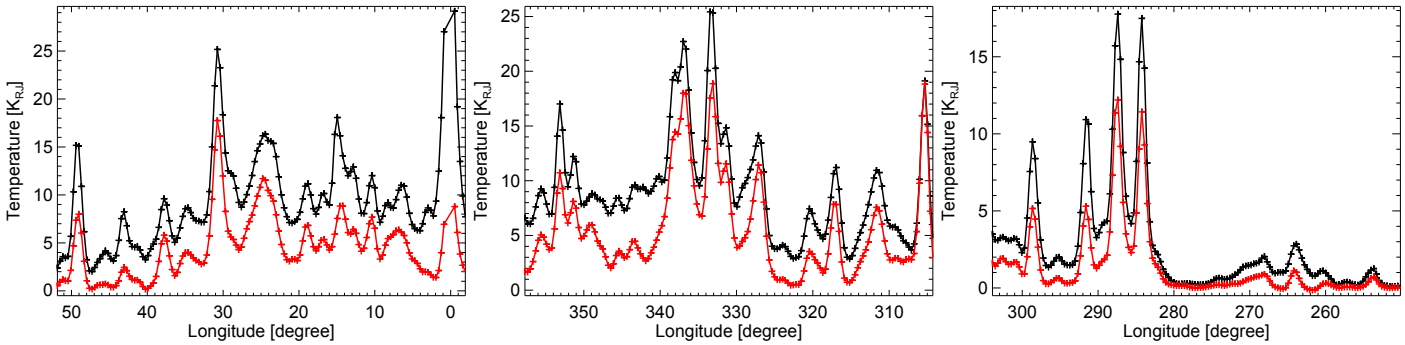

Fig. 9. Longitude profiles of the Commander (black) and RRL (red) free-free maps, averaged within $|b| \leq 1°$, for three regions of the Galactic plane (the first three regions shown in Fig. 7). The comparison is for the bright compact regions that show as peaks on top of a broad baseline level due to extended emission.

is assumed to be constant over the whole sky with a value to be determined globally; in this Commander solution the result is $\nu_{p2} = 33.35$ GHz. This second model component is there to account for the broadened spectrum of the overall AME emission, and should not be interpreted as a physically distinct AME component; in this paper (as in Planck Collaboration X 2016) we only consider the combination of the two components, which we evaluate at 22.8 GHz to allow comparison with earlier studies.

The all-sky map of AME as fitted by Commander is shown in Fig. 10. The foreground emission detected at frequencies around 20–60 GHz in the WMAP/*Planck* maps appears to be dominated by AME (e.g., Davies et al. 2006; Ghosh et al. 2012; Sect. 3 of this paper). It has been detected with high significance over a large area of the sky. The strongest emission is observed in the Galactic plane, particularly in the inner Galaxy ($l = 300° \rightarrow 0° \rightarrow 60°$). The AME in the inner plane was identified and discussed by Planck Collaboration XXI (2011) and Planck Collaboration Int. XXIII (2015). The map also shows clear, strong AME in many of the molecular cloud regions that are well known to exhibit AME, including the Perseus and ρ Ophiuchus clouds. While previous *Planck* AME papers (Planck Collaboration XX 2011; Planck Collaboration Int. XV 2014) focused on compact AME regions, here we also look at diffuse AME regions away from the Galactic plane ($|b| > 10°$). We identify strong diffuse AME in the Chameleon/Musca regions as well as the Orion complex, which is discussed later in this section. These regions are less likely to be affected by foreground degeneracies than others: regions such as the Auriga dust feature above the Galactic centre and a large structure around the North Celestial pole can also be seen in the AME map, however they overlap with significant sources of synchrotron emission.

Overall there is a high level of correlation of AME with the thermal dust maps made at higher frequencies of *Planck* and in the infrared; however, the AME clearly cannot be accounted for by the Rayleigh-Jeans tail of the thermal dust emission, which is at least a factor of 30 below the AME component at 30 GHz. At low Galactic latitudes ($|b| \lesssim 10°$) and in bright compact and diffuse AME regions, the complexity of separating AME from CMB, synchrotron, and free-free emission is the dominant uncertainty for the Commander solution. At high latitude, where the AME is weak, the Commander solution is dominated by instrumental noise. The Commander AME map also contains residual extragalactic source contributions when their spectrum is intermediate between the assumed synchrotron and free-free models (e.g., Centaurus A is clearly visible, as are bright radio sources such as 3C 273); to remove these we mask sources in the PCCS2 catalogue at 28.4 GHz that are brighter than 1 Jy.

We evaluate the peak frequency of the combined AME spectrum for each pixel. The mean and median across the whole sky are 20.6 and 20.4 GHz, respectively, and at $|b| > 10°$ they are 20.5 and 20.2 GHz, respectively. Apart from bright regions, the peak frequency map is very noisy, largely constrained by our prior on ν_{p1} around 19 GHz (see Sect. 4.1 and Fig. 16 of Planck Collaboration X 2016) and contains residual signal from point sources. Regions such as Perseus, ρ Oph and Orion have higher than average peak frequencies, around 25–30 GHz, in agreement with previous analyses (e.g., Planck Collaboration XX 2011). In some places the fits are dominated by the second AME component (notably the Sh 2-27 and southern Gum nebulae). This is consistent with the ILC analysis of Sect. 3, although in reality some of these regions have even higher peak frequency, e.g., Planck Collaboration Int. XV (2014) found a

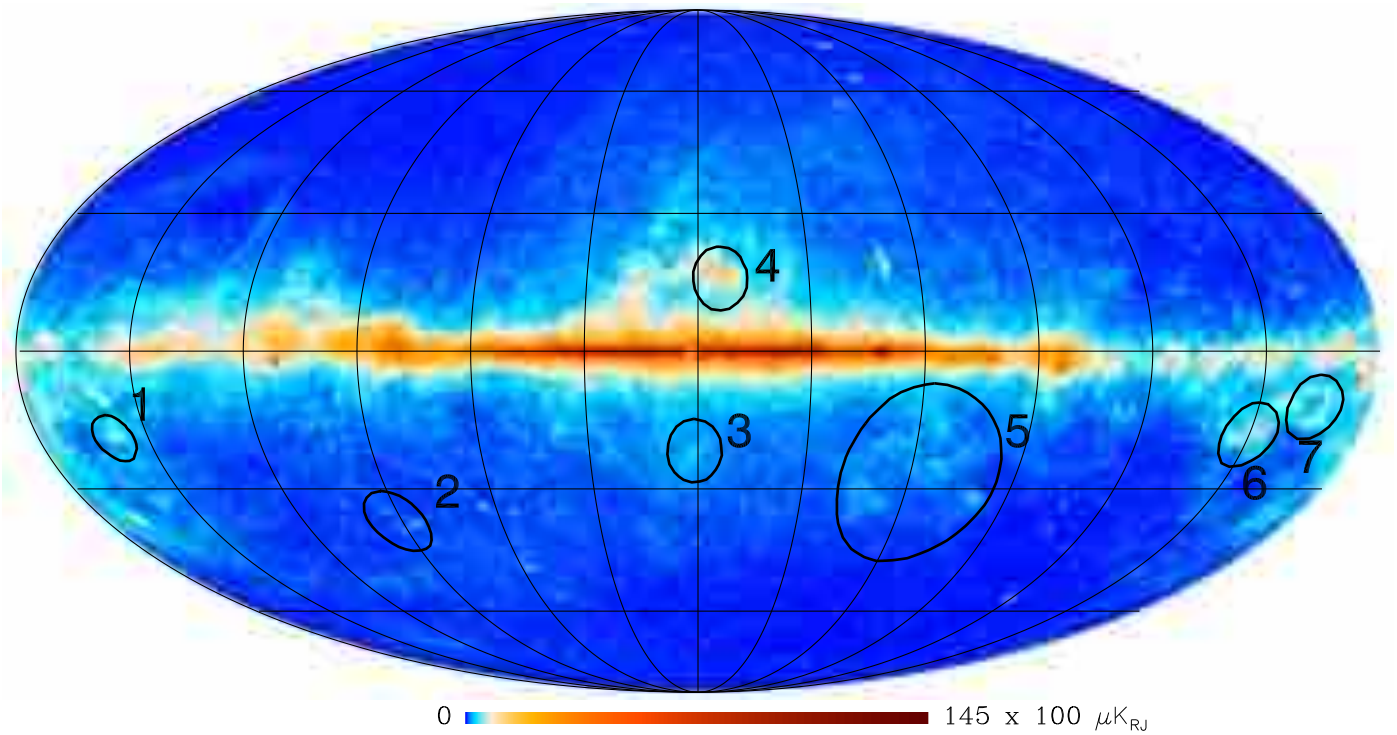

Fig. 10. All-sky map of AME from Commander at 22.8 GHz plotted using a Mollweide projection, with a 30° graticule and an asinh colour scheme. Seven regions of diffuse AME have been highlighted, and are discussed in the text.

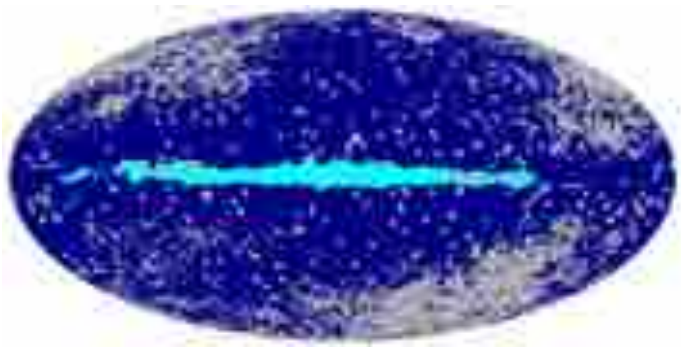

Fig. 11. Mask used for the AME T–T plots. The regions in grey are masked in the T–T plots. The region in light blue shows where the AME at 22.8 GHz is brighter than 1 mK; this is also masked when determining the best-fitting emissivity. We also mask the ecliptic plane ($|\beta| < 20°$) when analysing the IRAS and WISE data.

best-fitting value of ν_p of 50 GHz for the California Nebula. Sh 2-27 has an exceptionally high χ^2 in the Commander fit (Planck Collaboration X 2016, Fig. 22), which we found can be alleviated by allowing a similar peak frequency (recall that in our baseline Commander model ν_{p2} is fitted globally to keep the number of free parameters acceptable). Dobler & Finkbeiner (2008b) previously found a bump at ~50 GHz in the SED of Hα-correlated emission from the Warm Ionized Medium that they speculated could be a high-frequency spinning dust component, which is likely the same emission we are seeing here. We find that in bright free-free regions (primarily on the plane, but also bright high-latitude regions such as M 42 and the California nebula) the AME peak frequency correlates with the free-free amplitude (at 22.8 GHz) with a best-fitting slope of (0.066 ± 0.012) GHz mK^{-1}, which may be an indication of the importance of the interstellar radiation field in the excitation of AME carriers (e.g., Tibbs et al. 2013).

4.2.1. All-sky correlations

In order to look at the correlation of the AME with other components, we have degraded the AME map and other tracer maps to $N_{side} = 64$ (pixel widths of 55′). We define a mask, shown in Fig. 11, to exclude pixels where the S/N for AME is less than 3.0 and point sources brighter than 1 Jy, except at $|b| < 5°$ to avoid masking Galactic plane sources. However, we mask five Galactic plane regions containing the brightest H II complexes (e.g., Cygnus-X) in the sky. We use a 3° radius disc centred at (l, b) = (49.°6,−0.°6), (79.°2,0.°4), (268.°2,−1.°3), (287.°5,−1.°1) and (291.°8,−0.°9). These are particularly bright in the IRAS 12 and 25 μm maps, where there could be contamination by starlight and/or line emission. We show the T–T plots for the entire sky outside of the mask for different potential tracers in Fig. 12. We also test the effects of additionally masking the Galactic plane ($b < 10°$). We calculate the emissivity, i.e., the ratio of AME emission compared to AME tracers, from the slope of the best-fitting line as shown in the T–T plots for pixels where the AME amplitude at 22.8 GHz is less than 1 mK (shown in light blue in Fig. 11). The difference between the Commander maximum-likelihood and mean solutions for the AME component is around 5–6%, depending on frequency, due to the non-Gaussian shape of the probability distribution. We therefore assume a conservative 10% modelling uncertainty on top of the Commander component uncertainty maps; we also assume a 13.5% calibration uncertainty for the IRAS 100 μm map (Miville-Deschênes & Lagache 2005).

We find an excellent correlation ($r = 0.98$) with the *Planck* map at 545 GHz, shown in Fig. 12a, which is predominantly thermal dust emission. A mean emissivity of (65±7) μK (MJy sr^{-1})$^{-1}$ is found ((70 ± 7) μK (MJy sr^{-1})$^{-1}$ when the Galactic plane

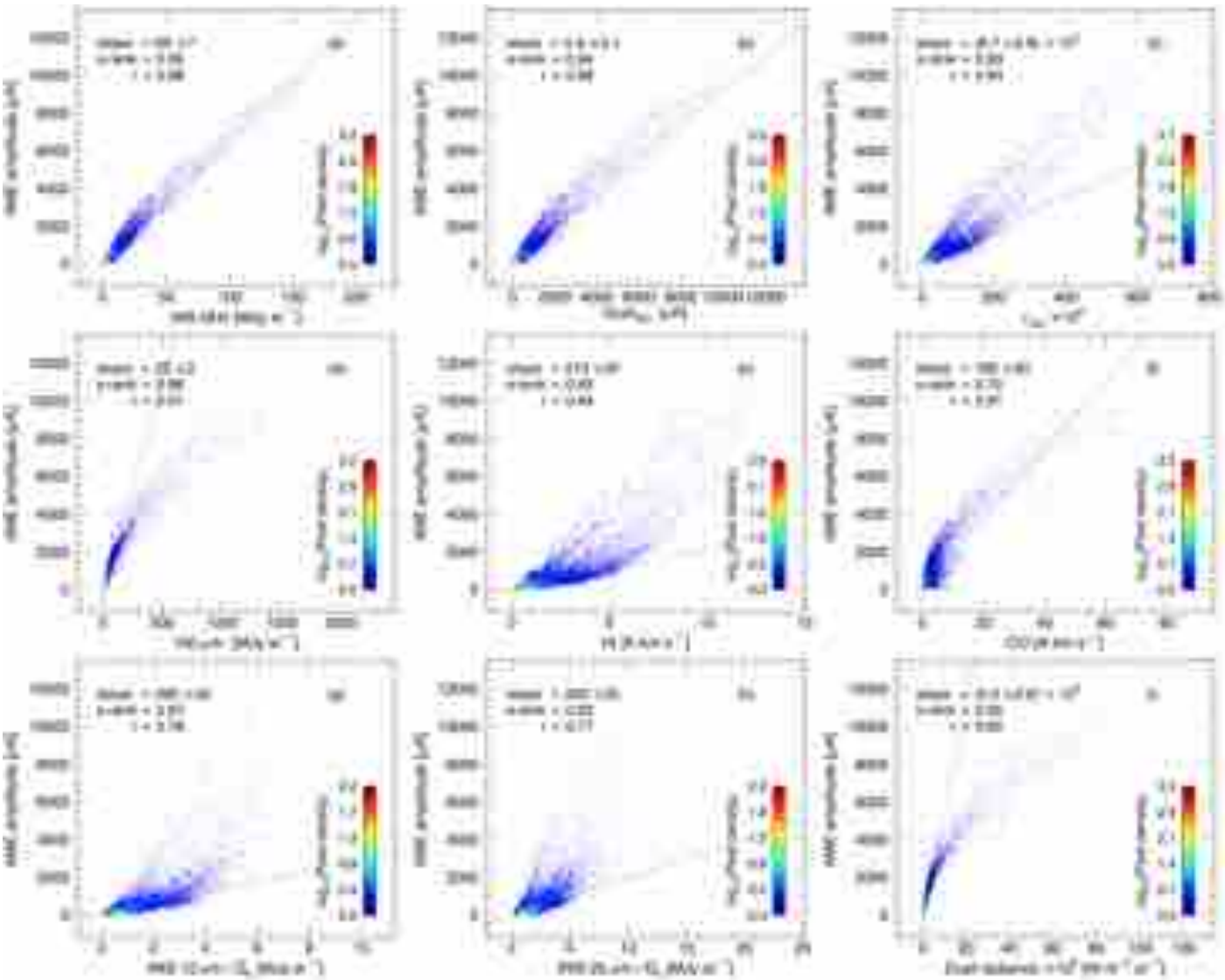

Fig. 12. T–T plots at $N_{\rm side} = 64$, using the mask shown in Fig. 11. The best-fitting lines and emissivities shown are determined where the AME amplitude is less than 1 mK. The Spearman's rank correlation coefficient (s-rank) and the Pearson's correlation coefficient (r) are also shown. *Top row*: AME (μK at 22.8 GHz) compared to: **a)** *Planck* 545 GHz (MJy sr^{-1}); **b)** the `Commander` thermal dust solution at 353 GHz (μK); and **c)** τ_{353} (rescaled by 10^5). *Middle row*: **d)** 100 μm (MJy sr^{-1}); **e)** H I (K km s^{-1}); and **f)** CO $J = 2 \rightarrow 1$ (K km s^{-1}). *Bottom row*: **g)** IRAS 12 μm (MJy sr^{-1}) divided by G_0; **h)** IRAS 25 μm (MJy sr^{-1}) divided by G_0; and **i)** dust radiance calculated from the `Commander` products.

is masked), which is consistent over a wide range of amplitudes. The overall emissivity against IRAS 100 μm that we find when looking at the entire sky is $(22 \pm 2)\,\mu$K (MJy sr^{-1})$^{-1}$ (Fig. 12d), with $r = 0.91$; this is somewhat lower than the weighted average found by Planck Collaboration Int. XV (2014) of $(32 \pm 4)\,\mu$K (MJy sr^{-1})$^{-1}$, although the latter is for a specific set of 27 low-latitude clouds selected for significant emission, rather than an all-sky average. Davies et al. (2006) used template fitting to estimate the emissivity of AME compared with thermal dust; they calculated the emissivity in terms of the "FDS model 8" dust map at 94 GHz (Finkbeiner et al. 1999), which can be multiplied by a factor of 3.3 to obtain the equivalent 100 μm emissivity (on average). Our analysis agrees well their results, where they found $(21.8 \pm 1.0)\,\mu$K (MJy sr^{-1})$^{-1}$ across the whole sky outside of the WMAP Kp2 mask, and an average of $(25.7 \pm 1.3)\,\mu$K (MJy sr^{-1})$^{-1}$ in the 15 regions they examined. We note that this good agreement in the overall high-latitude emissivity comes from different component-separation methods.

For thermal emission tracers there is some curvature in the relation at the brightest pixels, where there is less AME for a given amount of thermal dust emission. This is more noticeable in the 100 μm correlation than the 545 GHz correlation, because the 100 μm amplitude is much more affected by the temperature of the thermal dust grains than the 545 GHz emission (Tibbs et al. 2012), which increases towards the Galactic plane (e.g., Planck Collaboration XIX 2011). This effect is not seen in the τ_{353} correlation, however there is a much larger scatter in the τ_{353} correlation, as well as a trend towards there being more AME per unit τ_{353} at high optical depth.

There is a good correlation ($r = 0.84$) with H I emission integrated in the velocity range $[-450, +400]$ km s^{-1} from the LAB survey (Kalberla et al. 2005), shown in Fig. 12e, with a slope of $(210 \pm 20)\,\mu$K K^{-1} ($(280 \pm 30)\,\mu$K K^{-1} when the Galactic plane is masked); there is also a noticeable upturn and increase in the scatter of points in this relation above an H I integrated velocity intensity of around 3 K, in agreement with previous results (e.g.,

Lagache 2003). Planck Collaboration Int. XVII (2014) compared *Planck* and WMAP data to H I data, and found an emissivity of $(1.75 \pm 0.14) \times 10^7\,\mu\mathrm{K}\,\tau_{353}^{-1}$ [7]; they also considered AME models, which gave slightly lower emissivities with τ_{353} of $1.3 \times 10^7\,\mu$K. We find an emissivity against τ_{353} of $(8.7 \pm 0.8) \times 10^6\,\mu$K (Fig. 12c, $(1.1 \pm 0.1) \times 10^7\,\mu$K excluding the Galactic plane), which is lower than the values found by Planck Collaboration Int. XVII (2014) by a factor of 1.5–2.1. However, the emissivities have not been calculated on the same areas of sky, and this difference is within the variations of $E(B-V)/N_{\mathrm{H}}$ reported in Planck Collaboration XI (2014). We also compare AME at 22.8 GHz with the Commander thermal dust solution at 353 GHz and find a slope from the regions of $(0.9\pm0.1)\,\mathrm{K\,K^{-1}}$ (Fig. 12b, $r = 0.98$, $(1.0\pm0.1)\,\mathrm{K\,K^{-1}}$ excluding the Galactic plane); this is also slightly lower than the value of $(1.12 \pm 0.03)\,\mathrm{K\,K^{-1}}$ found by Planck Collaboration Int. XXII (2015).

The upturn in the H I correlation implies that the AME is related to another phase that is not traced by H I emission. We also look at CO emission, which will trace denser regions, and is a marker for H II emission. The correlation with the Commander CO $J = 2 \rightarrow 1$ map is rather more complicated than the other correlations, however. The best-fitting slope is $(180 \pm 20)\,\mu\mathrm{K}\,(\mathrm{K\,km\,s^{-1}})^{-1}$ (Fig. 12f), with $r = 0.91$, reducing to $(150 \pm 20)\,\mu\mathrm{K}\,(\mathrm{K\,km\,s^{-1}})^{-1}$ when the Galactic plane is masked. However, at low amplitudes the emissivity is clearly a lot lower than the best-fitting value, and at high amplitudes it is clearly higher than the best-fitting value. This could be due to component separation issues; alternatively, since the curvature largely takes place at AME amplitudes above 1 mK, it may indicate that there is less AME in the densest parts of the Galaxy than at higher latitudes.

We have also looked at the correlations with the IRAS 12 μm and 25 μm data, which trace the very small dust grain population that could produce AME, as well as containing PAH line emission. Indications of an improved correlation with these data have been seen on smaller scales by e.g., Casassus et al. (2006). However, these data are considerably contaminated by zodiacal light and other systematics; as such, we have masked the ecliptic plane ($|\beta| < 20°$) before fitting these data. The resulting AME emissivity against 12 μm emission is $(460 \pm 60)\,\mu\mathrm{K}\,(\mathrm{MJy\,sr^{-1}})^{-1}$, with Pearson correlation coefficient $r = 0.93$ and Spearman's rank correlation coeffient $s = 0.71$, and against 25 μm emission is $(370 \pm 40)\,\mu\mathrm{K}\,(\mathrm{MJy\,sr^{-1}})^{-1}$, with $r = 0.87$ and $s = 0.52$. However, these will still include other systematic effects, such as stellar contamination and high-latitude zodiacal light. We nomalize the maps by the interstellar radiation field intensity, which we estimate by $G_0 = (T_{\mathrm{d}}/17.5)^{\beta+4}$ (Ysard et al. 2010), so that we are correlating against column density. Dividing by G_0 improves the correlation as measured by Spearman's rank, which includes the curvature in the correlation, while the Pearson's rank, which relies on a linear correlation, reduces. This improvement in correlation is as expected by the spinning dust model (Ysard et al. 2010), however the value of G_0, and hence the correlation coefficient, is highly dependent on the dust temperatures and spectral indices. The resulting emissivity against 12 μm is $(290 \pm 30)\,\mu\mathrm{K}\,(\mathrm{MJy\,sr^{-1}})^{-1}$ (Fig. 12g, $r = 0.78$, $s = 0.87$) and against 25 μm it is $(200 \pm 20)\,\mu\mathrm{K}\,(\mathrm{MJy\,sr^{-1}})^{-1}$ (Fig. 12h, $r = 0.77$, $s = 0.83$). We return to this topic in the discussion of the Musca region, below.

In a recent analysis, Hensley & Draine (2015) have compared the Commander AME maps with different potential tracers of AME, and find a good correlation against dust radiance. This is the integrated intensity from thermal dust, and it characterises the energy absorbed and emitted by the thermal dust particles. We have also compared the AME map with dust radiance (calculated using the Commander products and Eq. (10) in Planck Collaboration XI 2014) in Fig. 12i. We find a strong correlation at low amplitudes, with an emissivity against AME at 22.8 GHz of $(5.6 \pm 0.6) \times 10^8\,\mu$K, and $r = 0.90$. At higher amplitudes (i.e., in the Galactic plane), the dust radiance calculated using the Commander products turns over, in the same way as the correlation with the IRAS 100 μm data does, implying that this is due to temperature effects. If we use the radiance map from Planck Collaboration XI (2014), which includes the 100 μm map, in the analysis, this effect reduces in magnitude, but is still present.

Hensley & Draine (2015) also compare the variations in AME emissivities (defined by dividing the AME map by the average emissivity against dust radiance) with variations in the fraction of the WISE 12 μm data (Meisner & Finkbeiner 2014) that can be attributed to polycyclic aromatic hydrocarbon (PAH) emission, in contradiction with expectations from the spinning dust model where PAHs are though to be the spinning molecules. Using the Commander thermal dust amplitude and T_{d} and β_{d} maps from (Planck Collaboration XI 2014), they find no correlation between AME emissivities and PAH emission. We repeat their analysis, using the WISE 12 μm data and masking the Galactic plane ($|b| < 5°$) and the Ecliptic plane ($|\beta| < 20°$) in addition to the mask shown in Fig. 11. We find similar results when using the dust radiance maps calculated using the products from (Planck Collaboration XI 2014), with correlation coefficients of 0.10 (Planck Collaboration XI 2014 radiance map) and 0.23 (using the Commander dust amplitude). However, if we calculate dust radiance using only the Commander products, then we find a correlation with a slope of 1.1 ± 0.1, with a correlation coefficient of 0.52 [8]. Although the Commander dust radiance map will be biased low due to the absence of data points tracing warmer dust temperatures, this demonstrates the dependence of this result on the quality of the radiance map; it will also depend on the quality of the AME map. One possibility is that this correlation is affected by the large angular scale structure in the Galaxy; as such we return to this in the discussion of the Musca region, below.

In conclusion, we find the best correlation with AME at all amplitudes is from the 545 GHz *Planck* map, followed by the Commander dust solution at 353 GHz and the optical depth, τ_{353}. The dust radiance has a tight correlation with AME away the Galactic plane, but has a worse correlation in the plane. The correlation with 100 μm is significantly affected by temperature effects, which the choice of lower frequency thermal dust maps avoids. We find a reasonable correlation with H I emission, although this does not appear to correlate with the brightest AME emission, and with CO emission, although this is not well-fitted with a single emissivity. The correlation with dust radiance is very good at low amplitudes, but using a single emissivity would

[7] Planck Collaboration Int. XVII (2014) give a value of $(17 \pm 1)\,\mu\mathrm{K}\,(10^{20}\,\mathrm{H\,cm^{-2}})^{-1}$ at 23 GHz, which can be converted to $\mu\mathrm{K}\,\tau_{353}^{-1}$ using $E(B-V)/N_{\mathrm{H}} = (1.44 \pm 0.02) \times 10^{-22}\,\mathrm{mag\,cm^2}$ and $E(B-V)/\tau_{353} = (1.49 \pm 0.03) \times 10^4\,\mathrm{mag^{-1}\,cm^{-2}}$ (Planck Collaboration XI 2014).

[8] The first preprint version of Hensley & Draine (2015) used a full-sky WISE map that later turned out to be contaminated by *Planck* 857 GHz data on scales larger than 2°, which might also affect our analysis of their results. A revised version, Hensley et al. (2016), used an alternative approach to process the WISE data to avoid this issue; they found that their conclusions were unchanged. As such, we have not revised our conclusion here.

Table 2. *Top section*: emissivities of AME at 22.8 GHz (μK) relative to the Commander thermal dust amplitude at 545 GHz (MJy sr^{-1}), the IRAS map at 100 μm (MJy sr^{-1}), and the optical depth at 353 GHz, τ_{353}, for the regions shown in Figs. 10 and 13. *Bottom part*: emissivities from Davies et al. (2006, D06; whole sky and region mean) and Planck Collaboration Int. XV (2014, XV; Perseus, ρ Oph; and the unweighted region mean) for comparison.

Region	AME/545 GHz [μK (MJy sr^{-1})$^{-1}$]	AME/100 μm [μK (MJy sr^{-1})$^{-1}$]	AME/τ_{353} [μK 10^{-6}]
R1: Perseus	24 ± 7	12.3 ± 1.9	1.5 ± 0.9
R2: Plume	47 ± 6	18 ± 2	7.7 ± 1.0
R3: R CrA	36 ± 14	50 ± 12	4.1 ± 1.8
R4: ρ Oph	40 ± 9	4.6 ± 0.9	2.2 ± 1.2
R5: Musca	59 ± 8	26 ± 3	6.9 ± 1.0
Chamaeleon	74 ± 8	22 ± 2	11 ± 1.1
R6: Orion	47 ± 5	20 ± 2	4.7 ± 0.6
R7: λ Orionis	104 ± 11	25 ± 3	15 ± 1.8
LMC	56 ± 6	8.5 ± 1.0	7.9 ± 0.9
SMC	30 ± 9	4.7 ± 1.5	3.3 ± 1.0
Entire sky	65 ± 7	22 ± 2	8.3 ± 0.8
$\lvert b\rvert > 10°$	70 ± 7	21 ± 2	9.7 ± 1.0
XV: Perseus	...	24 ± 4	...
XV: ρ Oph	...	8.3 ± 1.1	...
XV: Mean	...	32 ± 4	...
D06: Kp2 mask	...	21.8 ± 1.0	...
D06: Region mean	...	25.7 ± 1.3	...

Notes. We also include emissivities for the LMC and SMC, discussed in Sect. 4.5.

over-predict the amount of AME present in the Galactic plane. We caution that these correlations will depend on the choice of mask due to large-scale biases, contamination from other emission mechanisms (e.g., point sources, zodiacal light, etc.), and variations across the sky.

4.2.2. Diffuse AME regions

We now move on to consider individual diffuse regions of AME. We have labelled seven regions in the all-sky AME map of Fig. 10 that demonstrate diffuse AME away from the Galactic plane and are in areas with relatively high S/N and clean component separation outputs. These include the well-known regions of Perseus and ρ Ophiuchus, as well as five new regions. In Fig. 13 we show the Commander solutions for synchrotron, free-free, AME and thermal dust, along with the CMB-subtracted 28.4 GHz *Planck* data and Hα data, for the new regions. In each of these maps, an area has been defined to analyse the properties of the region using T–T plots, and sources brighter than 5 Jy in the PCCS2 catalogue have been masked out to a radius of 60′, with some exceptions noted below. We show T–T plots between AME and thermal dust for three regions in Fig. 14. We use the best-fitting slope from these T–T plots to determine the emissivity of the AME component compared to the other components. Results for all regions are given in Table 2.

1. Perseus. This molecular cloud is a well-known source of AME (Watson et al. 2005; Planck Collaboration XX 2011). For the correlation analysis, we focus on an 8° × 8° patch centred on $(l, b) = (160.^\circ26, -18.^\circ62)$. Perseus is included in the PCCS2 catalogue, so we unmask the point sources when calculating the emissivities in this region. We find a lower emissivity for Perseus in the Commander products than in Planck Collaboration Int. XV (2014); this is due to leakage of around 40% of the AME emission to the free-free component, which also causes a decrement in the synchrotron map (see Fig. 33 below).

2. Pegasus plume. An example where the AME amplitude traces a filament-like structure at the edge of the Pegasus constellation at $(l, b) = (92°, -37°)$ and approximately 10° in length is shown in the first column of Fig. 13 (Region 2 in Fig. 10). We look at a 15° × 15° patch centred on this position. The plume was included in the CO catalogue of Magnani et al. (1985) as MBM 53–55 (G92.°97−32.°15, G92.°97−37.°54, and G89.°19−40.°94, respectively), and MBM 55 is also coincident with the H II region S 122 (G89.°18−41.°13) in Sharpless (1959). Fukui et al. (2014) have compared the CO emission to thermal dust emission as seen by *Planck* at 353–857 GHz. The structure can be seen clearly in the CMB-subtracted *Planck* 28.4 GHz map, which is very closely correlated with the thermal dust amplitude at 545 GHz. There is no visible emission in the synchrotron map and thus the signal in the AME map is unlikely to be due to synchrotron emission. The feature does have associated free-free emission, as traced by Hα; however, the brightness at 22.8 GHz is about 10 times greater than would be predicted for free-free emission, assuming a typical electron temperature ($T_e \approx 7000$ K). The plume structure is not resolved at 1° resolution, and therefore absorption of Hα light by dust should be similar to other high-latitude regions ($|b| > 30°$) at $\lesssim$0.1 mag, with only a small fraction being absorbed in compact high-density regions. The section of the plume corresponding to S 122 is definitely free-free emission; however, we conclude that the rest of this feature is predominantly AME, and that its appearance in the Commander free-free map is likely to be due to leakage from the AME component. This would be an interesting target for higher-resolution follow-up measurements, particularly in the bright region around MBM 53.

3. Corona Australis. The second column of Fig. 13 shows Corona Australis below the Galactic centre (Region 3 in Fig. 10). The region has been studied by Harju et al. (1993) in CO emission and with *Spitzer* by Peterson et al. (2011), and it is reviewed in Neuhäuser & Forbrich (2008). The central object is the R Corona Australis dark cloud (R CrA), which has a tail extending to the bottom-left of the maps consisting of the reflection nebula NGC 6729. The reflection nebula is illuminated by the early-type star TY CrA, and exhibits an extended 3.3 μm emission feature that could be to PAH emission (Chen & Graham 1993). We focus our analysis on a 3° × 3° area centred on $(l, b) = (1°, -22°)$ that encompasses the reflection nebula but not the R CrA cloud. The R CrA region is dominated by free-free emission, and it appears in both the Hα and free-free maps. However, the reflection nebula clearly shows AME, with a small amount of free-free emission seen in Hα (there is a feature in the tail in the Commander free-free map; this does not show up in Hα, however). The structure does not appear in the synchrotron map.

4. ρ Ophiuchus. This molecular cloud is another well-known source of AME (Casassus et al. 2008; Planck Collaboration XX 2011). It is included in the PCCS2 catalogue, so we unmask the point sources when considering this region. We look at a 5° × 5° patch centred on $(l, b) = (353.^\circ05, 16.^\circ9)$. We find a low

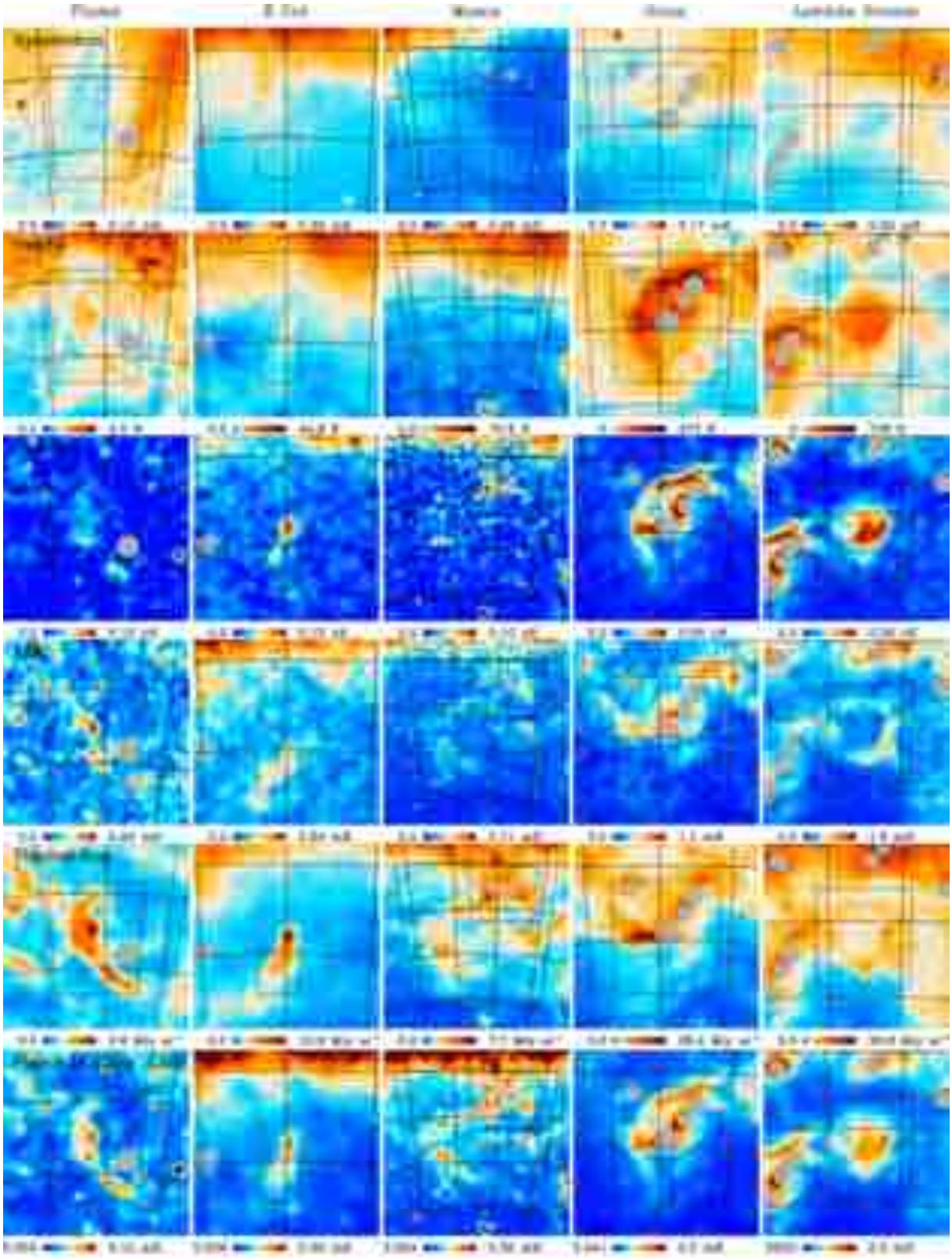

Fig. 13. `Commander` component maps for diffuse AME regions. From *top to bottom*: synchrotron amplitude (mK at 22.8 GHz), Hα (Dickinson et al. 2003, Rayleighs), free-free amplitude (mK at 22.8 GHz), AME amplitude (mK at 22.8 GHz), thermal dust amplitude (MJy sr^{-1} at 545 GHz), CMB-subtracted *Planck* 28.4 GHz map (mK). Column 1: a plume of emission in Pegasus, centred at $(l, b) = (91\overset{\circ}{.}5, -35\overset{\circ}{.}8)$. Column 2: the Corona Australis region at $(l, b) = (0^\circ, -18^\circ)$. Column 3: an extended region of emission in Musca/Chamaeleon, centred at $(l, b) = (305^\circ, -26^\circ)$ (the Large Magellanic Cloud can be seen to the bottom-right). Column 4: the Orion (M42) region of emission centred at $(l, b) = (209^\circ, -19\overset{\circ}{.}38)$. Column 5: the λ Orionis region at $(l, b) = (196^\circ, -12^\circ)$. The graticule separation is 10° in both directions, and the colour scales are asinh (although most are close to linear). The regions looked at for the correlation analyses are shown as black rectangular boxes.

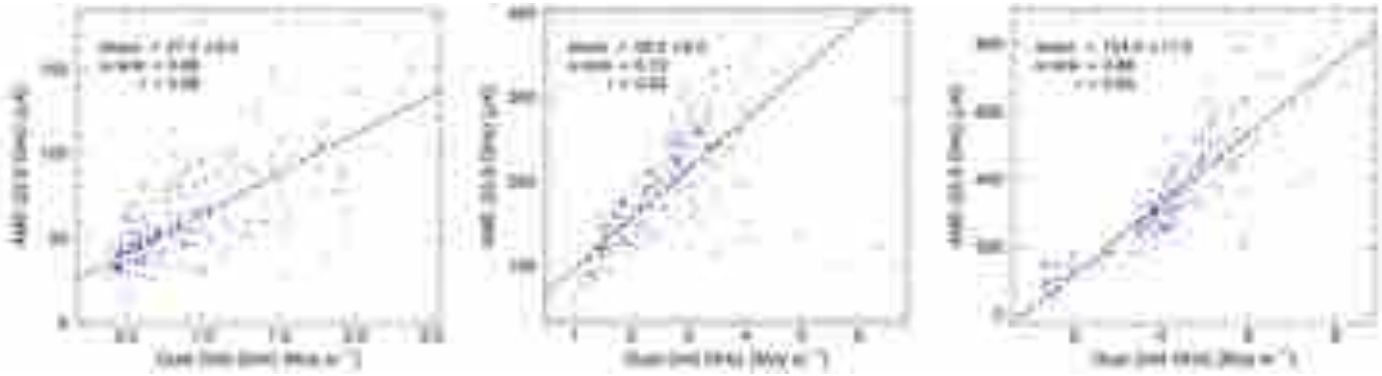

Fig. 14. T–T plots comparing the Commander AME map evaluated at 22.8 GHz to the Commander dust map at 545 GHz in three regions, as shown in Fig. 13. The best fit is shown as a dashed line. From *left to right*, for the Pegasus plume, Musca, and λ Orionis regions.

AME-100 μm emissivity of $(4.6 \pm 0.9)\,\mu\mathrm{K}\,(\mathrm{MJy\,sr^{-1}})^{-1}$, compared to $(8.3 \pm 1.1)\,\mu\mathrm{K}\,(\mathrm{MJy\,sr^{-1}})^{-1}$ from Planck Collaboration Int. XV (2014). This is due to significant leakage between the AME, free-free, and synchrotron components in the Commander solution in this region: half of the emission that has been attributed to AME in previous analyses (e.g., Planck Collaboration XX 2011) is instead attributed to free-free, causing a decrement in the synchrotron map, similar to the Perseus region (see Fig. 33 below). This issue is due to the complexity of this region, which lies within the Gould belt, where there is bright surrounding free-free and synchrotron emission.

5. Musca/Chamaeleon region. The third column of Fig. 13 shows a region of diffuse AME below the Galactic plane, in the Musca region close to the Magellanic clouds (Region 5 in Fig. 10). This region was previously studied in dust polarization by Planck Collaboration Int. XX (2015). Its distance is around 160–180 pc, and it contains three dark clouds (Whittet et al. 1997). We focus on a $15^\circ \times 12^\circ$ region centred on $(l, b) = (299^\circ, -16\overset{\circ}{.}5)$. The AME is clearly correlated with the dust emission, and there is a notable absence of emission in the synchrotron and Hα maps in this region. There is structure evident in the Commander free-free map; however, this correlates with some parts of the dust emission and not Hα, so it is likely to be AME rather than free-free. We mask two bright thermal dust sources in the Musca region (Cha I and Cha II) out to a radius of $80'$ when calculating the emissivities.

There is also a much larger AME half-ring that extends south of the Musca feature, into the Chamaeleon constellation. We include emissivities for the Chamaeleon region in a $35^\circ \times 30^\circ$ region centred on $(l, b) = (305^\circ, -25^\circ)$. We also use this region to look at the correlations between AME and IRAS 12 and 25 μm, since this part of the sky is at both high Galactic and ecliptic latitudes, and as such it is less contaminated by zodiacal or stellar light than the rest of the sky. We find an emissivity against 12 μm of $(550 \pm 60)\,\mu\mathrm{K}\,(\mathrm{MJy\,sr^{-1}})^{-1}$, and against 25 μm of $(570 \pm 70)\,\mu\mathrm{K}\,(\mathrm{MJy\,sr^{-1}})^{-1}$, both of which are higher than the all-sky values given earlier in this section. We also divide the 12 and 25 μm data by G_0 (as described above), after which we find an emissivity against 12 μm of $(250 \pm 25)\,\mu\mathrm{K}\,(\mathrm{MJy\,sr^{-1}})^{-1}$, and against 25 μm of $(159 \pm 16)\,\mu\mathrm{K}\,(\mathrm{MJy\,sr^{-1}})^{-1}$. That these numbers are lower than for the whole sky is likely to be an artefact in the G_0 map, which has a very small value due to the low Commander dust temperature in this region of around 17 K, compared to the mean temperature of 20.9 K. We also correlate the variations in AME emissivities with the fraction of PAH emission at 12 μm (as described above for the whole sky, following Hensley & Draine 2015) in this region. We find similar results to above, with a slope of 3.4 ± 0.4 when using the Commander radiance map, but poor correlations when using the radiance maps based on Planck Collaboration XI (2014). The correlations presented here are sensitive on how the comparison maps have been made, both in terms of inputs to the radiance map and contaminating emission in the IRAS maps.

6. Orion region. The fourth column of Fig. 13 shows the Orion region (Region 6 in Fig. 10). The strong free-free emission from M 42 and Barnard's Loop (Sh 2-276) is clearly visible. However, there is also an arc of AME emission that correlates with the high-frequency dust emission. This arc extends to lower longitude from M 42 along the integral-shaped filament to the dark cloud L 1641 and perpendicularly crosses over Barnard's loop (Orion Molecular Cloud A); in the other direction (Orion Molecular Cloud B) it extends up to M 78 to the top-right of the figure. The arc also appears faintly in free-free emission and in Hα. This dusty feature was recently mapped in 3D by Schlafly et al. (2015). We look at a $15^\circ \times 15^\circ$ region centred on $(l, b) = (209\overset{\circ}{.}01, -19\overset{\circ}{.}38)$, and we additionally mask M 42 to a radius of $100'$, and the point where the dust crosses the top part of Barnard's loop (where AME has likely leaked into the free-free map), when calculating the emissivities.

7. λ Orionis. The λ Orionis region (Region 7 in Fig. 10) can also be seen to the right of Barnard's Loop, and is shown in the fifth column of Fig. 13. We focus on a $13^\circ \times 13^\circ$ region centred on $(l, b) = (195\overset{\circ}{.}2, -12\overset{\circ}{.}2)$. This H II region (also known as S 264), which is illuminated by the O8 star λ Orionis, exhibits a shell of AME around the outside of the free-free region coincidental with the thermal dust ring. The dust ring has been previously noted in Maddalena & Morris (1987) and Zhang et al. (1989), and it has been observed in H I by Wade (1957) and CO by Lang & Masheder (1998) and Lang et al. (2000). The brightest AME regions in the ring are mostly located adjacent to bright thermal dust features, although the brightest AME region does not have a bright thermal dust counterpart. AME has been seen in PDRs around other H II regions at higher resolution, e.g., in ρ Ophiuchus (Casassus et al. 2008) and Perseus (Tibbs et al. 2010). λ Orionis has a particularly high emissivity against 545 GHz and τ_{353}, but the emissivity against 100 μm is comparable to the average; this indicates that the AME is connected to the colder dust in this region. It is likely that this region has not been identified

before due to the large free-free emission feature that the ring of AME surrounds.

There are significant differences between the emissivities for these seven regions. Some emissivities (particularly for Perseus and ρ Ophiuchus) are clearly biased low due to component-separation issues. Four are relatively consistent with values of AME/545 GHz typically in the range 40–50 μK (MJy sr^{-1})$^{-1}$. The notable exceptions are the emissivity values for λ Orionis and the Chamaeleon region, which are higher than the other regions by a factor of 2. However, except for λ Orionis and Chamaeleon, the emissivities are significantly lower than the average emissivity of $(65 \pm 7)\,\mu$K (MJy sr^{-1})$^{-1}$ across the whole high-latitude sky. The differences in emissivities could be a component-separation artefact, or they could be an indicator of the dependence of environmental conditions for the AME, or dust grain size distribution. For example, in nearby molecular clouds the AME carrier grains could have attached themselves to larger dust grains more than in the diffuse medium (e.g., Kim et al. 1994). We find a good correlation between the emissivities at 545 GHz and the optical depth.

In conclusion, we find that the `Commander` AME map provides a good tracer of AME in our Galaxy, however, there are significant degeneracies between the free-free and AME components that present difficulties when using the map to calculate emissivities. Additional all-sky data at frequencies of 5–20 GHz are needed to improve the free-free tracer and so enable a cleaner separation of AME from the other low-frequency components, in order to determine accurate emissivities and comparison with other data sets. In particular, λ Orionis is a distinctive region that warrants further study.

4.3. Synchrotron

In this section we discuss constraints on synchrotron emission derived from total intensity. We discuss options for modelling the form of the synchrotron spectrum, which is not a simple power law, and specify the model used in our baseline `Commander` analysis. The results are strongly limited by uncertainties in component separation; a much more reliable picture of the structure of the high-frequency synchrotron emission emerges from polarization data, discussed in Sect. 5. However, one advantage of total intensity is that we have a high S/N data set in the 408 MHz Haslam map, whereas in polarization all available ground-based sky maps are at low frequency and hence too strongly affected by Faraday rotation to be useful for spectral analysis. Because of residual differences between *Planck* and WMAP polarization maps (see Sect. 5.1 and Planck Collaboration X 2016), we do not attempt an independent fit of the spectrum of the polarized synchrotron emission.

The Galactic synchrotron spectrum curves significantly below a few GHz (e.g., de Oliveira-Costa et al. 2008; Strong et al. 2011). To generate a useful spectral constraint from just one low-frequency map, we cannot afford to fit this curvature independently at each pixel, as otherwise the low-frequency point would always fit perfectly and give no constraint on the high-frequency spectrum; instead we force the curvature to be constant across the sky, and we have tried several approaches to regularize the fit. As expected, simple power-law fits are inconsistent with our data, generating large and spurious "gain corrections" at 408 MHz.

Strong et al. (2011) and Orlando & Strong (2013) model the observed synchrotron emission for given Galactic magnetic fields and cosmic-ray (CR) propagation scenarios with the `GALPROP` code (Strong et al. 2007). This code solves the CR transport equation for any CR species, accounting for diffusion, reaccelerating processes, and energy losses in the interstellar medium. The CR transport properties are constrained by the local CR measurements and the observed ratio of secondary to primary nuclei, while energy losses are calculated for a given Galactic magnetic field. As implemented in the papers above, synchrotron `GALPROP` models aim to reproduce the large-scale emission, but not sub-kpc scale features such as the synchrotron loops and individual supernova remnants. The modelled local interstellar energy spectrum of leptons (after propagation effects) is adjusted to reproduce the direct measurements by Fermi-LAT above 7 GeV (Abdo et al. 2009; Ackermann et al. 2010). At lower energies, where solar modulation makes the local spectrum hard to determine, the lepton spectrum is based on synchrotron observations. In order to reproduce the curvature of the spectrum below a few GHz, Strong et al. (2011) found that the injected electron spectrum (before propagation effects) should have a break at approximately 4 GeV and should be harder than $p = 1.6$ below 4 GeV. Accounting for all these constraints, the resulting injected spectral index used in those works are ($N(E) \propto E^{-p}$) with $p = 1.6/2.5/2.2$, respectively, below/between/above the breaks at 4 and 50 GeV. Moreover, the cosmic ray lepton (CRL) spectral shape varies with Galactocentric radius due to propagation effects, CR source distribution, and the magnetic field strength. Despite these effects, the analysis in Strong et al. (2011) and Orlando & Strong (2013) finds that the spectral index at any given frequency is strikingly uniform across the sky: the spectral index between 408 MHz and 22 GHz has an rms dispersion of 0.02; between 22 and 70 GHz the rms is 0.01 (Fig. 15).

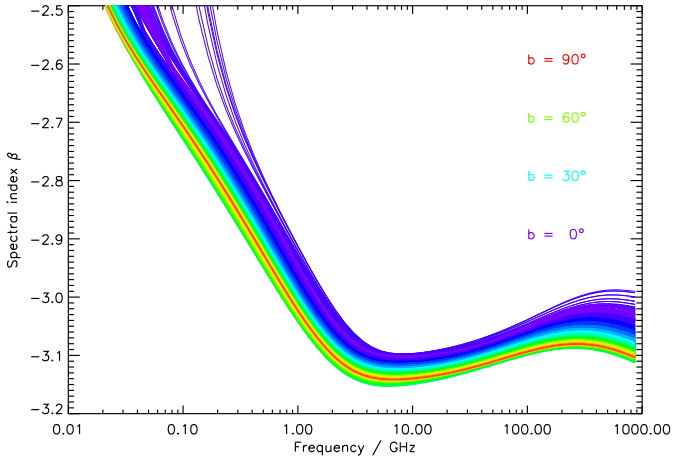

Fig. 15. Local spectral index of the synchrotron emission $\beta(\nu) = \mathrm{d}\ln T/\mathrm{d}\ln \nu$ vs. frequency for a sample of pixels (one per $N_{\rm side} = 8$ super-pixel), in the `GALPROP z10LMPD_SUNfE` model from Orlando & Strong (2013). The spectra are colour-coded by Galactic latitude: spectra at low latitudes show strong low-frequency curvature due to free-free absorption.

The uniformity of these model spectra over the sky contrasts with the much larger variation in $\beta(\nu)$ with frequency in the same models. For a given CRL spectrum, the frequency of synchrotron radiation scales directly with $B_\perp$, the component of the magnetic field perpendicular to the line-of-sight, and therefore the spectral index profiles shown in Fig. 15 will be shifted in log frequency by the change in $\ln B_\perp$. Given that $\mathrm{d}\beta/\mathrm{d}\ln \nu \approx -0.13$ at around 1 GHz, the spatial uniformity of the model spectral index implies that the average value of $B_\perp$ along each line-of-sight varies by at most 15% (rms) from one line-of-sight to another. Of course,

each model spectrum is an integral of the emission along the line-of-sight, along which $B_\perp$ varies considerably; however, the main variation of B is with Galactic scale height z, and hence all lines of sight, except those at very low latitude, sample nearly the same range of field strengths with nearly the same relative weighting. One might expect geometric factors alone to introduce significant spectral variations, but in these models the random component of the field dominates, so to a good approximation $B_\perp \approx \sqrt{2/3}\,|B|$.

The synchrotron intensity at fixed frequency depends on $B_\perp$ as $j_\nu \propto B_\perp^{-(\beta+1)}$, which suggests that regions of enhanced field strength will disproportionately dominate the emission. In the GALPROP models, the CRLs are supposed to diffuse efficiently through the interstellar medium, so that the local CRL density is not correlated in detail with the field strength. In reality, if the field is enhanced due to compression, e.g., by a shock wave, the CRLs will respond adiabatically if the time to diffuse out of the region is much longer than the timescale for compression. Then the particle energies will also be shifted to higher energies, giving a larger shift in the $\beta(\nu)$ profile, roughly $\propto B^2$, and $j_\nu \propto B^{-2\beta-3}$ (the exact index depending on the field geometry, see Leahy 1991 for details). Obviously this substantially increases the dominance of regions of high B in the overall synchrotron emission.

The spatial uniformity of the modelled synchrotron spectrum is thus likely to be an artefact due to the omission of sub-kpc structures in the models, such as the loops and spurs that dominate the high-latitude synchrotron sky. Indeed, we know that many individual supernova remnants (SNR) have spectra significantly flatter than that of the diffuse Galactic emission, as expected from the steepening caused by energy-dependent diffusion and radiative losses. It may seem redundant to argue on theoretical grounds that the GALPROP models show too little spectral structure, since much larger variations have been reported based on analysis of existing radio surveys (e.g., Lawson et al. 1987; Reich & Reich 1988; Dickinson et al. 2009). But if one discounts features associated with free-free absorption at very low frequencies and free-free emission at higher frequencies, the remaining large variations are mostly in the regions of lowest synchrotron intensity, which are susceptible to systematic errors such as sidelobe contamination from the strong Galactic plane emission, ground spillover, zero-level errors, and (at low frequencies) pick-up of sky emission reflected from the ground. Reich & Reich (1988) review previous large-area spectral index maps and conclude that all are unreliable, with the exception of the 38:408 MHz map of Lawson et al. (1987), which is strikingly uniform. Reich & Reich (1988) present their own map of spectral index between 408 and 1420 MHz in the northern hemisphere showing extensive regions at high Galactic latitude with $\beta > -2.4$, which they attribute at least in part to free-free emission uncorrelated with Hα, presumably due to extinction of the latter. They later extended their analysis to the full sky (Reich et al. 2004), finding even more extensive flat-spectrum regions in the southern hemisphere. If this were due to a free-free contribution, or even to an unusually flat synchrotron power law, the foreground temperature in the steradian or so around $(l, b) = (240°, -40°)$ would be several times higher than observed at 20–30 GHz (e.g., Fig. 1a). We believe that the culprit is likely to be some combination of the systematic errors mentioned above.

These considerations suggest two ways that our parameterized models can allow for larger spectral variations than found by Orlando & Strong (2013). To model emission from regions with B significantly different from the average, we can shift the spectrum in $\ln \nu$, keeping the overall shape fixed. However, there is certainly more spectral freedom allowed than this: from the dispersion in the spectral indices of young SNR, we expect the injected energy spectrum to be spatially and temporally variable; moreover the propagation effects included in the synchrotron models of Fig. 15 induce small variations in the high-frequency spectrum, which cannot be explained by variations in B. If we denote by $T_{\rm GP}(\nu)$ a fiducial spectrum from that simulation, then we can steepen or flatten it by writing

$$T_{\rm syn}(\nu) = (\nu/\nu_0)^{\delta\beta} T_{\rm GP}(\nu), \tag{4}$$

i.e., a change of local spectral index $\beta(\nu) = \mathrm{d}\ln T/\mathrm{d}\ln \nu$ by a constant $\delta\beta$. Most of the variation in Fig. 15 can be accounted for by such a model, but a larger range of $\delta\beta$ is needed to account for the actual sky. In practice, detailed accounting for the spectral curvature below 10 GHz is superfluous given that we only use one observed frequency in that regime. For our baseline Commander analysis our template was the spectrum of a single pixel in the z10LMPD_SUNfE model from Orlando & Strong (2013), chosen to be close to the all-sky median for several spectral parameters (i.e., knee frequencies, and spectral indices at the knees). As described in Planck Collaboration X (2016), this was fitted to the data along with the other foreground components allowing for a global shift in frequency (determined to be a factor of 0.26), and an amplitude that was fitted at each pixel.

The resulting synchrotron amplitude map (shown in Planck Collaboration X 2016) is essentially determined by the high S/N 408 MHz data, and deviates from it only in that residual free-free emission at 408 MHz is corrected (or over-corrected, at bright compact H II regions in which free-free absorption is significant at 408 MHz). The derived global frequency shift is surprisingly large and has the effect of steepening the average spectrum between 408 MHz and the *Planck* bands, resulting in a relatively low amplitude for synchrotron compared to AME and free-free. This may be because the fit is most strongly constrained by the North Polar spur and the diffuse halo of the inner Galaxy, the two regions that are both strong in synchrotron and relatively free of other components that could absorb errors in the synchrotron fit. Most analyses find flatter spectra in the narrow Galactic plane (e.g., Planck Collaboration Int. XXIII 2015).

Table 3. Key parameters of the WMAP MEM and MCMC foreground models (see Bennett et al. 2013a for details).

Model	$\beta_{\rm ff}$	$\beta_{\rm sync}$	AME
MEM	−2.15	−3.0	CNM, $\nu_{\rm peak}$ varies
MCMC-c base	−2.16	−3.0	...
MCMC-e sdcnm	−2.16	−3.0	CNM, $\nu_{\rm peak}$ fixed
MCMC-f fs	−2.16	varies	CNM, $\nu_{\rm peak}$ fixed
MCMC-g fss	−2.16	varies[a]	CNM, $\nu_{\rm peak}$ = 14.95 GHz

Notes. [(a)] As described in Strong et al. (2011).

4.4. Comparison with WMAP models

Here, we discuss the main similarities and differences between the low-frequency foreground component maps from our Commander analysis of the combined *Planck* and WMAP data sets (Planck Collaboration X 2016), and from the final WMAP analysis (Bennett et al. 2013a).

The WMAP team have published sets of component-separated maps using a maximum entropy method (MEM) and

Table 4. Ratios of the WMAP MEM and MCMC maps to the Commander maps for the high latitude sky with $|b| > 20°$ (*top*) and for $|b| < 20°$ (*bottom*).

Run	Sync		Free-free		AME	
	a	r	a	r	a	r
MCMC-c base	0.50	0.62	0.68	0.77	...	...
MCMC-e sdcnm	0.52	0.92	0.77	0.87	4.91	0.75
MCMC-f fs	0.52	0.62	0.80	0.77	3.18	0.67
MCMC-g fss	0.55	0.62	0.77	0.78	3.14	0.70
MEM	0.34	0.84	0.76	0.79	2.18	0.86
MCMC-c base	0.12	0.74	0.91	0.83	...	...
MCMC-e sdcnm	0.61	0.99	0.67	0.98	2.71	0.91
MCMC-f fs	0.13	0.78	1.09	0.89	4.71	0.86
MCMC-g fss	0.15	0.77	1.06	0.93	3.22	0.88
MEM	0.19	0.90	1.01	0.97	2.36	0.93

Notes. A value $a > 1$ indicates that the Commander maps contain more emission than the WMAP maps. The Pearson correlation coefficient (r) is also given.

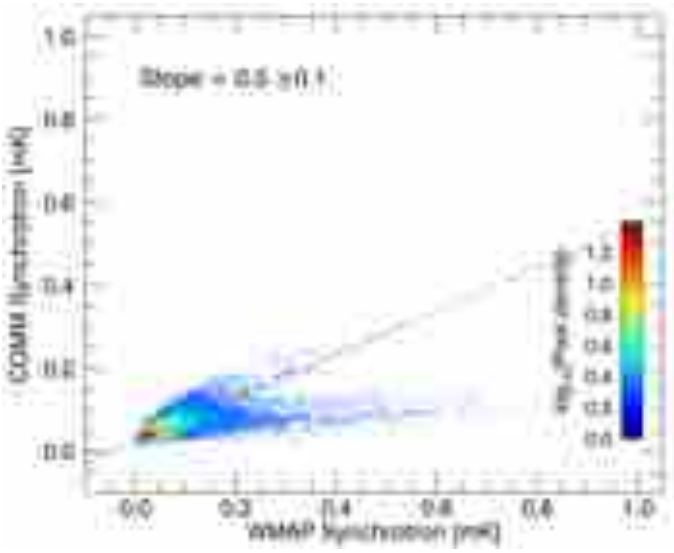

Fig. 16. Scatter plot between the Commander synchrotron solution evaluated at 22.8 GHz and the WMAP MCMC-f synchrotron model at the same frequency.

a Markov chain Monte Carlo (MCMC) technique on a pixel basis (Bennett et al. 2013b). We have compared the synchrotron, free-free and AME maps produced by these methods with the Commander maps through T–T plots with HEALPix $N_{\rm side} = 64$. Table 3 gives the key model parameters of the WMAP models that we used. Point sources from the PCCS2 catalogue brighter than 1 Jy at 28.4 GHz have been masked out. The best-fit ratios of the maps, derived from the T–T plots, are given in Table 4 for the high-latitude sky, with $|b| > 20°$ and for $|b| < 20°$; a is the best-fitting slope. Also listed in Table 4 are the Pearson correlation coefficients (r) for all the comparisons. If $r \gtrsim 0.9$, the measured slope, a, is reliable, since there is a good linear relationship between the Commander and the WMAP templates.

A first obvious difference between the Commander and WMAP MEM/MCMC models is that the AME component is systematically higher (between 2–4 times) in the Commander solution, at the expense of the synchrotron emission that is lower in Commander. This is clearer on the region closer to the Galactic plane (bottom half of Table 4), due to the better correlations measured there.

When comparing the Commander synchrotron solution with the WMAP models that allow the synchrotron spectral index to vary over the sky, the data are not well-fitted with a single slope, since two populations are clearly present. Figure 16 shows the scatter plot between the Commander synchrotron solution evaluated at 22.8 GHz and the WMAP MCMC-f synchrotron model at the same frequency. The two slopes visible in the figure are the result of a flatter spectrum synchrotron component on the plane (e.g., Kogut et al. 2007), which is not accounted by the Commander synchrotron model, where $\beta_{\rm sync}$ is fixed over the sky. This is not the case for the WMAP MCMC-e "sdcnm" and MEM solutions, which use a fixed synchrotron spectral index, resulting in a much better correlation between the Commander and WMAP components (see Pearson correlation coefficients for this component in Table 4). We also note from Table 4 that the Commander synchrotron component is always lower than the WMAP synchrotron models, which is due to the larger AME component in the Commander model.

The Commander free-free component is similar to most of the WMAP models at low Galactic latitudes, where Pearson's $r \gtrsim 0.89$ for all but the MCMC-c model. The correlation coefficients in this case are also close to 1. At high Galactic latitudes (top half of Table 4), the Commander free-free solution is lower than the WMAP models, at the expense of a higher AME contribution in Commander. The wider frequency range of *Planck*, specifically from 100–217 GHz, should enable a cleaner separation of the free-free component (Planck Collaboration Int. XIV 2014; Planck Collaboration Int. XXIII 2015).

In addition to the baseline Commander model, we have also compared the WMAP models to several earlier Commander runs with different input parameters. In particular, we look at a run that used a broken power-law for the synchrotron component along with a single AME component, and another that had straight power-laws for both the synchrotron and free-free components, also with a single AME component. In these models the synchrotron spectral index is fitted locally, while the break, $\Delta\beta$, in the first is fitted globally. This parameterisation is closer to that used by the WMAP team than is our baseline case with two AME components and a GALPROP synchrotron spectrum, and the fitted results are also closer to the WMAP results, with less AME and more synchrotron; however some differences remain. In both models the free-free amplitude in the Commander outputs is still lower than in the WMAP models, and in both Commander still finds less synchrotron emission than WMAP at low latitudes (except for WMAP "sdcnm"). However, at high latitudes they find *more* power in the synchrotron component than does the WMAP analysis. The AME components in these earlier Commander models are weaker than in our baseline and in much closer agreement with WMAP, with ratios around one for both the "fs" and "fss" models at both low and high latitudes, while the Commander solutions find more high-latitude and less low-latitude emission than the "sdcnm" model. These runs were not used for the baseline product as they gave worse overall fits and are less physically motivated than our eventual choice; we note them here solely to qualitatively consider the effects that different models can have on the component outputs.

The WMAP model that is closest to the baseline Commander solution is MCMC-e "sdcnm", although the AME component is brighter in the Commander products. Also, the Commander free-free amplitude is about 30% fainter than the corresponding WMAP fit; this has been noted before from comparison with RRL data by Alves et al. (2010) and Planck Collaboration Int. XXIII (2015). The main limitation in obtaining accurate components maps is the precise quantification of the synchrotron

component. Fuskeland et al. (2014) and Vidal et al. (2015) have shown that the polarized spectral index of synchrotron emission varies across the sky and these variations should be taken into account to obtain an accurate separation between the synchrotron and AME components; low frequency (5–20 GHz) data will be crucial for this.

4.5. LMC and SMC

The Large and Small Magellanic Clouds (LMC and SMC) are satellite galaxies of the Milky Way, close enough (50.0 ± 1.1) kpc for the LMC, Pietrzyński et al. 2013, and (61 ± 3) kpc for the SMC, Hilditch et al. 2005) that they are resolved by *Planck* both at 5′ in thermal dust and 30′ at low frequency. They have already been well studied at *Planck* and WMAP frequencies (Bot et al. 2010; Planck Collaboration XVII 2011; Draine & Hensley 2012). They thus provide a good test-bed for comparing the Commander solution with previous results and expectations, both in the Magellanic clouds and in comparison with our own Galaxy. We show maps of the Commander solution in the LMC in Fig. 17, which we discuss component by component below. The brightest region in all of the non-CMB component maps is the Tarantula nebula, also known as 30 Doradus, a well-known H II and star-formation region located at $(l, b) = (279.^\circ5, -31.^\circ7)$.

To cross-check the Commander solution, we perform aperture photometry on both the Commander maps and the latest *Planck* and WMAP maps, as well as other ancillary data, to generate spectral energy distributions (SEDs) of the LMC and the SMC. For the LMC we use central coordinates of $(l, b) = (279.^\circ5, -33.^\circ5)$, with a circular aperture of radius 300′, and an outer annulus for background subtraction of 300–350′. For the SMC we use central coordinates of $(l, b) = (302.^\circ8, -44.^\circ3)$, with a circular aperture of radius 150′, and an outer annulus of 150–200′. We do not attempt to remove Galactic foregrounds from the maps or SEDs, except through the background annulus in the photometry, since we are using the SEDs for the purpose of comparison. As a result, some Galactic foreground emission can be seen in the resulting LMC thermal dust map in Fig. 17.

We use the same aperture photometry code that was developed for Planck Collaboration XX (2011) and Planck Collaboration Int. XV (2014). We have modified the code to run on the Commander component maps to measure the amplitudes of the individual components in the aperture. The uncertainties are derived from the background annulus only: they do not include model or calibration uncertainties. Results are given in Table 5. We then sum those model SED components to compare with the flux densities measured directly from the Haslam, *Planck*, and WMAP maps, along with radio maps at 1.4 GHz by Reich et al. (2001) and 2.3 GHz by Jonas et al. (1998) and the infrared maps from *COBE*-DIRBE (Hauser et al. 1998) and IRAS (Miville-Deschênes & Lagache 2005). This comparison for the LMC and SMC is shown in the left panel of Fig. 18. We note that the Commander solution does not include data points above 857 GHz in its fit. In deriving the models, we exclude the 100 and 217 GHz *Planck* maps, since those bands contain CO emission.

Using the same spectral component model described in Planck Collaboration Int. XV (2014), including colour corrections, we also perform least-squares fits (LSF) to the flux densities up to 3 THz. There are two variants of the LSF model reported in Table 5 and Fig. 18. One is fitted to data including the CMB contribution (henceforth referred to as "LSF") and the other is fitted to data post-CMB subtraction, namely flux densities from aperture photometry on CMB-subtracted maps (using the Commander CMB solution; henceforth referred to as "LSF-CMB").

Table 5. Values of the fitted parameters for the LMC (top) and the SMC (bottom) from Commander, and the least-squares fitting before and after CMB subtraction.

Parameter	Commander	LSF (CMB)	LSF (no CMB)
EM	66.2 ± 1.7	57 ± 4	67 ± 2
T_e [K]	7000	8000	8000
A_d	24 903 ± 488	$(3.1 \pm 0.6) \times 10^{-5}$	$(2.82 \pm 0.14) \times 10^{-5}$
β_d	1.516 ± 0.003	1.47 ± 0.07	1.42 ± 0.03
T_d [K]	19.29 ± 0.09	22.7 ± 0.9	23.2 ± 0.3
A_{AME1}	15.3 ± 0.3	...	...
A_{AME2}	3.47 ± 0.14	...	...
A_{CMB} [μK]	16 ± 3	15 ± 3	...
A_{sync} [Jy]	239 ± 4	406 ± 33	375 ± 31
β_{sync}	−3.1	−2.70 ± 0.05	−2.74 ± 0.04
EM	20.0 ± 1.8	21.7 ± 0.9	25.1 ± 0.4
T_e [K]	7000	8000	8000
A_d	2541 ± 70	$(1.26 \pm 0.07) \times 10^{-5}$	$(7.2 \pm 0.3) \times 10^{-6}$
β_d	1.463 ± 0.004	1.36 ± 0.05	1.06 ± 0.02
T_d [K]	18.57 ± 0.14	21.5 ± 0.3	25.35 ± 0.18
A_{AME1}	1.497 ± 0.07	...	...
A_{AME2}	0.57 ± 0.03	...	...
A_{CMB} [μK]	36 ± 5	37 ± 2	...
A_{sync} [Jy]	25 ± 2	34 ± 3	31 ± 3
β_{sync}	−3.1	−2.76 ± 0.11	−2.88 ± 0.11

Notes. The Commander parameters are as described in Planck Collaboration X (2016) except for A_{sync}, which has been rescaled to a reference frequency of 1 GHz. We note that the Commander uncertainties only include the standard deviation, and do not include modelling uncertainties. The LSF parameters are the same, except for A_d, which is the optical depth at 250 μm.

We now go through each component in turn for both the LMC and SMC, considering both the morphology and the SEDs.

CMB. The CMB maps for both the LMC and SMC do not appear to be strongly contaminated by foreground emission; there is no clear correlation between the CMB map and the foreground components. The average CMB contribution agrees well in both the Commander and LSF estimates in the LMC and SMC. CMB contributions in both objects are positive, as was seen in Planck Collaboration XVII (2011). We thus conclude that the Commander CMB solution is robust at separating the CMB from foreground emission in this region.

Synchrotron. Low-frequency synchrotron emission is present in both the LMC and SMC. It is subdominant in total intensity at *Planck* and WMAP frequencies. In the LMC the peak of the emission is slightly offset from the Tarantula nebula, and diffuse emission is also present. The Commander spectral index between 408 MHz and WMAP/*Planck* frequencies is assumed to be $\beta_{sync} = -3.1$ according to the GALPROP model (see Sect. 4.3); in the LSF and LSF-CMB fits for the LMC we find $\beta_{sync} \approx -2.7$, and for the SMC $\beta_{sync} \approx -2.8$, effectively between 408 MHz and 22.8 GHz. At similar frequencies, Israel et al. (2010) found that $\beta_{sync} = -2.70 \pm 0.05$ in the LMC; however, they found a steeper index of −3.09 ± 0.10 in the SMC that agrees better with the Commander model. As such, Commander will under-estimate the

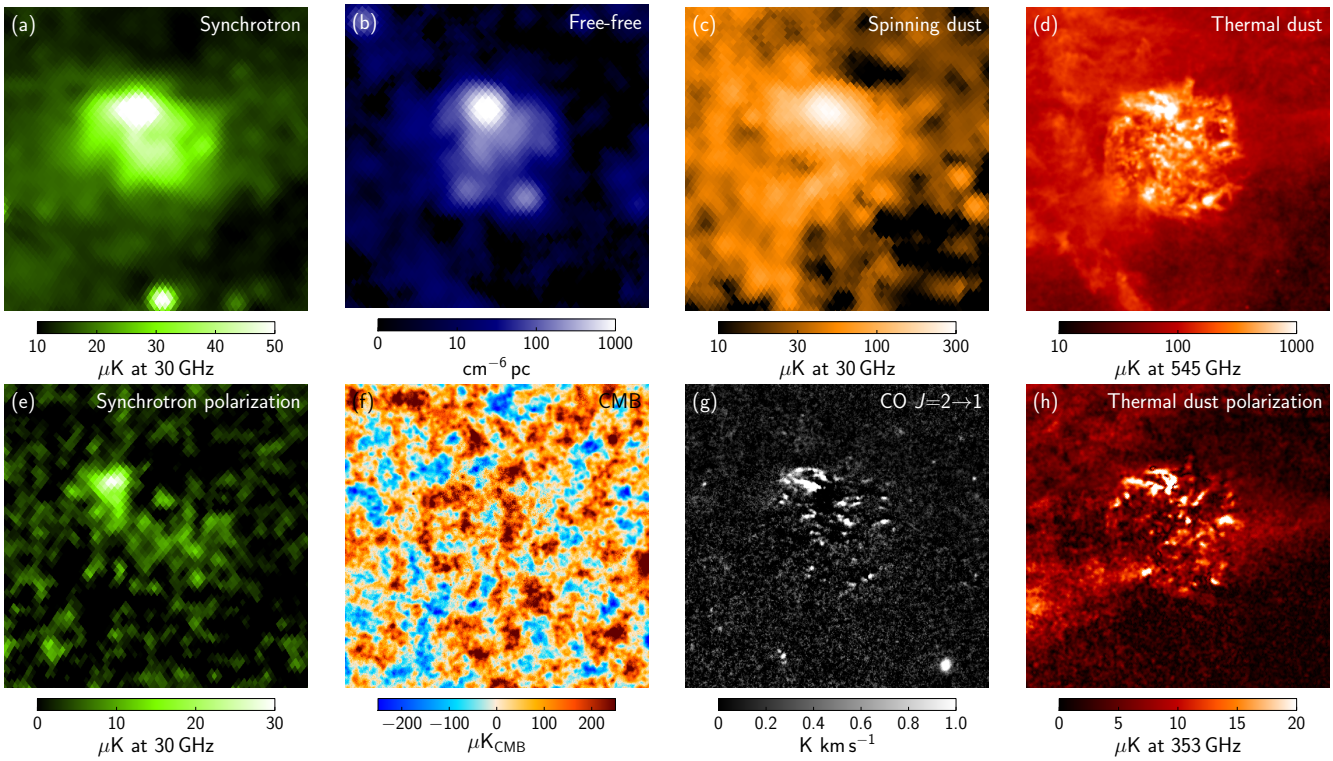

Fig. 17. `Commander` solution in the Large Magellanic Cloud region, plotted in Galactic coordinates. Panels show from *left to right* and *top to bottom*: **a)** synchrotron brightness temperature at 30 GHz with 1° resolution (linear colour scale); **b)** free-free emission measure with 1° resolution (logarithmic colour scale); **c)** spinning dust brightness temperature at 30 GHz with 1° resolution (logarithmic colour scale); **d)** thermal dust brightness temperature at 545 GHz with 5′ resolution (logarithmic colour scale); **e)** synchrotron polarization amplitude, P, at 28.4 GHz with 1° resolution (corrected for polarization leakage, linear colour scale); **f)** CMB temperature with 5′ resolution (linear colour scale); **g)** CO $J = 2 \rightarrow 1$ emission with 5′ resolution (linear colour scale); and **h)** thermal dust polarization amplitude, P, at 353 GHz with 5′ resolution (corrected for polarization leakage, linear colour scale). Each map covers 15° × 15°, and is centred on Galactic coordinates $(l, b) = (279°, -34°)$.

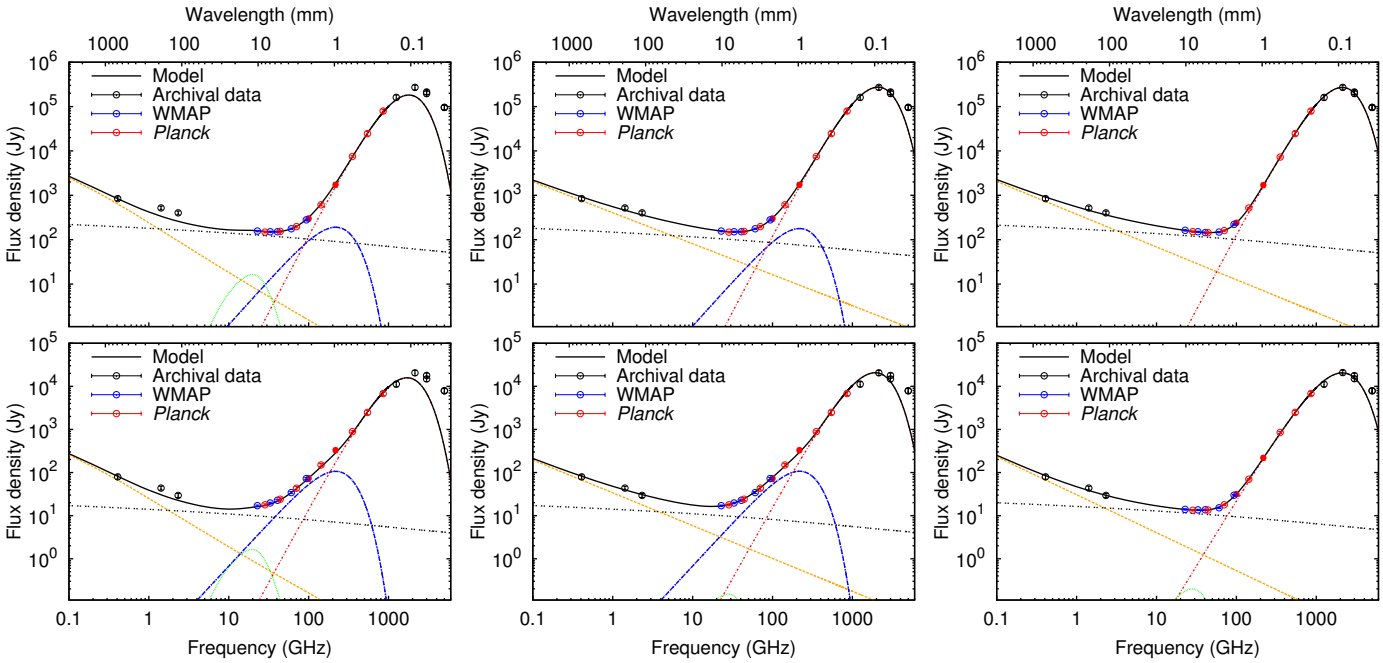

Fig. 18. SEDs of the LMC (*top*) and SMC (*bottom*) using aperture photometry, from the `Commander` solution (*left*), and least-squares fits to the data with (*middle*, LSF) and without (*right*)) the CMB (LSF-CMB). The components are synchrotron (orange dashed lines), free-free (black double-dashed lines), AME (green dashed lines), CMB (blue dashed lines), and thermal dust (red dashed lines). The solid black line represents the sum of the model components. *Planck* data points are shown in red, WMAP in blue, and other ancillary data (some of which are not included in the fits, see text) in black.

synchrotron contribution at *Planck* frequencies, particularly in the LMC and to a lesser extent in the SMC. The synchrotron amplitudes at 1 GHz in Commander for both the LMC and SMC are significantly lower than that in the LSF, due to the steep spectrum assumed, with the difference absorbed by the free-free component. The LMC also appears in the synchrotron polarization map; the polarized emission is at its highest (around 30% polarized, although this would be lower if the Commander synchrotron intensity spectral index were flatter) to the left of the peak in the synchrotron total intensity, offset from Tarantula, which corresponds to the two polarized synchrotron filaments identified by Klein et al. (1993).

Free-free emission. The free-free component dominates the SEDs of both the LMC and the SMC at frequencies of 5–50 GHz. The majority of the emission comes from the Tarantula nebula; there is also diffuse emission closer to the centre of the LMC, and other compact (<1°) objects are present. The morphology agrees well with the Hα maps of individual sources in the LMC by Davies et al. (1976, DEM): the main region of 30 Dor is surrounded by a large number of smaller sources that show up in the Commander map as diffuse emission. The two lower regions are groups of sources, with one comprising DEM 4, 6, and 36 (bottom-left), and the other consisting of DEM 27, 28, and 29 (bottom-right). The amplitude of the free-free emission can be converted to a star-formation rate (SFR) using the equations in Condon (1992). The Commander free-free amplitude at 10 GHz is 141 Jy, which gives an SFR of 0.10 $M_\odot\,\mathrm{yr}^{-1}$; the LSF model gives 0.08 $M_\odot\,\mathrm{yr}^{-1}$, and the LSF-CMB model gives 0.09 $M_\odot\,\mathrm{yr}^{-1}$. These are lower than the estimate of 0.2 $M_\odot\,\mathrm{yr}^{-1}$ for the average SFR from analyses of stellar populations by Harris & Zaritsky (2009) and Rezaeikh et al. (2014), but agree well with the recent star formation rate of 0.06 $M_\odot\,\mathrm{yr}^{-1}$ calculated by Whitney et al. (2008) based on young stellar objects; these authors also give a range of SFR estimates of 0.05–0.25 $M_\odot\,\mathrm{yr}^{-1}$ from infrared and Hα data. However, all of these estimates correspond to an SFR over different timescales (e.g., Murphy et al. 2012), as well as being subject to systematic effects; a more detailed study would be necessary to disentangle these effects. For the SMC, the amplitude at 10 GHz of 11 Jy from the Commander and LSF models gives an SFR of $1.1\times10^{-2}\,M_\odot\,\mathrm{yr}^{-1}$; the LSF-CMB model gives a slightly higher value of $1.3\times10^{-2}\,M_\odot\,\mathrm{yr}^{-1}$ from a flux density of 12.8 Jy. These estimates of the SMC free-free amplitude agree well with those from Draine & Hensley (2012), who attributed 11 Jy to the free-free component at 10 GHz, in very good agreement with the Commander amplitude.

AME. The Commander solution finds a small component of AME in both the LMC and SMC. In the LMC, the AME map has a bright region centred on 30 Dor, where there are many sources seen in the higher-resolution Hα and radio maps (McGee & Newton 1972, Davies et al. 1976), and where the brightest emission is seen in the LMC in thermal dust. The AME towards 30 Dor has a higher peak frequency in the Commander solution than that on either side, following the pattern of H II regions having higher peak frequencies, as noted in Sects. 3 and 4.2. At 20 GHz, the peak of the AME component, AME contributes about 16 Jy to the model, compared with the free-free amplitude of around 130 Jy. In the SMC, 1.6 Jy is attributed to AME, compared with 10 Jy for the free-free component. In both cases, AME is about 10% of the free-free amplitude, and it is comparable to the component separation uncertainty in the free-free component, and the amplitudes of the synchrotron and CMB components at that frequency. The ratio of free-free to AME here is significantly higher than that seen in the Galaxy (Planck Collaboration XX 2011; Planck Collaboration Int. XXIII 2015) due to the presence of 30 Dor, which dominates the free-free emission in the LMC. The LSF analysis includes an AME model, but is consistent with little or no AME (the AME contribution seen in the LSF SMC SED has a significance below 1σ). Nor was AME seen in the LMC and SMC SEDs in Planck Collaboration XVII (2011). Draine & Hensley (2012) included an AME component in their SED fits to the SMC of 3–5 Jy at 40 GHz; the Commander solution returns much lower AME amplitudes in the SMC of 0.2 Jy at 40 GHz. We calculate AME emissivities for the LMC for a 15° × 15° region centred on $(l, b) = (279°, -34°)$, and for the SMC in a 5°×5° region centred on $(l, b) = (302.°8, -44.°3)$. The emissivities are given in Table 2. For the LMC we find that the AME/545 GHz and AME/τ_{353} emissivities are comparable to those from the AME regions; however, the AME/100 μm emissivity is substantially lower, which is likely because the LMC has a higher dust temperature than the Galactic average. For the SMC, we find much lower values for all three emissivities. The LMC has comparable PAH levels to our Galaxy (Bernard et al. 2008), while the SMC has lower levels, which could explain why we find higher AME emissivities in the LMC than the SMC. The SMC has a very small grain (VSG) population that can be seen particularly clearly at 70 μm (Bernard et al. 2008); given the emissivities here this VSG emission is unlikely to be connected to AME, as AME is typically thought to be due to PAHs. We thus conclude that the small amount of AME found by Commander in the LMC is at the level that would be expected from our Galaxy, although both the LMC and SMC regions may be contaminated by leakage from the free-free and synchrotron components, as well as being potentially influenced by the steep synchrotron spectral index assumed in the Commander model. Further work is needed to improve constraints on the AME and its properties in this region.

CO. The Commander CO J=1→0 map detects various regions of CO emission, particularly around the 30 Dor region, as well as in various other dusty regions in the LMC. The morphology of the map compares well with ground-based surveys, such as the Magellanic Mopra Assessment (Wong et al. 2011). This indicates that the separation of CO emission has worked well in this region. An exception is a large negative region in the Commander high-resolution map, which is a component separation artefact.

Thermal dust. The thermal dust seen by *Planck* agrees well in morphology with IRAS data. The dust temperatures from Commander are significantly lower than those from the LSF: for the LMC the average dust temperature in the aperture is (19.29 ± 0.01) K, compared with (22.7 ± 0.9) K for the LSF. Planck Collaboration XX (2011) found (21.0 ± 1.9) K when fitting for a free β_d = 1.48 ± 0.25 (comparable with the β_d found here). Commander only fits data up to 857 GHz and the fitted temperature and spectral index underestimates the flux densities at higher frequencies. The LSF fits data up to 3 THz and so finds a higher temperature. We also note that where the fitted temperature is higher, β_d is lower. The same applies for the SMC, where the average from Commander is (18.57 ± 0.14) K, compared to (21.5 ± 0.3) K from the LSF, and (22.3 ± 2.3) K from Planck Collaboration XX (2011), where β_d = 1.21 ± 0.27 is flatter than found by Commander but in better agreement with the

LSF[9]. In the SMC, the submm excess (see e.g., Israel et al. 2010, Planck Collaboration XVII 2011) has been subsumed into the dust spectral index and the lower dust temperature. The thermal dust polarization in the LMC traces the spiral structure, with the projected magnetic field running parallel to the structure, particularly in the 30 Dor region where the *Planck* data have a higher sensitivity due to its scan strategy. This is also where the synchrotron polarization is seen.

In conclusion, we find that the `Commander` component maps in the regions of the LMC and SMC largely agree well with previous results and expectations, although the thermal dust properties are only representative up to 857 GHz.

5. Polarized foregrounds at $\lambda \approx 1$ cm

The previous section showed that significant uncertainties remain for component separation in total intensity. Fortunately, the picture is quite different in polarization, where, between *Planck* and WMAP, we have twelve bands with maps of the all-sky polarization. Our current understanding is that there are three significantly polarized components: the CMB; synchrotron emission; and thermal dust. AME polarization has not been clearly detected, with upper limits of typically a few per cent (see Sect. 5.7).

The three strongly polarized components have radically different spectra, and moreover, CMB polarization is well separated in angular scale from the foregrounds: after convolution to 1° resolution, the CMB polarization predicted by the *Planck* best-fit cosmology contributes an rms of only 0.54 μK to the Q and U maps, negligible compared to the noise per beam (although, of course, detectable in the angular power spectrum at low multipoles). The spectrum of the polarized dust is discussed in Planck Collaboration Int. XXII (2015) and Planck Collaboration Int. XXX (2016). Here we are interested primarily in the synchrotron component and consider the dust polarization only to the extent that the magnetic field pattern that it traces sheds light on the synchrotron features (Sect. 5.2). Planck Collaboration Int. XIX (2015) informs our understanding of the dust polarization features.

We begin by constructing a new map of polarized synchrotron emission by combining WMAP and *Planck* maps, which significantly increases the average S/N compared with WMAP/*Planck* data alone. We then discuss some of the major features in the polarized sky, including the loops, spurs, filaments, and bubbles.

5.1. Combination of Planck and WMAP

WMAP (Page et al. 2007; Bennett et al. 2013a) provided the first clear view of the intrinsic synchrotron polarization across the sky – previous ground-based observations (e.g., Brouw & Spoelstra 1976; Wolleben et al. 2006) being strongly affected by Faraday rotation and depolarization due to their lower observing frequencies ($\lesssim$2 GHz). WMAP's lowest-frequency channel, K-band, dominates the combined WMAP S/N in polarization because of the steep spectrum of synchrotron emission. Although the full-mission *Planck*-LFI maps have significantly lower noise than the final WMAP results, the foreground S/N is very similar, since at *Planck*'s lowest frequency (28.4 GHz) the synchrotron brightness is half that in K-band. After smoothing to a common resolution of 1°, the median (mean) S/N is 2.47 (3.77) for WMAP K-band and 2.64 (3.72) for *Planck* 28.4 GHz. The different scan strategies of the two missions result in somewhat different sensitivity patterns, so that each map is superior in some sky regions; *Planck* has the largest advantage in the regions around the Ecliptic poles (see the hit count maps in Planck Collaboration VI 2016).

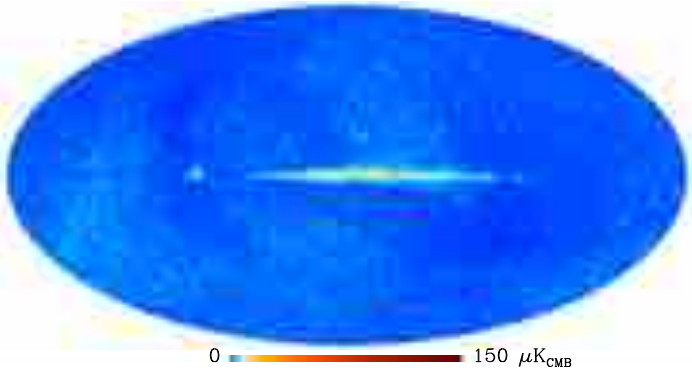

Fig. 19. Difference between the combined weighted polarization maps for *Planck* and WMAP at 1° resolution, defined as $\left[(Q_{\rm Planck} - Q_{\rm WMAP})^2 + (U_{\rm Planck} - U_{\rm WMAP})^2\right]^{1/2}$.

Planck and WMAP polarization results generally agree well, but the difference map (see Fig. 19) shows significant artefacts, both on the plane and at high latitudes. Extremely large angular-scale ($\ell = 3, 5, 7$) residuals covering much of the sky are thought to be due to the poorly-constrained modes in the WMAP data as a result of the scan strategy (Jarosik et al. 2011; Bennett et al. 2013a); they occur in all the WMAP frequency maps, with an approximately consistent pattern. However, they are most readily visible in the V- and W-bands of WMAP when the foreground brightness is close to the minimum. The on-plane features are likely to be caused by inaccuracies in the *Planck* leakage maps. These differences are further discussed in Planck Collaboration X (2016).

Because polarization is only marginally detected in many pixels of the individual WMAP and *Planck* maps, we have constructed a weighted mean image using all the maps in the range 20–50 GHz, where the polarization is dominated by optically thin synchrotron radiation, with negligible Faraday rotation (except at the Galactic centre, Vidal et al. 2015), so that the polarization angles should be consistent between the maps. We first smooth the *Planck* and WMAP maps to a resolution of 1° and $N_{\rm side} = 256$ in both Q and U, and the QQ, UU, and QU covariances as well. We assume that the emission has a single spectral index of −3.0, and we use this to scale all the maps (and their covariances) to match the *Planck* 28.4 GHz image. We then use the 2×2 Q and U covariance matrices and their inverse matrix to calculate the weighted average in each pixel of the Q and U maps. We create three weighted maps as a result: one consisting of the three lowest WMAP bands; one consisting of the two lowest *Planck* bands; and one using both WMAP and *Planck*. The *Planck* variance estimates include the uncertainty in the bandpass leakage correction. This results in a large fractional error in Q and U along the plane, so WMAP data dominate the on-plane emission in the combined map. At high latitudes,

[9] The `Commander` solution has a Gaussian prior on the thermal dust spectral index of $\beta = 1.55 \pm 0.1$, and the fitted values for the LMC and SMC are towards the lower end of this prior; however `Commander` would have returned a lower value for β than the prior if the data had preferred it. The LSF indicate flatter spectral indices, however this is including data over a larger (>857 GHz) range of frequencies.

the somewhat higher sensitivity of *Planck* down-weights the impact of the large-scale WMAP polarization artefacts, but we note in our discussion when these may still have an impact on our results. The improvement in S/N is significant, with: a median (mean) S/N of the WMAP weighted map of 2.70 (4.19); the *Planck* weighted map of 2.68 (3.81); and the combination of both of 3.37 (5.39), where the bigger improvement comes from the combination of both WMAP and *Planck*. This corresponds to a roughly 25% improvement in S/N compared to using the combined WMAP or *Planck* maps separately.

`Commander` also provides a polarized intensity synchrotron map, which is calculated using only *Planck* data. As this map is the best-fit solution to a model using noisy data, it is noisier than our combined *Planck*-only map (our map treats the small CMB component as noise). Moreover, the addition of WMAP K-band data in our map further reduces the noise in the final combined map. At 1° resolution, the `Commander` map has a median noise value over the entire sky of $\sigma_Q \approx \sigma_U = 4.5\,\mu$K, while our combined map has $\sigma_Q \approx \sigma_U = 2.6\,\mu$K.

Polarized intensity maps have been debiased using the asymptotic estimator (Montier et al. 2015; Vidal et al. 2016), which generalizes the estimator first proposed by Wardle & Kronberg (1974) to the case of anisotropic errors in (Q, U). Figure 20 shows the resulting polarization combination maps. A number of new polarized structures visible in the combined map that were unclear in the individual maps are highlighted. These are discussed in the sections that follow.

5.2. Overview of polarized synchrotron emission

Synchrotron total intensity is distributed comparatively uniformly over the sky. In the 408 MHz map, assuming an instrumental plus extragalactic background of 8.9 K (Wehus et al. 2016), half the total Galactic flux is contributed by 18% of the sky[10]. The equivalent figure for the dust-dominated *Planck* 545-GHz map is 4.6%. In the synchrotron intensity map, although the Galactic plane and the North Polar spur are visually prominent, they are superposed on broad diffuse emission that dominates the total flux.

This diffuse emission seems to be much weaker in polarization. Away from the narrow Galactic plane, i.e., at $|b| \gtrsim 3°$, the polarized cm-wavelength emission is dominated by the synchrotron loops and spurs familiar from low-frequency radio surveys. In fact, Vidal et al. (2015) demonstrate a close correspondence between the polarized intensity at WMAP K-band and an unsharp-masked version of the 408 MHz map, in which structure on scales $\gtrsim$10° is filtered out (see Fig. 21 top row a and b).

In particular, there is hardly any trace in the *Planck* and WMAP polarized maps of the synchrotron halo of the inner Galaxy, which fills roughly $|l| \lesssim 60°$ and $5° \lesssim |b| \lesssim 15°$ (Planck Collaboration Int. XXIII 2015) and contributes 20–30% of the Galactic synchrotron flux in low-frequency maps (compare panels a and c in Fig. 21). The effect is even clearer in fractional polarization, which is very low ($\lesssim$10%) in the inner halo region (see Fig. 22). The component separation analysis of Sect. 4 implies that the halo is still present in the unpolarized cm-wavelength maps, because the data are well-fitted with our synchrotron model, which has a constant shape, so that the synchrotron distribution is no different at 20 or 30 GHz from 408 MHz. Although, as we have seen, this separation is subject to substantial uncertainties, it is corroborated by spectral analysis of ground-based surveys (Reich & Reich 1988; Platania et al. 2003) that find that the halo and spurs have similar spectral indices near 1 GHz.

The magnetic field in the Galactic disc follows the plane, as expected from the shearing effect of differential rotation, and one would expect the same to apply in the inner halo. Its polarization would then be roughly orthogonal to that in the spurs rising out of the plane, which all have fields roughly parallel to their axes (Vidal et al. 2015). Therefore, the net polarization of halo and spurs will cancel to some extent. But the fact that the spurs are prominent in polarization, even when they are only perturbations on the inner halo in total intensity (see Fig 23), implies that the halo must be very weakly polarized; even between the spurs, there is hardly any sign of a field parallel to the plane in the inner halo region (a trace may be visible near $(l, b) = (34°, 8°)$; see the discussion of the $l = 45°$ feature in Sect. 5.4). This is a surprising contrast to the narrow plane at $|b| \lesssim 3°$, where the overall parallel orientation of the field is very clear in Fig. 20, despite the fact that a significant fraction of its emission is due to individual SNRs (Planck Collaboration Int. XXIII 2015), whose overall polarization orientation is nearly random. The conventional analogy between the Galactic halo and the Solar corona suggests that the halo field should relax to a nearly force-free configuration with little small-scale structure, constrained primarily by the foot points where the field lines are tied to dense gas clouds in the plane. This would lead us to expect a reasonably high fractional polarization; differential rotation of the footpoints should, as with the disc field, shear the field so that it is largely parallel to the plane as viewed from Earth. Evidently the halo field is much more tangled than this naive argument would suggest.

It is worth noting that the overall fractional polarization also appears to be low (<15%) across the high latitude sky (Fig. 22), although this quantity is very sensitive to the poorly-known zero level of the synchrotron total intensity (Vidal et al. 2015). Again, the implication is that there is substantial tangling of the field even on lines of sight looking out of the disc.

5.3. Loop I

5.3.1. Structure

Loop I is the nearly-circular structure of radius 58° whose top-left quadrant (as viewed in Galactic coordinates)[11] is traced by the North Polar spur (NPS). It is also detected in soft X-rays, where the emission is dominated by thermal emission from 3×10^6 K gas (Willingale et al. 2003), and is bordered by cold material visible via H I and dust emission (both thermal and anomalous). The NPS has long been a suspected γ-ray emitter, and Ackermann et al. (2014) clearly detect Loop I at GeV energies, presumably due to inverse-Compton scattering of starlight by the CRLs in the loop, combined with pion decay emission from the cold border. Figure 21 shows the structure in several tracers in stereographic projection (chosen because circles are projected as circles and also because the angular scale increases outwards, enabling a clear display of features around the edge of this enormous structure that covers most of a hemisphere).

In both Galactic hemispheres the polarization maps show a number of spurs within Loop I that parallel its outer boundary,

[10] The diffuse emission may be even brighter, since the background assumed may include an isotropic component of Galactic emission. Using the Lawson et al. (1987) extragalactic background estimate of 5.9 K, half the sky flux comes from 21% of the sky.

[11] To avoid the non-intuitive concepts of Galactic "East" and "West", throughout this section we describe emission features in terms of left and right as projected in the figures, corresponding to the directions of increasing and decreasing longitude, respectively.

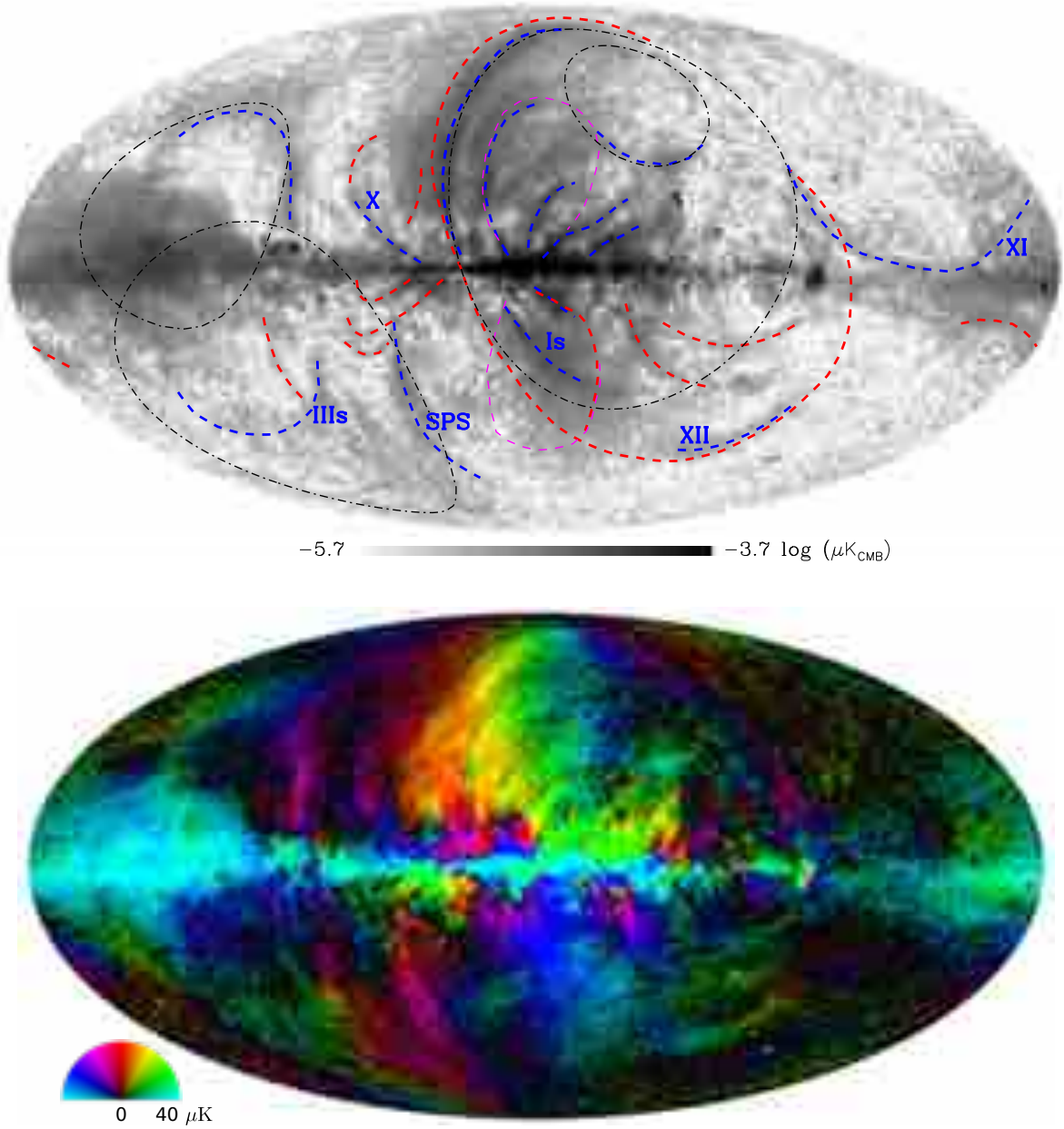

Fig. 20. *Top*: combined weighted polarization intensity map after debiasing, with features highlighted. The black dash-dot lines show the outlines of Loops I to IV, as defined by Berkhuijsen et al. (1971), the blue dashed lines show the filaments described by Vidal et al. (2015) using WMAP polarization data, the red dashed lines show features that are visible in the new *Planck* data, and the magenta dashed lines show the outline of the *Fermi* bubbles. Filaments that are discussed in the text are labelled. *Bottom*: the same combined polarization intensity map, with projected magnetic field angle (at 90° to the polarization angle) encoded in colour with asinh scaling. The coloured half-disc represents the polarization angle depicted in the map, with 0° horizontal, while the polarization intensity is represented with the radial distance along the half-disc.

nearly all concentrated on the left-hand side of the structure. Since Loop I covers about a third of the sky, including the inner Galaxy, some of the features projected inside it are surely unrelated, but the general coherence of the structure strongly suggests that most of the emission away from the plane has a common cause. The internal spurs are much more obvious in polarization than in total intensity, even after unsharp masking (Figs. 21a–c, 23). These features are therefore highly polarized; however, they are projected onto diffuse extended emission that seems to be weakly polarized ($\lesssim$15%), including the inner halo of the Galaxy, so the overall fractional polarization towards the inner spurs is not much higher than towards the NPS itself ($\approx$40–50%), while between them the fractional polarization is low (Fig. 22).

Previous measurements of the radio outline found Loop I to be surprisingly close to circular: the definitive study by Berkhuijsen et al. (1971, hereafter BHS) found that 19 points on the ridge-line covering 155° around the loop (all in the north Galactic hemisphere) fitted a small circle with an rms of only 0°.9. The NPS conforms roughly to the brightness profile expected from a shell of emission, for which the ridge-line marks the tangent to the inner surface; the outer boundary lies several degrees beyond the ridge line, and is also clearly traceable, especially around the NPS (e.g., Fig. 21b). Relatively bright diffuse polarized emission outside the boundary of the NPS south of $b = 40°$ (Fig. 21c, 25) seems to be part of a different structure (see Sect. 5.4).

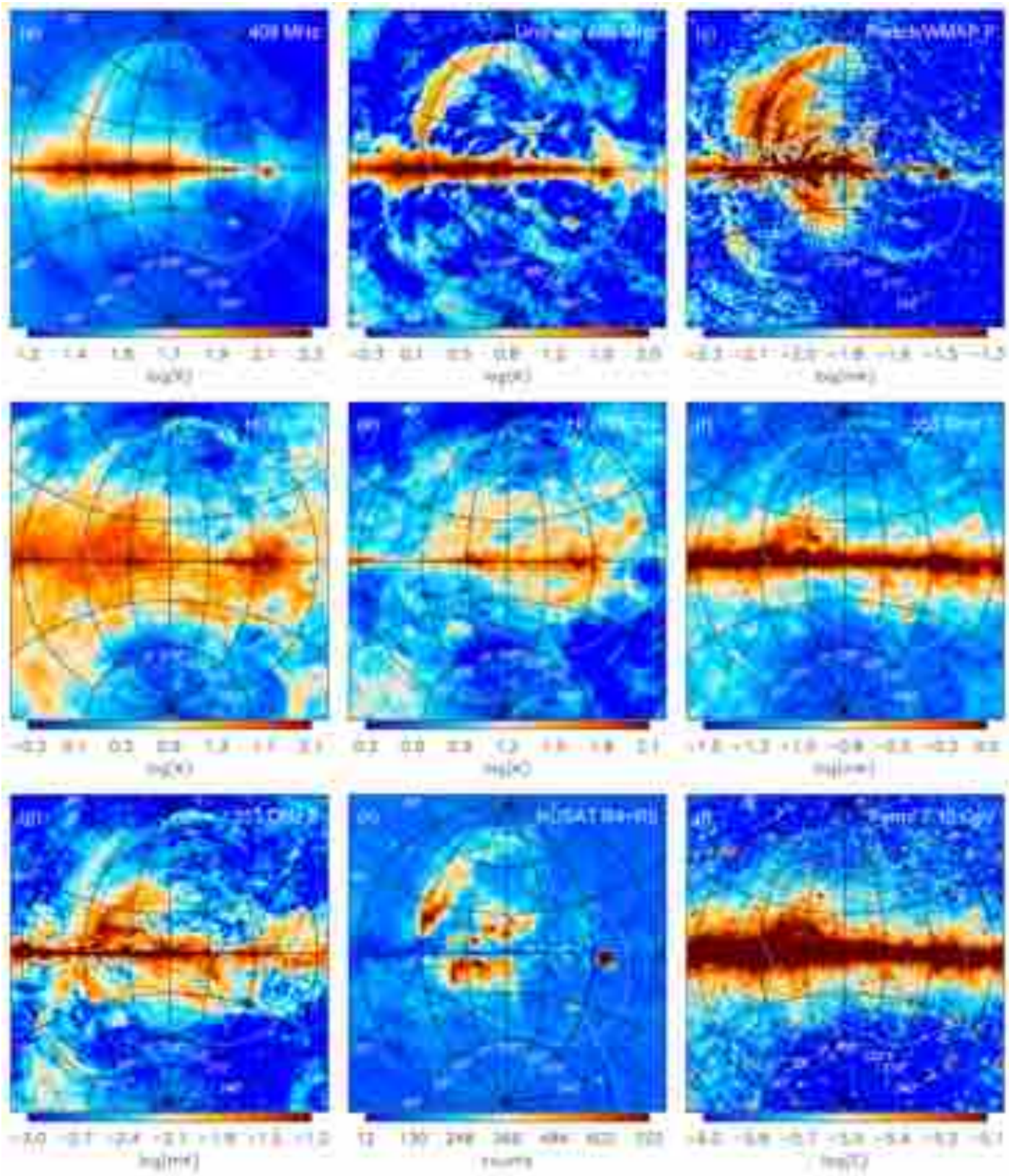

Fig. 21. Various tracers of the interstellar medium in the hemisphere containing Loop I, with all maps centred at $l = 330°$, $b = 0°$, and using stereographic projection, so that small circles in the sky are projected as circles: **a)** 408 MHz; **b)** unsharp-mask 408 MHz; **c)** combined *Planck*-WMAP polarization intensity; **d)** H I at $v_{\rm LSR} = 0$, velocity width 10 km s^{-1}, from the LAB survey (Kalberla et al. 2005); **e)** the same, at −10 km s^{-1}; **f)** *Planck* 353 GHz temperature; **g)** *Planck* 353 GHz polarization intensity; **h)** ROSAT bands R4+R5 (0.44–1.21 keV) from Snowden et al. (1997); and **i)** *Fermi* 1–10 GeV from Ackermann et al. (2014). The dashed white outline is our proposed outer boundary, derived from panels **b)** and **c)**.

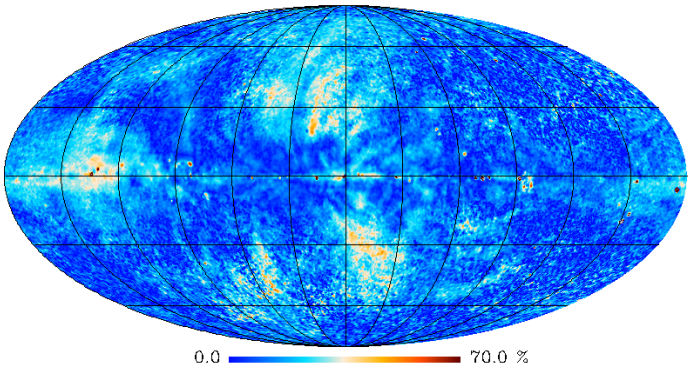

Fig. 22. Polarization percentage of the debiased weighted polarization intensity map against the Commander synchrotron total intensity fit evaluated at 22.8 GHz. Uncertainties in the component separation discussed in the text, and also uncertainty in the absolute zero level, make this highly uncertain, except in regions of strong synchrotron emission, such as the North Polar spur and the inner Galactic halo (see also discussion in Vidal et al. 2015).

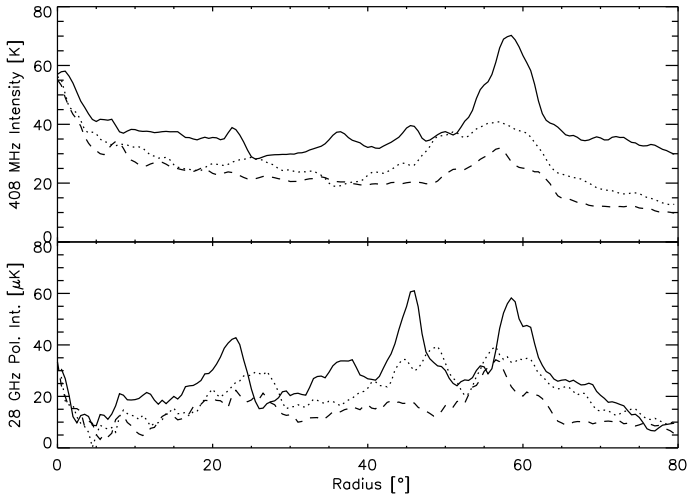

Fig. 23. Profiles of Loop I in total intensity at 408 MHz (Remazeilles et al. 2015) and in our combined *Planck*-WMAP polarized intensity image at 28.4 GHz. Profiles are along radial cuts beginning at the nominal centre of the loop, $(l, b) = (329°, 17\overset{\circ}{.}5)$ and are averaged over a 10°-wide sector in position angle, at position angles 75° (solid line), 50° (dotted), and 25° (dashed). They cross the North Polar spur at $b = 22°$, 43°, and 61°, respectively.

South of the plane, the loop is superimposed on the inner halo and cannot be clearly followed in total intensity, but in WMAP and *Planck* polarization maps (Figs. 20, 21), the pattern is clear, at least on the left-hand side of the structure. The brightest southern spur, called filament Is by Vidal et al. (2015), runs well inside the path of the BHS small circle. However, a fainter spur extends from $(l, b) = (22°, -5°)$, closely along the BHS circle until its ridge becomes lost in faint diffuse emission near $b = -37°$; at this point clearly-detectable polarization again extends several degrees outside the circle. There is then no trace of a ridge-line close to the BHS circle along its whole bottom-right quadrant. It eventually re-aligns with the observed loop boundary at the top of the spur north of the Vela SNR $(l, b) = (268°, 25°)$, near the first measured point in Berkhuijsen et al. (1971). In this bottom-right quadrant three broad, faint, concentric arcs extend from the interior of Loop I, reaching some 30° beyond the BHS circle; these arcs are visible both in polarization and in the unsharp-masked 408 MHz map. The outermost (filament XII of Vidal et al. 2015) rejoins the plane near $l = 250°$ and appears to emerge on the other side as the aforementioned spur above Vela. Although they might be unrelated, they share the general pattern of the other Loop I filaments, for instance the middle arc that passes in front of the LMC is clearly brightest on the left-hand side, as it approaches the Galactic plane near $l = 300°$. We consider it plausible that filament XII represents the outer boundary of Loop I, and on this basis we have marked the outline of the loop in Fig. 21. None of the current theories (see Sect. 5.3.3) predict a strictly spherical structure; taking the smallest plausible distance to the centre as 120 pc, the diameter is at least twice the 100 pc scale height of the H I distribution. Therefore, even ignoring the possible interaction with the Local Cavity (LC) in which the Sun is situated, the loop is expanding into an inhomogeneous environment. Most individual SNRs, even though much smaller than Loop I, show quite large departures from circular outlines, often exceeding the level of distortion implied if filament XII traces the edge of Loop I.

In X-rays, the North Polar Spur peaks at a position inwards from the synchrotron ridge, but, as the outline drawn in Fig. 21 shows, the outer edge of the spur in the two tracers is coincident. This result is unexpected, because the Spur cannot be bounded by a shock front fast enough ($v \gtrsim 300\,\mathrm{km\,s^{-1}}$) to heat the ambient medium to millions of kelvin, while at the same time accelerating the cold border to at most $25\,\mathrm{km\,s^{-1}}$ (see Sect. 5.3.3 below). In young supernova remnants, co-incidence of radio and X-ray boundaries is always due to X-ray synchrotron emission from the shock, and it seems likely that in the NPS the faint X-ray emission from the outer edge is also non-thermal.

In contrast, the gas and dust tracers extend a few degrees further out, particularly obvious in the H I and dust filament at the top of the loop, $(l, b) = (320°, 84°)$. This is just as expected, since neutral atoms and dust grains could not survive at the 3×10^6 K of the X-ray emitting gas.

5.3.2. Distance

Loop I is usually associated with the Sco-Cen OB association (e.g., Salter 1983) at a distance $D = 120$–140 pc (de Zeeuw et al. 1999). The primary evidence is that the NPS appears to be detectable in starlight polarization for stars at distances of $\gtrsim$100 pc (Mathewson & Ford 1970; Santos et al. 2011); the aligned grains must be in the cold border rather than the spur itself. *Planck*-HFI maps of polarized dust (Fig. 21g and Planck Collaboration Int. XIX 2015) show that emission and extinction measurements of field direction agree, confirming that the extinction distances apply to the dust features seen in emission.

Sofue (1977, 1994) has instead suggested that the loop is due to an outburst at the Galactic centre, but in Sect. 5.5 we argue that this model is now ruled out. However, evidence against the traditional distance has also been accumulating.

Iwan (1980) showed that the wall of dense gas that bounds the LC would have to form a major "dent" in the apparently spherical structure of Loop I, assuming $D = 130$ pc. Placing the loop several hundred parsecs away avoids the awkwardness that this dent is not reflected at all in the projected outline. If the shape is quasi-spherical, its near surface would only be about 20% of the distance to the centre, so $D \approx 400$ pc given absorption at the LC wall. It would still be plausible that stars at about 100 pc could be polarized by dust in the border.

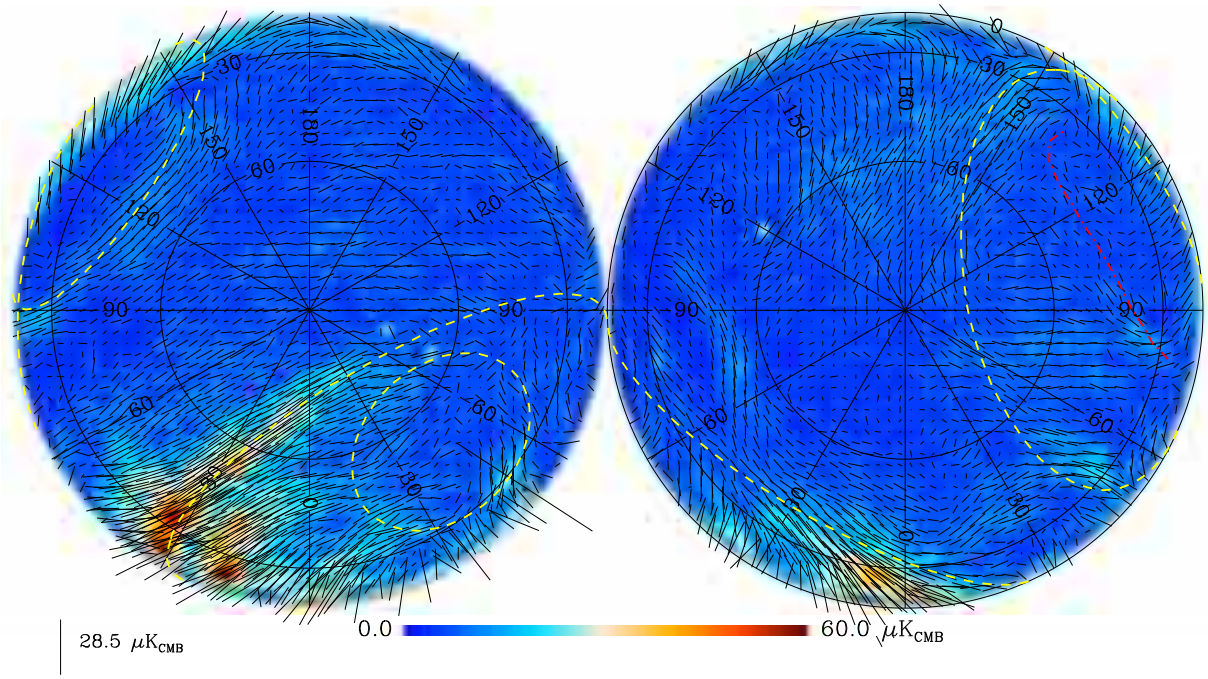

Fig. 24. Line elements showing the orientation of the projected magnetic field (90° to the synchrotron polarization angle) from the *Planck* 28.4 GHz data at 2° resolution. The region within $b = \pm 10°$ has been masked out (grey rings) to avoid crowding of the vectors. The colour scale shows the polarized intensity. The maps are in orthographic projection, centred on the Galactic poles, north (*left*) and south (*right*). Light dashed circles show the outlines of Loops I to IV, as defined by Berkhuijsen et al. (1971) and shown in Fig. 20; the red dashed line is the locus of filament IIIs from Vidal et al. (2015).

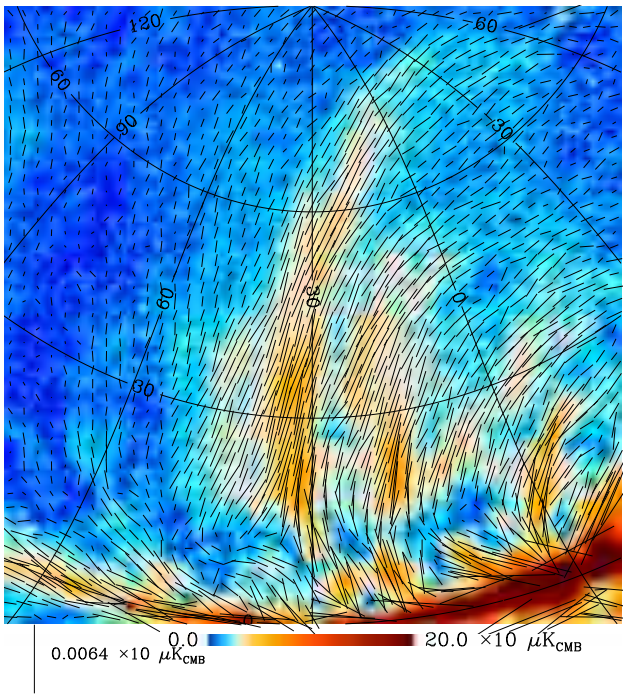

Fig. 25. Combined 28.4 GHz polarization map at 1° resolution of the North Polar spur and the region outside its perimeter, including filament X of Vidal et al. (2015), which leaves the Galactic plane at a shallow angle from near $l = 36°$, and the $l = 45°$ feature between filament X and the NPS. Colour scale is asinh, but the length scale for polarization line elements remains linear, as in all our figures.

The interstellar medium within 200–300 pc has now been tomographically mapped in a variety of absorption tracers against stars with HIPPARCOS distances (Frisch et al. 2011). Towards the bright left side of Loop I, the LC wall is at D = 70–80 pc, and in the Galactic plane dense gas then extends continuously to the Ophiuchus and Lupus molecular clouds at D = 140–160 pc (e.g., Vergely et al. 2010). These are the remnants of the parent cloud(s) of the Sco-Cen association. Although there is a small cavity surrounding the most active part of the association (Puspitarini & Lallement 2012), there is no sign of a cavity with the angular size of Loop I, and this can no longer be ignored given that microwave polarization maps show that the loop crosses the Galactic plane without interruption. Lallement et al. (2014) push the analysis out to 1 kpc by using stars with photometric distances instead of relying purely on HIPPARCOS. They find a low-density cavity starting some 250 pc from the Sun, covering the longitude range of Loop I. If this is the Loop, the radius is roughly a kiloparsec, and it would stretch well into the halo.

Given the lack of room for Loop I immediately outside the Local Cavity, Frisch has long argued (e.g., Frisch 1981; Frisch et al. 2011) that the two are continuous, and that the NPS is merely separated from us by a fold in the LC wall. However, this view is at odds with the evidence from soft X-ray absorption of the NPS. This absorption is visible in the ROSAT map (Fig. 21h) where the inner boundary of the X-ray NPS at $b < 40°$ closely follows the border of the cold material traced in panels d–g of Fig. 21. This material can be confidently assigned to the LC wall, since it is picked up by starlight polarization at $D > 100$ pc (Santos et al. 2011), and again extinction and emission polarization is consistent. X-ray spectra in the region are well fitted by absorbed thermal emission (Puspitarini et al. 2014). Similarly, Sofue (2015) makes a strong case that the sharp truncation of the X-ray NPS below $b = 10°$ is due to absorption in the cold clouds of the Aquila Rift. Both papers find that the hydrogen

column density derived from the X-ray spectra requires a distance to the front of the spur, roughly the shell tangent-point, of at least 200 pc[12]. The corresponding distance to the centre is $D > 400$ pc.

Further evidence for a larger distance comes from the 21-cm polarization map of Wolleben et al. (2006). As noted by Wolleben (2007), the emission from Loop I is strongly depolarized at $|b| \leq 30°$. Given the cut-off in latitude, which does not correspond to any feature in the intrinsic intensity or polarization structure, the depolarization is almost certainly caused by fluctuations in the foreground Faraday depth, ϕ_F, across the 30-arcmin beam of the Wolleben map. The sharp cutoff in b suggests that the high-latitude part of the loop projects above the dense layer of the ISM that creates the "Faraday horizon". At the near distance, the implied scale height, $h \approx 50$ pc, is much too low for the most effective source of widespread Faraday rotation, the warm ionized medium (WIM) ($h = 1$–2 kpc, Gaensler et al. 2008).

The Faraday depths required also imply a larger distance. Depolarization requires fluctuations with $\sigma_F \gtrsim \pi/2\lambda^2 = 36\,\mathrm{rad\,m^{-2}}$. The LC has negligible Faraday depth, due to its low density, and so the magneto-ionic medium responsible must be in the LC wall, if Loop I is directly adjacent to us, even though the wall is mainly traced by neutral gas. Fluctuations across a beamwidth θ requires field tangling on scales $D\theta$, and hence the Faraday depth along the line of sight of length L centred at distance D integrates as a random walk, with amplitude $\sigma_{RM} = k_F \langle n_e |B_{\|}| \rangle \sqrt{LD\theta}$, where $k_F = 8.1 \times 10^{-6}\,\mathrm{m\,nT^{-1}\,pc^{-1}}$. The WIM has electron density $n_e \approx 1\,\mathrm{cm^{-3}}$ at pressure equilibrium. We also assume $B = 1$ nT, with $\langle B_{\|} \rangle$ a factor $1/\sqrt{3}$ smaller. Inserting these values and taking $D = 80$ pc, the required path length is $L \gtrsim 70$ pc, which places the front face of the loop beyond the Sco-Cen association, even if the WIM has unity filling factor. Of course higher-density material would require less path and in fact the Sh 2-27 H II region (G006+236), ionized by ζ Oph at $D = 112$ pc (van Leeuwen 2007), casts a particularly deep Faraday depolarization "shadow" at 21 cm, implying it is in the foreground despite a precise distance that puts it near the assumed shell centre. However, such objects are readily detected in Hα surveys, and cover only a small fraction of the depolarized region. The near distance can only be made compatible with these results if the polarization is dominated by the far hemisphere of the loop, as in one of the models discussed in Sect. 5.3.3.

Given all this evidence that Loop I is several times further away than the Sco-Cen OB association, we searched for an alternative group of OB stars[13] to generate the Loop. Given the angle at which the NPS passes through the Galactic plane, these must be at positive latitudes; we searched $-45° < l < 15°$, $5° < b < 35°$. Apart from Sco-Cen, in this region there are no known OB associations (de Zeeuw et al. 1999), but an association old enough to generate Loop I could already have lost its O stars and could easily have escaped notice. Using SIMBAD (Wenger et al. 2000) we found 51 OB stars (mostly B giants) with parallax, π, between 1 and 3.3 mas; 14 with $0 < \pi < 1$ mas; and 14 with $\pi < 0$. Although the individual parallaxes are barely significant, the distribution is strongly biassed to positive values, so there certainly has been star formation within the last 20 Myr in the relevant volume. We will have to await *Gaia* data for a definitive assessment of stellar groupings there.

5.3.3. Interpretation

The majority view of Loop I is that it is a nearby pre-existing cavity re-energized by one or more recent supernova, in order to explain the cold neutral border seen in dust and H I (see Salter 1983 for a review).

The H I border appears at $V_{LSR} = 0\,\mathrm{km\,s^{-1}}$ (Fig. 21d), which is uninformative, because expansion at the tangent points is perpendicular to the line of sight. Heiles (1984) interpreted the border as part of a shell expanding at $\approx 25\,\mathrm{km\,s^{-1}}$; this implies that the obvious Sco-Cen supershell, visible most clearly at $-10\,\mathrm{km\,s^{-1}}$ (e.g., Kalberla et al. 2005; Vidal et al. 2015, Fig. 21e), is merely the end-cap of Loop I itself. It is worth noting that this shell is elongated in the same direction as our proposed outline for Loop I. However, the Sco-Cen shell is more usually seen as a distinct structure with a smaller angular size than Loop I (e.g., de Geus 1992). If Loop I has a much lower expansion speed, e.g., $2\,\mathrm{km\,s^{-1}}$ as estimated by Weaver (1979), its H I emission would not be separable in velocity from the very local H I surrounding the Sun. The difference between these two interpretations is dynamically significant: at $25\,\mathrm{km\,s^{-1}}$, the cold shell cannot have been accelerated by a shock, since the heating would have dissociated the gas and evaporated the dust; therefore acceleration by a pressure gradient as in the stellar wind model proposed by Weaver (1979) is required. A $2\,\mathrm{km\,s^{-1}}$ expansion is consistent with the weak remains of a shock, although of course a much faster shock would be needed to heat the interior gas above 10^6 K. We also note the absence of optical emission lines characteristic of a cooling shock, which would be expected if the shock speed exceeded $10\,\mathrm{km\,s^{-1}}$. A plausible explanation is that the re-energizing blast wave has only recently hit the cavity wall, which would also explain why the NPS is so much brighter and more sharply-defined than the other large loops (e.g., Borken & Iwan 1977).

Figure 24 shows the projected magnetic field orientation around the Galactic polar caps. We show the *Planck* data only, smoothed to 2° resolution, because of the suspect large-scale structure in the WMAP data. Figure 25 shows the pattern closer to the Galactic plane. The quasi-parallel field pattern in the spurs has been recently discussed by Vidal et al. (2015). Here we wish to draw attention to the regions of organized field orientation at high latitude, *outside* the NPS, which parallels it quite closely over most of its length. Some of this region is occupied by the cold border, where the magnetic field may be organized by the expansion of the loop, e.g., as modelled by Vidal et al. (2015). However, Fig. 24 shows that the parallel-field region extends past longitudes of 60°, well beyond the outer limit of the cold border.

The origin of this high-latitude, inter-loop polarization is unclear. Wolleben (2007) sees it as emission from a "new loop", in whose shell the solar system is embedded, but the evidence for this loop is weak (Sect. 5.4) and its proposed interpenetration of Loop I is, to say the least, dynamically problematic. In a somewhat similar picture, Vidal et al. (2015), following Heiles (1998), place the Solar System on the surface of Loop I, so that loop emission fills a hemisphere: this can explain the high-latitude polarization, but it is not clear why the cold border seems to have a significantly smaller radius than 90°. If the loop is nearby and the polarization is from the halo, the alignment with Loop I would be an accident. However, especially if the loop is as large as suggested in Sect. 5.3.2, the emission may be from

[12] Sofue (2015) argues for a distance of $\gtrsim$500 pc, but this relies on the assumption that the Aquila Rift is at a single distance, whereas clouds at several different distances are involved, see the tomographic maps of Lallement et al. (2014).

[13] We follow Reed (2003) in defining OB stars as main sequence stars of type B2 and earlier, and giants of type B9 or earlier, roughly corresponding to stars massive enough to go supernova.

the immediate environment of the loop, suggesting that Loop I is brightest where the interstellar field is in the plane of the shell surface. This is exactly as predicted by Spoelstra (1972), who applied the model of van der Laan (1962) to the NPS. This appeals to the asymmetry of magnetic stress, which has a net tension along the field lines, so magnetic forces oppose expansion only perpendicular to the field. The same model has been invoked to explain the occurrence of barrel-shaped SNRs aligned with the Galactic plane (Gaensler 1998).

Much of the random component of the Galactic magnetic field is on scales smaller than Loop I (e.g., Haverkorn et al. 2008; Brown & Taylor 2001), so the external field around it is likely to show significant variation in magnitude and direction. Such large objects are therefore unlikely to show the bilateral symmetry of classic barrel-shaped remnants. Nevertheless the basic physics still operates; thus, segments of the shell expanding perpendicular to the field, along the edge of the NPS, will be more strongly impeded and so require higher internal pressure, and therefore stronger nonthermal and thermal (X-ray) emissivity. By the same token, we expect the fainter parts of the shell to expand fastest, consistent with our interpretation of the bottom-right arcs as a bulge in the loop boundary. Of course, asymmetric densities in the ISM will also play a role, and as noted above, if the loop is at $D \approx 140$ pc the observed density gradient is in the required sense.

In old supernova remnants the projected magnetic field is commonly aligned with the outer surface, i.e., the shock propagating through the ISM. This alignment is naturally produced by shock compression, which ensures that the field lines behind the shock tend to be parallel to the shock plane. In this picture there is no global field order in the shock plane, but the field anisotropy causes polarization at viewing angles other than face-on, reaching a maximum when the line-of-sight is in the shock plane (see Laing 1980). Applied to Loop I, this model implies that both the NPS and the internal spurs are tangential views of shock fronts. There is no problem with this if the internal spurs are background features, as suggested for one of the most prominent in Sect. 5.5 below. However, if, as seems likely, at least some of the internal spurs are physically associated with Loop I, then we have to explain multiple concentric shock waves. The expected supernova rate for the Sco-Cen OB association is around $1\,\mathrm{Myr}^{-1}$ (de Geus 1992), while remnant lifetimes are conventionally $\lesssim$30 kyr, and in the low-density environment of a superbubble they are likely to be shorter. Therefore multiple active supernova remants within the superbubble are very unlikely, even if Loop I is powered by a much more massive OB association than Sco-Cen. However, if a re-energizing blast wave has recently run into the contact discontinuity at the outer surface of the superbubble, it will separate into a transmitted and reflected shock, and for any non-ideal geometry a rather complex pattern of crossing shocks is expected in the reflected wave. MHD simulations of this scenario would be illuminating, but are beyond the scope of this paper.

A very different model for the NPS has been proposed by Heiles (1998) and is implicitly applied to the internal filaments of Loop I by Vidal et al. (2015). In their geometry the NPS is not a tangential view of the superbubble boundary, since the solar system is on the bubble surface. The organized field pattern is due to the wrapping of a relatively ordered interstellar field over the surface of the expanding bubble. The spurs are bundles of field lines with an enhanced density of cosmic ray electrons and therefore enhanced synchrotron emission. An attractive feature of this is that a very simple geometric model gives a good qualitative fit to the field pattern in the loop. However, the model has the peculiarity that the emission is implied to be dominated by the far side of the loop; the near side, in which the viewer is embedded, would contribute a parallel polarization over the whole hemisphere, quite unlike the observed pattern. We note that in this model, Sh 2-27 can depolarize the loop emission even though located near the centre of the bubble.

A hybrid of the two models is possible if the solar system is moved off the loop surface in the Heiles geometry, so that the NPS resumes its usual role as the projected loop boundary. However, this would worsen the agreement of the model and observed field pattern, and is still subject to the problem that emission from the near surface of the bubble would give a much more uniform projected field.

5.3.4. Possible contamination of the CMB by Loop I?

Liu et al. (2014) have recently argued that emission from Loop I is contaminating current microwave background maps. Specifically, they demonstrate an alignment between the BHS small circle and positive peaks in the low-multipole ($\ell \leq 20$) structure of the WMAP ILC map (Bennett et al. 2013a); von Hausegger et al. (2016) confirm that the alignment is also seen in the *Planck* CMB maps[14]. Showed that the analysis by Liu et al. underestimated the probability, p, of a chance alignment, but von Hausegger et al. (2016) present a stronger statistical test that gives $p < 3 \times 10^{-3}$. The amplitude of these peaks is about ten times larger than worst-case errors due to foreground contamination in the ILC maps estimated by Bennett et al. (2013a), which occur around the edge of the mask recommended for use with their ILC map at low multipoles (Liu et al. applied no mask in their analysis). The most convincing alignment with the circle is in the southern Galactic hemisphere, including along the bottom-right section that we note above shows no sign of emission from the loop border. In general these peaks in Liu et al.'s low-l map show little correlation with the actual synchrotron or dust emission from Loop I, especially if we mask the Galactic plane as Bennett et al. recommend. We note that Liu et al. (2014) suggest that the contamination might be due to magnetic dipole emission from dust grains associated with Loop I. However, the securely-detected dust associated with Loop I is mostly located at larger radii than the synchrotron ridge, and would not itself give a significant signal in the analysis of Liu et al. (2014) or von Hausegger et al. (2016).

Moreover it seems unlikely that the dust in Loop I is particularly unusual; even if we posit a unique dust type in the loops, Mertsch & Sarkar (2013) have argued convincingly that similar structures are scattered throughout the Galactic disc and contribute a significant fraction of its synchrotron emission. By the same token, the proposed dust emission from distant loops should accumulate along the Galactic plane, but no such signal is apparent in the CMB maps. von Hausegger et al. (2016) argue that this expected signal is restricted to $|b| < 5°$, a region where component separation is unreliable (hence the need for a Galactic mask). While it is true that it is not possible to accurately estimate the CMB signal in this region, we can rule out foreground contamination at the level required by this model. The integrated brightness of the distant loops is is an order of magnitude larger than that of Loop I, and the features responsible for the Loop I alignment are among the brightest in the CMB maps after filtering to $l \leq 20$, with amplitudes 50–100 μK. Using this to scale the arbitrary units in Fig. 5 of von Hausegger et al., the brightness from distant loops on the Galactic plane

[14] Ogburn (2014).

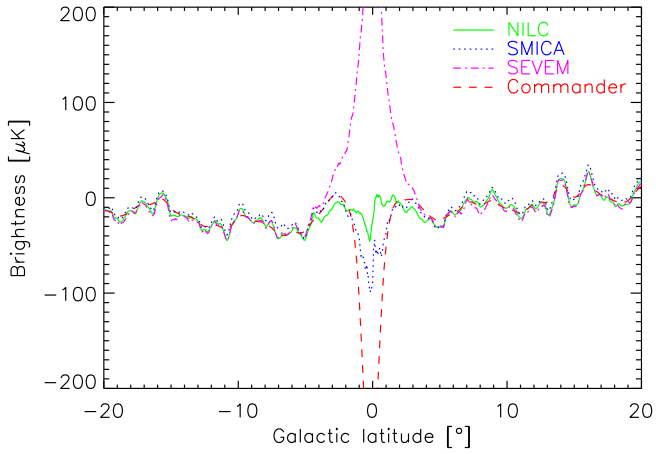

Fig. 26. Mean brightness vs. Galactic latitude, b, in the *Planck* CMB maps from Planck Collaboration IX (2016), in the range $|l| < 60°$. Solid green: NILC; dotted blue: SMICA; dot-dashed magenta: SEVEM (all at 5 arcmin resolution); dashed red: baseline Commander model at 1° resolution (Planck Collaboration X 2016). The first three methods all use inpainting to fill masked regions around bright compact features in some or all of the input maps: pixels affected by this have been omitted from the averaging. High amplitudes close to $b = 0$ are due to residual foreground contamination.

averaged over $|l| < 60°$ should be $\approx 900\,\mu$K, and is still over $100\,\mu$K at $|b| = 4°$. Figure 26 shows profiles of derived CMB brightness against b for the four main *Planck* component separation methods. Except for SEVEM, which is the method least well adapted to removing diffuse foregrounds, substantial contamination from Galactic foregrounds is confined to $|b| < 2°$. Even the SEVEM map has smaller Galactic residuals than predicted from the von Hausegger et al. analysis.

In short, there is little reason to believe in the contamination suggested by Liu et al. The alignment they suggest is with a theoretical schematic rather than the observed synchrotron loop, and is even further away from the actual dust emission in the loop. The formal improbability that the observed alignment occurs by chance, $p \approx 0.2\%$ in the best (i.e., *Planck*) CMB maps, should be offset against the low prior probability that this schematic accidentally aligns much better with a previously-undetected structure than with the synchrotron loop that it was intended to model. This p-value does not allow for any look-elsewhere effect such as potential alignments with other loops. Moreover, their proposed physical model implies additional strong contamination along the Galactic plane, which is not observed.

5.4. Other loops and spurs

Three other synchrotron loops that are generally agreed upon (e.g., Vidal et al. 2015), and there are a dozen or so shorter filaments or spurs, with several mutually-incompatible proposals for joining some of them into loops. Given our emphasis on the non-circularity of Loop I, and the fact that it seems all too easy to find small circles passing plausibly close to a sequence of ridges on the sky maps, we do not find any of these newly proposed loops convincing; however, their component spurs are certainly real. We discuss the more interesting examples in turn.

Loop II. Also known as the Cetus arc, Loop II is a very diffuse, 45°-radius structure centred at $(l, b) = (100°, -32.°5)$. The faint, broad emission on the left-hand side of the maps in Fig. 2 is attributed to it. As originally defined by Large et al. (1962), the right-hand end of the arc was considered to be the "South Polar Spur" (SPS), which descends from the plane at $l = 45°$ (visible in Figs. 20 and 21). The SPS is prominent in both the unsharp masked 408 MHz map and the synchrotron polarization map, but curves towards the right as it leaves the plane (as does its projected magnetic field), in the opposite direction from the notional path of Loop II; it therefore appears to be unrelated. The BHS small circle for Loop II just crosses the plane, but no emission from it has been traced in the northern Galactic hemisphere; the top of the loop may be obscured by Galactic plane emission, but it is also possible that the expanding shell was halted by the dense gas in the plane. Alternatively, Weaver (1979) and Heiles (1998) suggest that Loop III is its northern extension, although the two loops are offset by 24° in longitude. No reliable distance information is available for Loop II.

Figure 24 shows a coherent field pattern roughly parallel to the locus of Loop II that is not visible in the WMAP data. The polarized intensity essentially disappears into the noise at the bottom of the loop near the South Galactic Pole (SGP), but a coherent polarization field can be traced along a path that goes a few degrees further towards the SGP than the BHS fit, and closes a few degrees higher in longitude from the SPS. Some of this polarization is detected at 1.4 GHz by Wolleben et al. (2006), but the polarization angles are more disordered, presumably due to Faraday rotation, and so the alignment with the loop is not so clear.

Loop III. Loop III is centred at $(l, b) \approx (124°, 15.°5)$; BHS give a radius of 32.°5, although Figs. 20 and 24 show that polarized emission is detected several degrees further out. Loop III is clearly detected around most of its perimeter in the northern hemisphere in both total intensity and polarization. Its right-hand spur, rising from the plane directly above the Cyg X region, passes through the region of deep coverage near the North Ecliptic Pole $(l, b) \approx (96°, 30°)$ on the *Planck* maps, giving a particularly clean view of the well ordered magnetic field (Fig. 27). This Cygnus spur is relatively narrow ($FWHM \approx 5°$) until it reaches $b \approx 30°$ after which the loop becomes much broader and fainter. As it returns to the plane its polarization is obscured by the strongly polarized Fan region ($100° < l < 170°$), in which the magnetic field is parallel to the plane and therefore orthogonal to the expected field in the loop. BHS argue that the loop re-emerges from the fan region in the southern hemisphere at $l \approx 150°$, and the B-field pattern in our synchrotron polarization map is consistent with this, but the loop does not convincingly close in the south. Vidal et al. (2015) imply that their filament IIIs may be associated with Loop III proper, but this is one of the regions where WMAP and *Planck* disagree the most, and the existence of this filament is not confirmed in the *Planck* maps, except for a short section near $(l, b) = (82°, -30°)$ (see Fig. 24). Kun (2007) discusses possible interactions between Loop III and the cold gas north of the plane, notably the North Celestial Loop (Meyerdierks et al. 1991) that may be swept-up material.

Loop IV. Loop IV is centred at $(l, b) = (315°, 48.5°)$ and is projected entirely inside Loop I. Only an arc subtending $\approx 20°$ along its low-latitude rim is clear in our polarization map; see Vidal et al. (2015) for analysis. The high-latitude rim of Loop IV that parallels the top of the NPS is very noisy here but clear in the 21 cm polarization map of Wolleben et al. (2006).

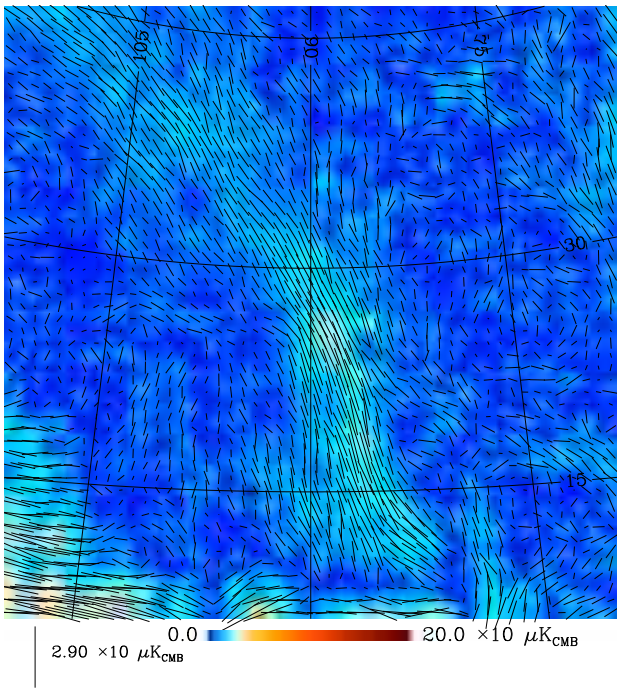

Fig. 27. Combined polarization map of the Cygnus spur, the right-hand end of Loop III. The map is centred at $(l, b) = (90°, +27°)$ and the graticule has a 15° spacing.

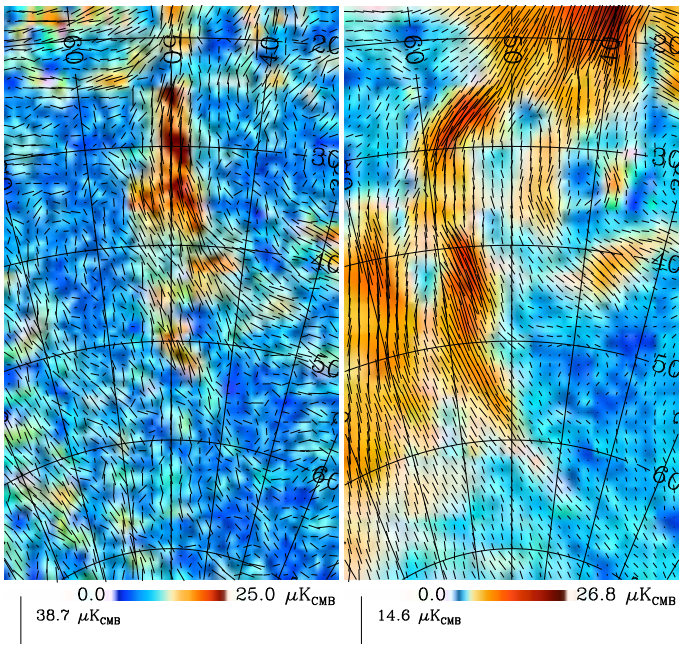

Fig. 28. The South Polar Spur. *Left*: *Planck*-WMAP polarization map; *right*: *Planck* 353-GHz dust polarization. The maps are centred at $(l, b) = (50°, -45°)$ and the graticule has a 10° spacing.

The South Polar Spur (SPS) and Filament X. As discussed above, the SPS was once seen as the low-longitude edge of Loop II, but in fact curves in the opposite direction so the outside edge of the SPS is to its right. It also forms the most prominent segment of the S1 loop proposed by Wolleben (2007), and was labelled filament VIIb by Vidal et al. (2015). Wolleben's view of the SPS was obscured by Faraday rotation near the plane; as noted by Vidal et al. (2015), the high frequency ($\gtrsim$20 GHz) polarization structure of the SPS is more strongly curved near the plane than expected for Wolleben's path. The other section identified by Wolleben as part of his new loop is usually seen as one of the interior ridges of Loop I and the northern part of Loop IV; thus, all components of loop S1 appear to be parts of smaller structures and there is no clear evidence that S1 exists as a coherent physical structure.

The SPS has its own cold border just outside the radio ridge, at $l \approx 60°$, $-30° > b > -70°$, which is particularly clear in dust polarization (Fig. 28). The border is visible in H I at $0 < v_{\rm LSR} < 10\,{\rm km\,s^{-1}}$ (Fig. 21d,e), which implies a distance of less than a few hundred parsecs.

Given our discussion above, we are reluctant to define a loop by extending a small circle from the clearly-detected arc of the SPS. In fact, a slightly fainter spur immediately north of the plane (Vidal et al.'s filament X) seems to be a reflection-symmetric twin of the SPS, suggesting a wasp-waisted cavity shaped by the dense gas in the plane (see the left-hand edge of Fig. 21c).

Our map allows filament X to be traced further north, to $b = 37°$, where it curves over and enters the region of bright diffuse polarized emission just outside the NPS (Fig. 25). Unusually, the field in this northern section is perpendicular to the filament. This alignment is not due to a contribution from the underlying diffuse emission; if it were, the filament would appear as a trough (due to cancellation), not a ridge in polarized intensity. A possible return section is marked in Fig. 20.

The Orion-Taurus Ridge and Filament XI. Unlike the other spurs, these features do not emerge from the Galactic plane but run parallel to it at closest approach, at $(l, b) \approx (220°, -15°)$, and $(l, b) \approx (230°, 40°)$, respectively (see Fig. 20). They are visible in both unsharp-masked total intensity and in polarization (see Fig. 2 of Vidal et al. 2015). Milogradov-Turin & Urošević (1997) and Borka et al. (2008) propose the existence of a pair of very large, overlapping loops (V and VI in their designation) that connect a sparse collection of features including the right-hand end (at $l < 180°$) of the Ori-Tau ridge and Vidal et al.'s filament IIIs. However, the rest of the Ori-Tau ridge curves far away from the locus of Loops V/VI, and the magnetic field continuously follows that curvature, so these loops appear to be spurious.

Filament XI is an approximately 80°-radius arc that seems to curve away from the plane at both ends (Fig. 20); however, it is unclear if features near $l = 264°$ belong to the left-hand end of Filament XI or the right-hand side of Loop I (or filament XII, if not part of Loop I). Extended to a full loop, Filament XI encloses most of Galactic quadrant 3 north of the Plane, which is one of the faintest regions of the polarized sky; over much of this quadrant no polarization is clearly detected by *Planck* and/or WMAP, even at 4° resolution.

$l = 45°$ feature. This is the highly-polarized patch covering $12° < b < 45°$ and from the edge of the NPS to $l \approx 50°$ (Fig. 25). The low-b edge of the polarization feature coincides with a rapid brightening of the inner halo in total intensity, and when polarization re-appears at $b \approx 8°$ it has an orthogonal orientation, roughly parallel to the Galactic plane. Hence this minimum is due to a cancellation between the plane-parallel field in the inner halo and the near-vertical field in our feature, and does not mark the physical edge. A faint ridge runs through the top half of the feature at $l \approx 45°$, which is just visible in the 408 MHz map (Fig. 21a,b); otherwise there is little trace in total intensity. The magnetic field runs at a slight angle to the ridge of the NPS throughout; in the adjacent section of the NPS the projected field

is misaligned with the ridge-line and in better agreement with that in the $l = 45°$ feature. Plausibly the feature overlaps in projection with Loop I, but if so the current data do not allow us to trace it inside the loop.

Smaller loops. Mertsch & Sarkar (2013) have emphasized that analogues to the large synchrotron loops should be common, and more distant and smaller examples should therefore be visible in the sky maps close to the Galactic plane. One rather clear example is the polarization structure south of the Cyg X region, centred at $(l, b) = (90°, -5°)$, which seems to be a superposition of a 5°-radius loop around this bright star-forming complex and another spur heading to the lower right (Fig. 29). The radius is about 120 pc, assuming a distance of 1.4 kpc for Cyg X (Rygl et al. 2012). A northern counterpart is less obvious, partly because of the two bright supernova remnants, HB 21 and W 63, that lie on the likely path. Figure 29 also shows another possible distant loop: the set of three arches in the southern hemisphere, centred near $l = 60°$; they are also marked in Fig. 20. The coherence of the polarization vectors allows the outer arch to be followed around to $(l, b) = (17.°4, -12.°9)$, just south of the Cygnus Loop supernova remnant. While the polarized intensity suggests that the inner arch returns to the plane at $l \approx 61°$, the polarization vectors are orthogonal to the apparent ridge-line, and so this might be a different structure. Figure 29 also shows that the dust polarization has the same magnetic pattern as the synchrotron emission around Cyg X. There is also a polarized dust filament that runs roughly along the inner edge of the middle $l = 60°$ arch, while the outer arch parallels the dust in polarization as it runs behind the SPS.

5.5. Fermi bubbles in polarization

The *Fermi* bubbles are two large structures extending perpendicular to the Galactic plane, up to about ±55°. They were first discovered by Dobler et al. (2010) using spatial templates while searching for a γ-ray counterpart to the microwave haze (e.g., Finkbeiner 2004; Planck Collaboration Int. IX 2013) in the *Fermi* data.

The origin of the bubbles is not clear, although their location and symmetry with respect to the Galactic centre suggest that they originate there. They have a γ-ray spectrum significantly harder than the inverse Comptom emission from the Galactic Halo or the one from pion decays from collisions of CR, with the ISM protons and heavier nuclei (Su et al. 2010). Different models have been proposed to explain their origin, most of them relating to a recent AGN-type activity at the Galactic centre. For a recent overview on the bubbles and their spectral behaviour in γ-ray, see Dobler (2012) and Ackermann et al. (2014).

We compare our combined *Planck*-WMAP polarization amplitude map at 28.4 GHz with a full-sky *Fermi* map from Ackermann et al. (2014). The γ-ray map was produced using 50 months of *Fermi* LAT data (Atwood et al. 2009), using only the "UltraClean" class events, i.e., the sample of events with less contamination from misclassified interactions in the *Fermi* LAT instrument. See Ackermann et al. (2014) for a detailed description on the *Fermi* data analysis. We use the high energy map, which covers 10–500 GeV. In this energy range, the emission from the *Fermi* bubbles appears clearly without any component separation at latitudes $b \gtrsim 20°$. The main foreground emission in gamma rays is from decay of π^0 particles produced by CR protons interacting with the ISM (Ackermann et al. 2012). If the CR density and spectrum are roughly spatially uniform over the

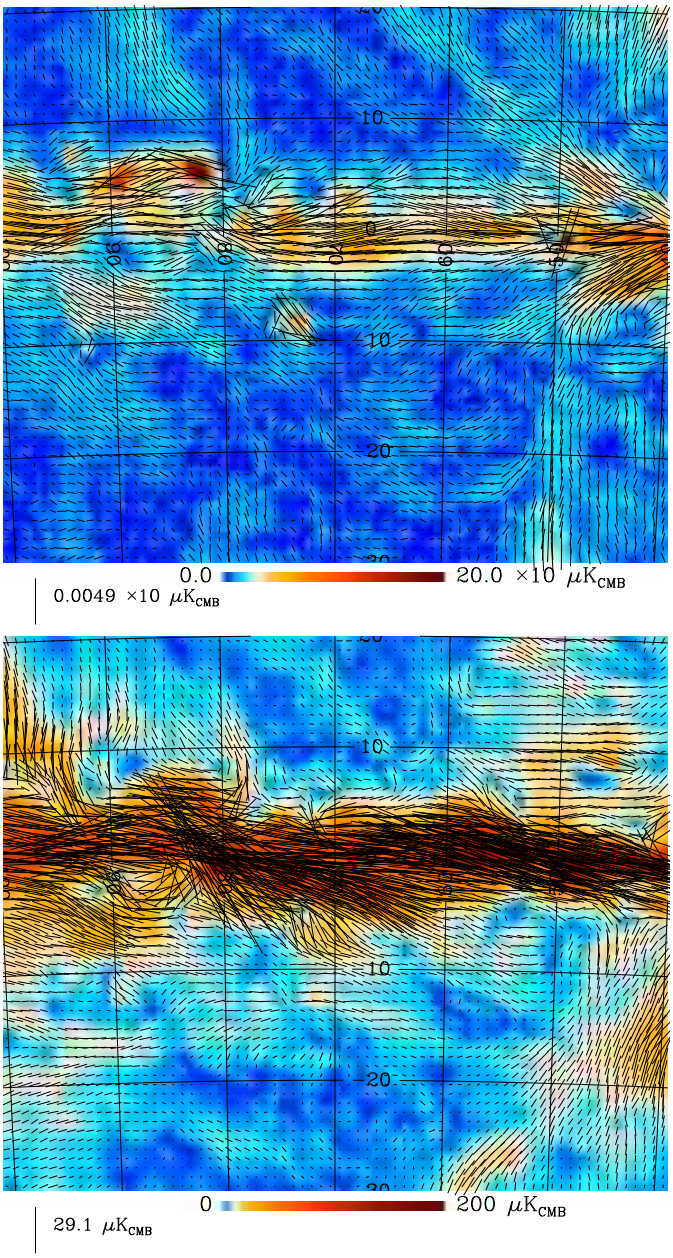

Fig. 29. *Top*: combined polarization map with magnetic field vectors overlaid, centred on $(l, b) = (70°, -7.°5)$ showing several polarized arches south of the plane. Bright compact features along the plane are all SNRs: DA 530 (G93.3+6.9); HB 21 (G89.2+4.7); W 63 (G82.2+5.3); CTB 87 (G74.9+1.2); the Cygnus Loop (G74.0−8.5); CTB 80 (G69.0+2.7); and W 51C (G49.1−0.6). The large spur at $l \approx 50°$ is the SPS. *Bottom*: dust polarization in the same region as seen at 353 GHz. Maps are rectangular projections and have an asinh colour scale.

Galaxy, then the π^0 emission will be proportional to the ISM column density (Su et al. 2010). A good tracer for the ISM column density are maps of thermal emission from dust grains, since dust is well mixed in the ISM and its emission is optically thin. Here, we use the *Planck* 353 GHz optical depth map from Planck Collaboration XI (2014) as a column-density proxy for π^0 emission to fit and remove it from the γ-ray map.

In the middle panel of Fig. 30, we show the resulting 10–500 GeV *Fermi* map. A region of about ±5°along the Galactic plane, where the subtraction of the scaled *Planck* 353 GHz map

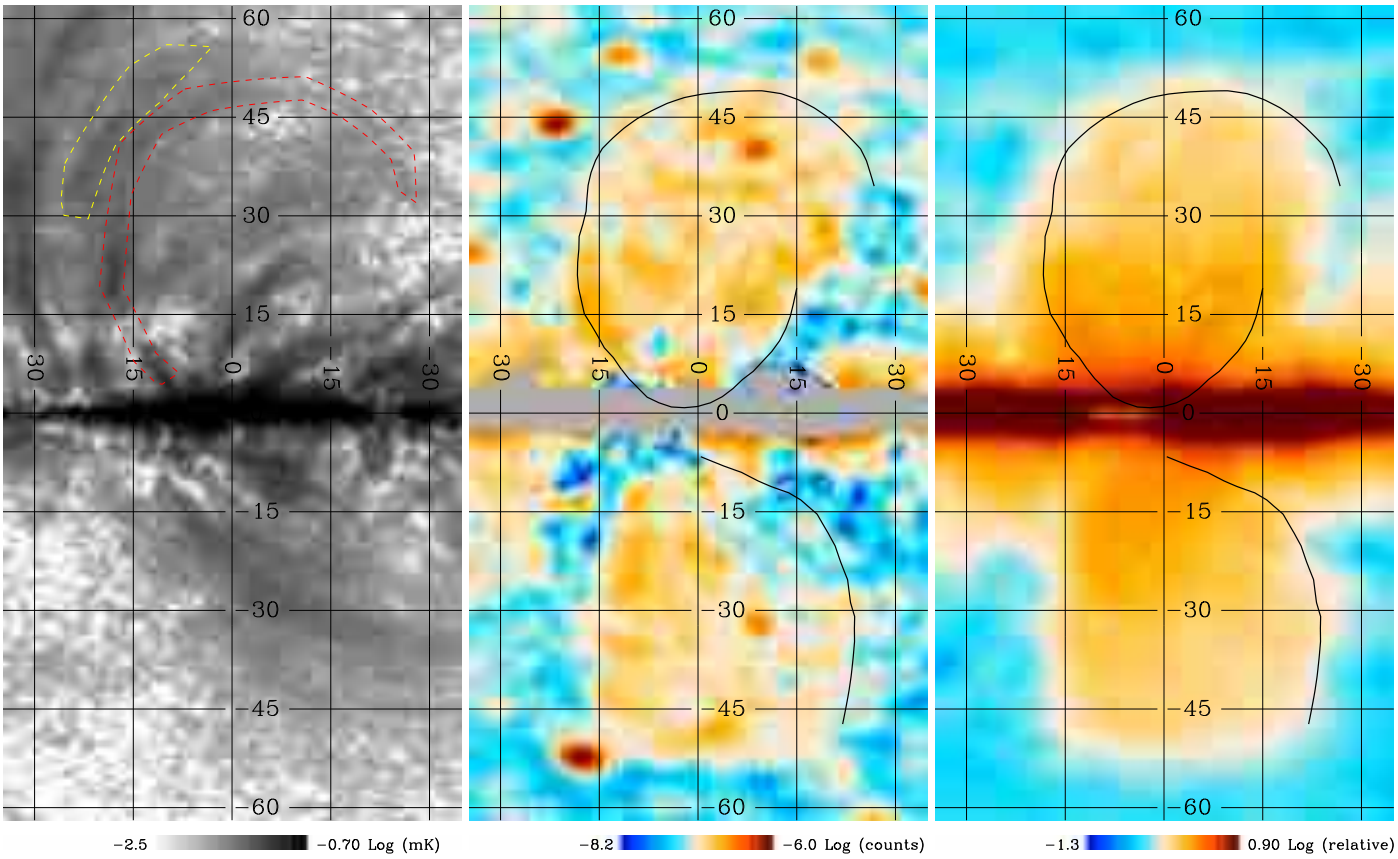

Fig. 30. *Left*: cartographic projection of the combined *Planck*-WMAP polarization amplitude, centred at the Galactic centre, with graticule lines at 15° intervals. The regions defined by red and yellow dashed lines were selected to calculate a polarized spectral index; in red is the filament around the *Fermi* bubble and in yellow a control area. *Centre*: cartographic projection of the 10–500 GeV map from Ackermann et al. (2014), with the π^0 emission subtracted as described in the text, showing the *Fermi* bubbles. *Right*: *Fermi* bubbles component from Selig et al. (2015). The black outline corresponds to the centre of the narrow filaments visible in the polarization map on the left.

left large residuals, has been masked out and is shown in grey. The left panel in Fig. 30 shows our combined *Planck*-WMAP polarization amplitude map, where narrow filaments are visible that correspond to the border of the *Fermi* bubbles. We note that the northern filament is much clearer than the southern one. The ridge-lines of these filaments is over-plotted in the *Fermi* map on the right to show the correspondence. It is remarkable to see how closely the polarized filament follows the border of the *Fermi* bubbles. We also show on the right panel the denoised and source-subtracted *Fermi* bubbles template constructed by Selig et al. (2015) using a Bayesian inference algorithm. Their reconstruction has a poorer angular resolution than the less processed version we show at the centre of Fig. 30, but still it is clear that the synchrotron filaments outline the border of the bubbles. The polarized filaments are unresolved in the *Planck* polarization maps (40′ FWHM beam), implying that these are very narrow synchrotron structures. This is further confirmation of a sharp border for the *Fermi* bubbles, and models that fail to predict this feature are now less favoured (see Dobler 2012 for a description of some of these models).

Polarization spectral index. We have measured the polarization spectral index, $\beta_{\rm pol}$, between the bias-corrected WMAP 23 GHz and *Planck* 30 GHz using T–T plots of a region that encompasses the north filament. The left panel of Fig. 30 shows two regions in the polarization intensity map that we selected to measure $\beta_{\rm pol}$, one including most of the northern filament (in red) and a second region that we use as control (yellow).

The T–T plots are shown in Fig. 31. The polarization spectral index of the *Fermi* bubble filament is $\beta_{\rm pol} = -2.54 \pm 0.16$, while the nearby control region has $\beta_{\rm pol} = -2.90 \pm 0.36$. The spectral index of the region that includes the filament is much flatter than the standard value of −3.0 normally assumed for diffuse synchrotron emission. It is also flatter than all the values presented in Fuskeland et al. (2014) and Vidal et al. (2015), who explored the polarized spectral indices in different regions using WMAP data. This flatter spectral index indicates that the energy distribution of the synchrotron radiation along the filament has more higher energy electrons than that of the diffuse component next to it. The polarization spectral index of the *Fermi* bubble filament we measure here is identical to the spectral index of the microwave haze of $\beta_{\rm Haze} = 2.54 \pm 0.05$ (Planck Collaboration Int. IX 2013). This supports the relationship between the filament and the haze/bubble emission.

Fermi bubbles and Loop I. A relationship between Loop I (see Sect. 5.3.1) and the *Fermi* bubbles has been hypothesized (e.g., Kataoka et al. 2013). This would put Loop I at the Galactic centre, with a much larger size and radio luminosity, as long argued by Sofue (e.g., Sofue 1977, 1994, 2015).

With the new *Planck*-WMAP combined polarization map, in Sect. 5.3.1 we trace Loop I below the Galactic plane. It is

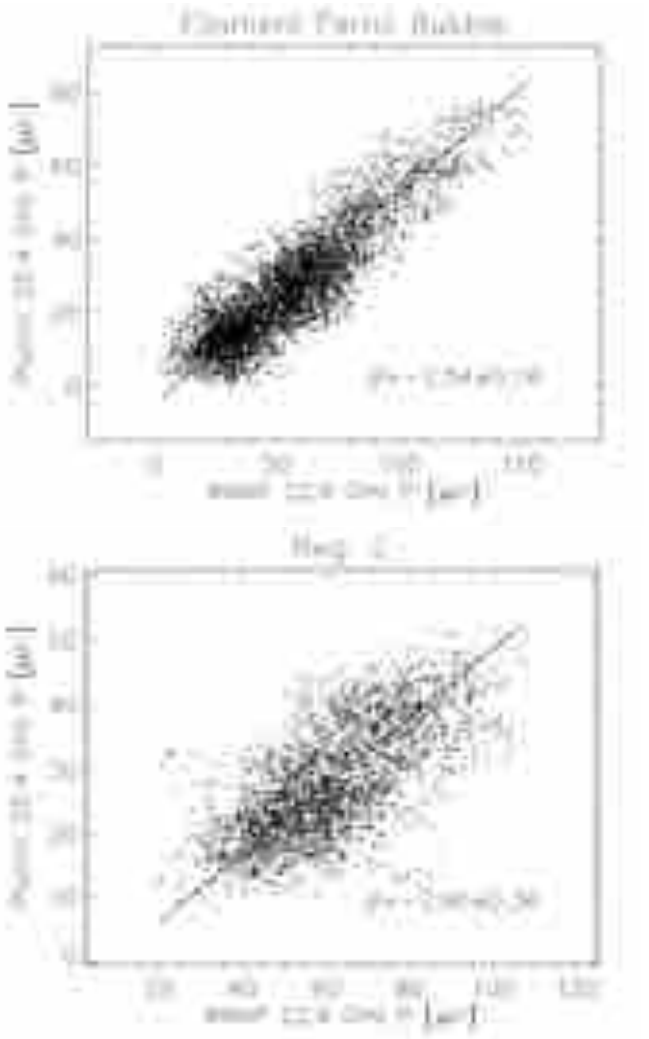

Fig. 31. *T–T* plots between the polarization amplitude maps of WMAP *K*-band and *Planck* 28.4 GHz. The two plots correspond to the regions defined in the left panel of Fig. 30. The *Fermi* bubble filament shows a flatter spectrum than the control region.

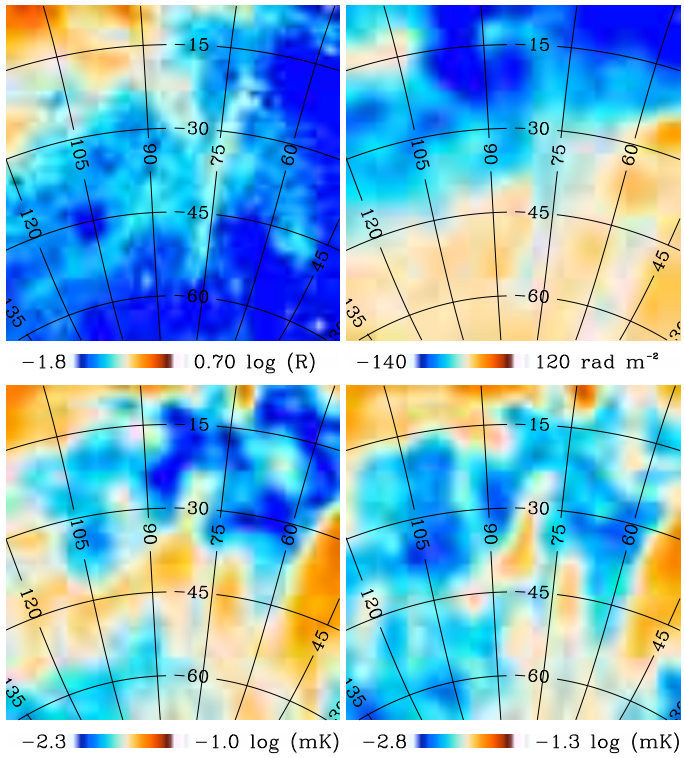

Fig. 32. *Top left*: Hα map in the velocity range $-80 < V_{\rm lsr} < -40\,{\rm km\,s^{-1}}$. Notice the vertical filament that runs at $l \approx 75°$ and $-60° < b < -20°$. *Top right*: Faraday depth map from Oppermann et al. (2012), which also shows a filament at the same location, with a mean value of $-25\,{\rm rad\,m^{-2}}$ along its extension. The filament has a counterpart in "absorption," visible as a trough in polarization intensity maps. *Bottom left*: WMAP 23 GHz polarization intensity map. *Bottom right*: *Planck*-WMAP polarization intensity map. The Hα map on the top left corner has an angular resolution of 1°, while the other three maps have a common resolution of 3°. The grid spacing is 15°.

clear from the top panel of Fig. 20 and from Fig. 30 that the southern part of the *Fermi* bubble extends outside Loop I, and there is no trace of an interaction with the bubble in the radio maps, given the continuity and smoothness of the Loop I polarized filaments in the southern hemisphere. The two structures must therefore be at different distances. The *Fermi* bubbles are well centred on the Galactic centre, show a pinched structure symmetric about the Galactic plane, as expected for an outburst from the nucleus (Sofue 1994), and are unique in the γ-ray sky. All this makes it highly likely that they are located at the distance of the Galactic centre, as usually assumed. In contrast, Loop I is centred 35° from the nucleus and significantly above the plane, while on its left-hand side, where it can be clearly followed, it appears to extend through the plane without any sign of deviation (Sect. 5.3.1). This is just as expected if it is relatively nearby and embedded in the disc rather than extending far beyond it. Of course, it also has a larger angular size than the *Fermi* bubbles, and there are at least several similar loops (Sect. 5.4). We are therefore confident that Loop I is a foreground feature.

5.6. An anti-correlation of an Hα filament and polarized intensity

Another interesting aspect that can help in the determination of the distance to some of the polarized structures is the discovery of a region that shows an anti-correlation between Hα emission and the polarized intensity in our combined *Planck*-WMAP map. This has not been noticed before as far as we are aware, because the filaments are located at high Galactic latitude, in the Faraday-thin regime.

In Fig. 32 we show an Hα map, integrated over the velocity range $-80 < V_{\rm lsr} < -40\,{\rm km\,s^{-1}}$, from the Wisconsin H-Alpha Mapper (WHAM) survey (Haffner et al. 2003). The filament that runs along $l \approx 75°$ is about 40° in length. The WMAP 22.8 GHz polarized intensity, and the *Planck*-WMAP polarized intensity map also shown in Fig. 32, show a trough at the same location as the Hα filament. This feature is also visible in the Faraday depth map from Oppermann et al. (2012), shown on the same figure. The Faraday depth, ϕ is proportional to the magnetic field along the line of sight and the electron density:

$$\phi = k_{\rm F} \int_{r_0}^{0} {\rm d}r\, n_{\rm e}(r) B_r(r). \tag{5}$$

We have ruled out a chance correlation since the polarized feature is also clearly visible, at higher angular resolution, in the maps from the GALFACTS (Taylor & Salter 2010) consortium

(Jereon Stil, priv. comm.), and the correlation is still strong at angular scales of a few arcmin.

The origin of the observed anti-correlation between Hα intensity and polarization amplitude is not clear. A first possibility is that the trough visible in the combined *Planck*-WMAP polarization map is a depolarized region, meaning that the Hα filament lies in between the polarized background emission and us. If this is the case, the ionized gas traced by the Hα map could produce Faraday rotation, due to the presence of a magnetic field in the plasma, depolarizing the diffuse background emission along its extension. However, this hypothesis is not compatible with the low density of the ionized gas. The intensity of the filament in Hα is 2 R above the background at the original resolution (6′) of the Finkbeiner (2003) Hα map. This corresponds to a mean electron density of 2.0 cm^{-3} (assuming that the filament has a thickness of 1 pc), which is very low to produce significant Faraday rotation at 23 GHz for typical values of the magnetic field. Moreover, the Faraday depth map from Oppermann et al. (2012) has a value of about 25 rad m^{-2} along the filament, which corresponds to a 0°.3 change in polarization angle at 23 GHz. Therefore, Faraday rotation of this high latitude filament is not enough to cause any major depolarization at 23 GHz.

A second alternative is that there could be a strong coherent magnetic field parallel to the line of sight along the filament. This might be the result of the dynamical processes that created the filament. If this is the case, there would be less polarized emission at the filament location than around it.

Lastly, it might well be that the synchrotron emission from the region of the Hα filament is intrinsically weakly polarized. This might be due to a less organized magnetic field in this region in comparison with the diffuse emission seen in the vicinity of the filament on the polarization map.

We also note the fact that the Hα filament is only visible at negative radial velocities. This corresponds to the velocity range of the Perseus arm of the Galaxy. If the Hα filament belongs to that arm, it would imply that the distance to the diffuse synchrotron background is much larger than a few hundred parsecs, lying at least 2 kpc away from us.

5.7. Limits on AME polarization

If AME is solely due to spinning dust particles, then we expect it to have a very low polarization percentage. The level of spinning dust polarization depends on the alignment efficiency of the small grains and PAHs in the interstellar magnetic field. Lazarian & Draine (2000) considered resonance paramagnetic relaxation, which predicts $\lesssim$1.5% polarization for frequencies $\gtrsim$20 GHz; Hoang et al. (2013) use constraints on the alignment of grains seen in ultraviolet polarization to predict that AME will have a polarization of $\lesssim$0.9% at frequencies above 20 GHz. At lower frequencies ($\lesssim$10 GHz), the polarization fraction will be higher, but as the AME spectrum steeply decreases at low frequencies while other foreground components are increasing, this will be more difficult to detect than at the peak of the AME spectrum. Given this, and the fact that the observed polarization percentage would naturally be less than this due to beam and line-of-sight depolarization, we do not expect to detect significant AME polarization with *Planck*, i.e., the polarization percentage should be $\lesssim$1%.

Observational constraints on AME polarization have so far been placed using relatively compact, isolated clouds, where AME is known to be strong. Rubiño-Martín et al. (2012a) review the available constraints and their relation to theoretical models. The best constraint comes from the Perseus region, which has significant AME emission and relatively little contaminating synchrotron emission. Battistelli et al. (2006) reported a weak detection in Perseus at $3.4^{+1.5}_{-1.9}$% at 11 GHz, while later measurements obtained by López-Caraballo et al. (2011) using WMAP data found a 2σ limit of <1%; Dickinson et al. (2011) have also measured a 2σ limit of <1.4% for Perseus (as well as an upper limit of <1.7% in ρ Ophiuchus), and Génova-Santos et al. (2015) found a 2σ limit of <2.8% in Perseus at 19 GHz. Recently, Battistelli et al. (2015) have claimed to detect polarized AME emission at 21.5 GHz from RCW 175, an H II region, where they measured a polarization percentage of (2.2 ± 0.2 (random) ± 0.3 (systematic))% at 21.5 GHz. However, Battistelli et al. (2015) argue that a large fraction of this signal could be residual synchrotron radiation, leaving little or no polarized AME. There have been very few attempts to constrain the polarization from the large-scale diffuse AME; Kogut et al. (2007) find that AME accounts for less than 1% of the total polarized signal, while Macellari et al. (2011) placed a limit of <5% based on template fitting of WMAP data. Planck Collaboration Int. XXII (2015) placed upper limits by correlating WMAP and *Planck* polarization maps with the *Planck* 353 GHz dust polarization map. They found that the correlation turned upwards at low frequencies, and at WMAP K-band they placed an upper limit on AME polarization of 16%; they also noted that the upturn could be explained by dust-correlated synchrotron polarization rather than AME polarization.

We use the debiased polarization map assembled using a weighted average of both *Planck* and WMAP data (see Sect. 5.1) to look for polarized emission that is correlated with diffuse AME from the `Commander` solution. We note that the weighted polarized map assumes a spectral index of $\beta = -3.0$, rather than an AME-like spectrum. We create T–T plots between the AME and polarization intensities, both rescaled to μK at 22.8 GHz, in order to measure the percentage polarization. Assuming that any potential AME polarization has a constant percentage across the region, then this should result in a linear correlation of the data points in the T–T plots. We use the uncertainty maps and assume a model uncertainty of 10% for both the `Commander` AME solution and the weighted polarization map; the latter uncertainty is subdominant in these regions. We fit for the slope of the correlation, which directly gives the percentage polarization. We repixelize the maps to $N_{\rm side} = 64$ to ensure that the pixels are independent. We note that the debiasing method used will not perfectly remove all of the noise bias, particularly in regions of low S/N, but any residual bias should be lower than the thermal noise limits where the S/N is low.

We focus on two high latitude regions from Sect. 4.2, namely Perseus and the Pegasus plume. We show the AME and debiased polarization maps in Fig. 33, and the AME–polarization T–T plot for each region in Fig. 34. AME dominates the total emission at around 20–30 GHz in both of these regions. Unlike regions such as Corona Australis and Musca, which are strongly contaminated by highly polarized Galactic synchrotron structures (see Sect. 5.2), Perseus and the Pegasus plume are in parts of the sky with relatively little synchrotron polarization, although the Pegasus plume does have two polarized synchrotron features crossing the region; these can be seen in Fig. 33 and are marked on Fig. 20. One of these synchrotron arcs is somewhat aligned with the AME plume, however it is unrelated to the plume, since it extends beyond the plume towards the Galactic plane. The morphology of the polarized and total intensity synchrotron emission is quite different in the region of the plume, and the aligned arc is either highly polarized or has a flat spectrum,

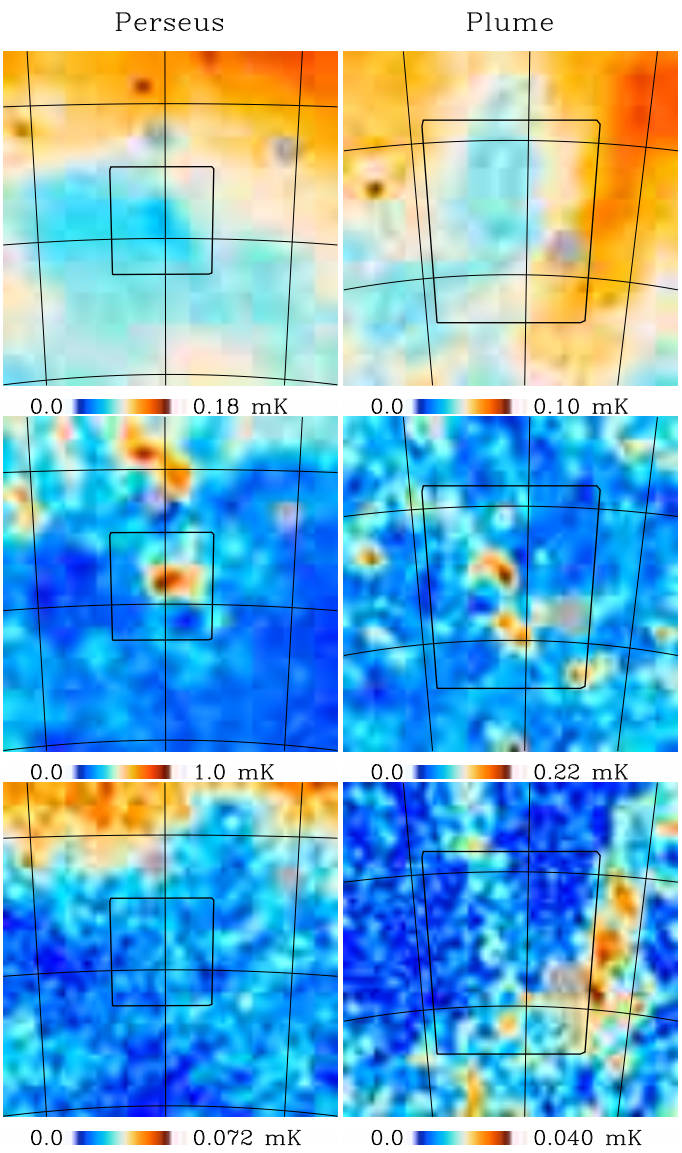

Fig. 33. *Top*: `Commander` synchrotron component maps; *middle*: `Commander` AME component maps; and *bottom*: debiased weighted polarization maps. *Left*: Perseus; *right*: the Pegasus plume. The colour scales are linear here. The regions are defined and masked as per Sect. 4.2. The Perseus region does not contain significant polarized synchrotron emission, while the Pegasus plume contains several polarized synchrotron arcs.

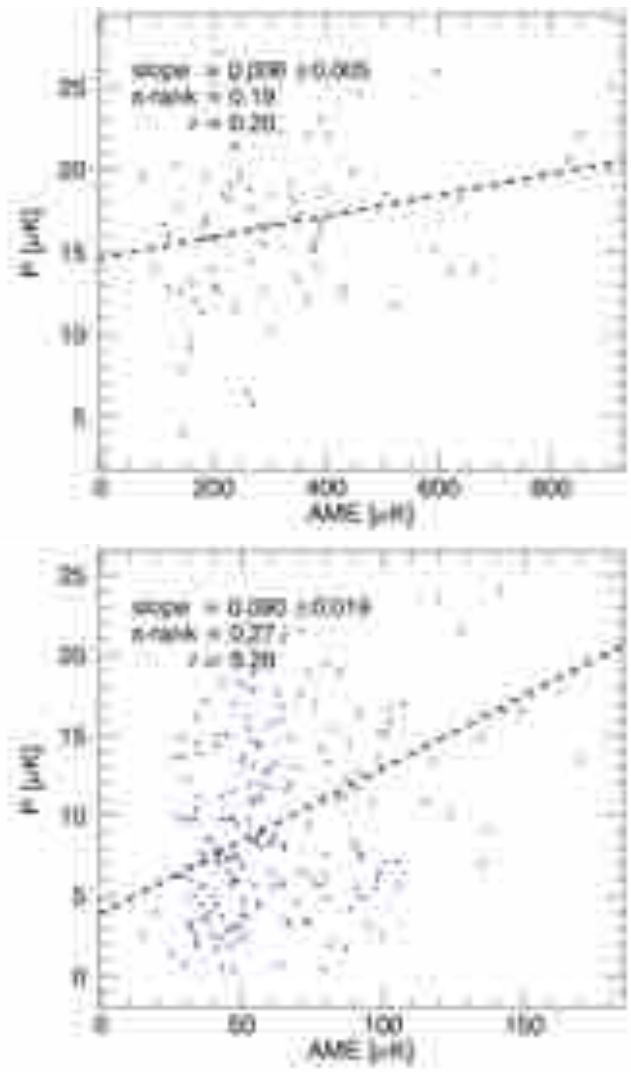

Fig. 34. *T*–*T* plots between the polarization and AME intensities (both in units of μK at 22.8 GHz). *Top*: Perseus; *bottom*: Pegasus plume. The scatter is mostly due to thermal noise in the polarization map (uncertainties in the polarization intensity in these regions are typically around 5 μK). The fitted slope gives the polarization fraction for the region, based on the linear fit (dashed line).

since it is faint in the total intensity map. Unlike the Perseus and Pegasus plume regions, the Orion and λ Orionis regions contain strong free-free emission: while free-free emission is unpolarized there may be residual leakage from total intensity to polarization. In addition there is a broad background of polarized synchrotron emission in these regions, and due to their proximity to the Galactic plane there will be a correlation between synchrotron and thermal dust emission, simply because both components will be brighter towards the Galactic plane than they are off-plane. We apply the point source mask described in Sect. 4.2: in the regions of interest this only consists of masking one point source near the Pegasus plume.

We find that the strongest constraint comes from Perseus, where we measure an AME polarization percentage (compared with the overall polarization intensity) of 0.6±0.5%, which gives a 2σ limit of <1.6%, matching previous constraints. The Pearson correlation coefficient is 0.20. An improved `Commander` estimate of the AME in this region (see Sect. 4.2) would decrease this upper limit by around 40%. In the Pegasus plume region we find a polarization percentage of 9.0 ± 1.9%, with a Pearson correlation coefficient of 0.29, which, given the presence of correlated polarized synchrotron emission, we interpret to be a 2σ limit of <12.8%. We attempt to subtract some of the polarized synchrotron emission by assuming that the intensity is 10% polarized, which removes some of the synchrotron emission from the region near the point source. This reduces the polarization percentage relative to the AME to 5.2 ± 1.6%, or a 2σ limit of <8.4%, with a Pearson correlation coefficient of 0.24; assuming a higher level of synchrotron polarization results in significant negative pixels in the polarization map. We also compare the weighted low-frequency polarization map with the polarized dust emission at 353 GHz by separately comparing the Q and U maps at the two frequencies, at $N_{\rm side}$ = 64, in the regions of Perseus and the Pegasus plume. Similar analysis was performed by Planck Collaboration Int. XXII (2015) across the whole sky. We find similar results, with no significant detection in Perseus,

and a weak detection in the Pegasus plume, which we ascribe to dust-correlated polarized synchrotron emission, as described above.

In summary, we do not find strong evidence for diffuse polarized AME in WMAP/*Planck* data, with a 2σ upper limit of 1.6% in the Perseus region. In order to improve on current constraints, we will need either reduced noise levels in regions that are free of polarized synchrotron emission (such as Perseus) or the ability to subtract accurately the synchrotron emission from less clear regions. The forthcoming map of polarized synchrotron emission at 5 GHz by the *C*-Band All Sky Survey (King et al. 2014) will assist with the latter issue.

6. Conclusions

In this paper we have discussed the Galactic foreground emission observed by WMAP/*Planck* between 20 and 100 GHz. The total intensity emission comprises at least three distinct components: synchrotron; free-free; and AME, commonly attributed to spinning dust. These components emit smooth continua that are typically decreasing with frequency. It is therefore extremely difficult to separate these components with any precision. Furthermore, these individual components are often spatially correlated (e.g., towards the Galactic plane).

We have applied an internal linear combination technique to WMAP/*Planck* data to produce a map that is free of CMB, free-free, and thermal dust. This has given us some insight into the spectral form of emission at 23 GHz. For most of the intensity analysis we rely on the component-separation products from the `Commander` code. This involved fitting a parametric model to the data. However, a number of simplifications have had to be made, given the limited number of frequencies and complexity of the foreground emission. In particular, we have not so far been able to produce a detailed synchrotron map in intensity. Instead we have had to rely on a `GALPROP` spectral model to take into account the bulk of the synchrotron emission above 20 GHz. In polarization the situation is somewhat clearer. The polarization maps at 20–50 GHz are dominated by synchrotron radiation; free-free and AME are expected to have very low polarization fractions.

Nevertheless, in this study we have been able to produce reasonable products for free-free and AME, from which we have inferred some physical results. Our polarization results do not rely directly on component separation.

The main conclusions from our study are as follows.

- After applying an ILC procedure to remove CMB, free-free, and thermal dust emission at 22.8 GHz, we find that the residual emission has significant spectral variations. This emission is expected to be dominated by (weak) synchrotron and (stronger) AME emission. In particular, we find that for some regions the spectrum is flatter than that of free-free emission ($\beta = -2.1$).
- The aforementioned areas are largely towards bright H II regions such as the ζ Ophiuchi cloud (Sh 2-27)and the California nebula. Because synchrotron emission is not observed to be flatter than about $\beta = -2.3$, the spectral changes are thought to be due to a high frequency component of spinning dust. Indeed, Planck Collaboration Int. XV (2014) found evidence for a spinning dust peak at around 50 GHz for the California nebula.
- Our free-free map appears to correspond well to previous maps made with WMAP data, and also to Hα maps at high latitudes (where dust absorption is small). The amplitude relativ to Hα is lower than the theoretical value for typical electron temperatures, as has been found in previous studies.
- A natural explanation for the low free-free-to-Hα ratio is that there is significant scattered Hα light. We have attempted to estimate this fraction by correlating Hα residuals (after subtracting the mean correlation) with the dust optical depth. We do indeed find a correlation with the thermal dust optical depth. If we assume that electron temperature varies by no more than ± 1000 K, we find that the scattered Hα emission accounts for $28 \pm 12\%$, or $36 \pm 12\%$ after making a nominal correction for absorption by dust.
- We also compared the `Commander` free-free map to the RRL Galactic plane survey of Alves et al. (2015). Again, we find a good overall correspondence between the maps. However, there are significant differences, which might be due to variations in electron temperature.
- The `Commander` AME map is closely correlated with thermal dust emission, as traced by FIR/sub-mm maps. We have identified several new diffuse regions away from the Galactic plane that appear to emit significant AME. These regions are typically associated with large dust cloud complexes. We have compared the emissivity of AME in these regions relative to the amount of thermal dust emission. The AME emissivity against 545 GHz and τ_{353} varies by a factor of approximately 2 from region to region. The λ Orionis region has a particularly high emissivity that warrants further investigation, ideally in conjunction with additional low-frequency data to reduce leakage between the free-free and AME components.
- Comparison of the `Commander` foreground products with similar products from the WMAP team shows that the amplitude of synchrotron emission is significantly lower in our analysis. This is particularly the case at low latitudes, where our fixed spectral model cannot account for the flatter index reported by WMAP and in earlier *Planck* analyses. To compensate, our AME amplitude is significantly higher by a factor of around 2–4 (depending on which model is being compared). The free-free component is in better agreement in general, but our model is typically lower by about 10–30%, which has been noted before (Alves et al. 2010, 2012). We emphasize that our model fits the data extremely accurately, with median residuals along the Galactic plane of <1% for *Planck* and < 2% for WMAP channels (Planck Collaboration X 2016).
- We have combined WMAP/*Planck* polarization maps to construct a higher S/N polarized intensity map. This is the highest S/N synchrotron polarization map available above a few GHz, where Faraday rotation can be safely ignored.
- The new polarization map shows a number of large-scale polarization structures, including spurs and filaments. These new features are detected clearly only in polarization, indicating a high polarization fraction similar to the brighter well-known spurs.
- The halo of synchrotron emission in the inner Galaxy clearly visible at 408 MHz appears to have a low polarization fraction (<10%) compared to the high-latitude spurs with typical polarization fractions of 30–50%. The diffuse high-latitude emission is also weakly (though detectably) polarized (<15%).
- We discuss in detail the characteristics of Loop I. The new polarization maps enables us to follow it further into the southern Galactic hemisphere, where there is a substantial deviation from the small circle fitted to the brighter northern part, presumably due to the inhomogenous environment.

Radio depolarization, X-ray absorption, and tomographic mapping of the local ISM all suggest that the loop is at least several times more distant than the traditional 120 pc.

- The projected magnetic field outside the North Polar spur parallels the loop, supporting the model that the loop is in part shaped by its interaction with the ambient magnetic field.
- The filaments projected inside Loop I are mostly associated with it, possibly a system of internal shock waves created when a re-energizing supernova shock reflected from the old boundary of the cavity. Alternatively, in accordance with the model of Vidal et al. (2015), they might be a system of "illuminated" field lines on the back hemisphere of the loop cavity.
- On several grounds we are not convinced by the suggestion of Liu et al. (2014) that emission from the loop is seriously contaminating derived CMB maps.
- We trace the magnetic field in Loop II for the first time. It follows the path of the loop, as in the other examples. We show that the most prominent feature in the original definition of Loop II is actually unrelated, and so the loop is somewhat smaller and fainter than previously believed.
- The proposed extension to Loop III in the south suggested by Vidal et al. (2015) is largely an artefact in the WMAP maps.
- The South Polar Spur, previously identified as the low-l edge of Loop II, is actually the high-l edge of a smaller structure. Just like for Loop I, there is a filament of cold material (traced by H I and thermal dust) running just outside it, with parallel magnetic field. From the H I velocity the distance is at most a few hundred pc.
- Loops V and VI (Milogradov-Turin & Urošević 1997) and S1 (Wolleben 2007) are not physical structures; our map shows that major components of the proposed loops deviate radically from the expected path. These components are independent features, with much smaller angular size than the suggested loops.
- We find two examples of smaller and more distant loops, one of which arcs around the Cyg X star-forming region. Both are associated with polarized dust features.
- We observe a clear outline of narrow highly polarized intensity around the northern Fermi bubble above the Galactic centre. The spectral index appears to be much flatter ($\beta = -2.54 \pm 0.16$) than other filaments, but similar to that found for the microwave haze. This is indicative of a more energetic population of electrons along these lines of sight. We note that the Southern extension of the *Fermi* bubble extends further south than Loop I, which probably rules out an association of Loop I with the *Fermi* bubbles.
- We have discovered examples of anti-correlation of Hα and polarized synchrotron intensity. The most striking is a high latitude Hα filament that appears as a local minimum in polarization. Because of the low density of ionized gase we can rule out Faraday depolarization. The observed anti-correlation appears to be real in that there is no synchrotron emission emanating from the region of the Hα filament. The negative velocity of Hα and the longitude imply that the filament could be lying at a distance of at least 2 kpc.
- We correlated the polarized maps with the `Commander` AME map. We found that there was no significant correlation except for the Pegasus plume region, where a low level ($9.0 \pm 1.9\%$) of polarization was observed, consistent with contamination from surrounding synchrotron radiation.

Although we are beginning to understand the diffuse emission at WMAP/*Planck* frequencies, there is still a long way to go. In intensity, the component separation is still a major difficulty. In particular, we have not been able to constrain the synchrotron spectral dependence, due to the degeneracy and confusion with free-free, AME, and CMB. New data in the frequency range 2–15 GHz are needed to more fully characterize all of the low-frequency foreground components. Experiments such as S-PASS at 2.3 GHz (Carretti 2011), C-BASS at 5 GHz (King et al. 2014), and QUIJOTE at 11–19 GHz (Rubiño-Martín et al. 2012b) will improve the situation considerably.

In polarization, the emerging picture is that synchrotron emission is by far the dominant polarized component below 50 GHz, with very little contribution from free-free and AME. The diffuse synchrotron emission has now been measured with good S/N for a large fraction of sky. However, there are still regions where the S/N is low. More importantly, the detailed spectral dependence of synchrotron emission is still unknown.

Acknowledgements. This paper is dedicated to the memory of the late Professor Rodney Deane Davies CBE FRS and Professor Richard John Davis OBE, both of whom contributed greatly to the *Planck* project. The Planck Collaboration acknowledges the support of: ESA; CNES and CNRS/INSU-IN2P3-INP (France); ASI, CNR, and INAF (Italy); NASA and DoE (USA); STFC and UKSA (UK); CSIC, MINECO, JA, and RES (Spain); Tekes, AoF, and CSC (Finland); DLR and MPG (Germany); CSA (Canada); DTU Space (Denmark); SER/SSO (Switzerland); RCN (Norway); SFI (Ireland); FCT/MCTES (Portugal); ERC and PRACE (EU). A description of the Planck Collaboration and a list of its members, indicating which technical or scientific activities they have been involved in, can be found at `http://www.cosmos.esa.int/web/planck/planck-collaboration`. This research was supported by an ERC Starting (Consolidator) Grant (no. 307209) and STFC Consolidated Grant (no. ST/L000768/1). We have made extensive use of the `HEALPix` package and the IDL astronomy library. This research has made use of the SIMBAD database, operated at CDS, Strasbourg, France.

References

Abdo, A. A., Ackermann, M., Ajello, M., et al. 2009, Phys. Rev. Lett., 102, 181101
Ackermann, M., Ajello, M., Atwood, W. B., et al. 2010, Phys. Rev. D, 82, 092004
Ackermann, M., Ajello, M., Atwood, W. B., et al. 2012, ApJ, 750, 3
Ackermann, M., Albert, A., Atwood, W. B., et al. 2014, ApJ, 793, 64
Adams, W. S. 1941, ApJ, 93, 11
Ali-Haïmoud, Y., Hirata, C. M., & Dickinson, C. 2009, MNRAS, 395, 1055
Atwood, W. B., Abdo, A. A., Ackermann, M., et al. 2009, ApJ, 697, 1071
Alves, M. I. R., Davies, R. D., Dickinson, C., et al. 2010, MNRAS, 405, 1654
Alves, M. I. R., Davies, R. D., Dickinson, C., et al. 2012, MNRAS, 422, 2429
Alves, M. I. R., Calabretta, M., Davies, R. D., et al. 2015, MNRAS, 450, 2025
Banday, A. J., Dickinson, C., Davies, R. D., Davis, R. J., & Górski, K. M. 2003, MNRAS, 345, 897
Barnes, D. G., Staveley-Smith, L., de Blok, W. J. G., et al. 2001, MNRAS, 322, 486
Barnes, J. E., Wood, K., Hill, A. S., & Haffner, L. M. 2015, MNRAS, 447, 559
Battistelli, E. S., Rebolo, R., Rubiño-Martín, J. A., et al. 2006, ApJ, 645, L141
Battistelli, E. S., Carretti, E., Cruciani, A., et al. 2015, ApJ, 801, 111
Bennett, C. L., Hill, R. S., Hinshaw, G., et al. 2003, ApJS, 148, 97
Bennett, C. L., Larson, D., Weiland, J. L., et al. 2013a, ApJS, 208, 20
Bennett, C. L., Larson, D., Weiland, J. L., et al. 2013b, ApJS, 208, 20
Berkhuijsen, E. M. 1971, A&A, 14, 359
Berkhuijsen, E. M., Haslam, C. G. T., & Salter, C. J. 1971, A&A, 14, 252
Bernard, J.-P., Reach, W. T., Paradis, D., et al. 2008, AJ, 136, 919
Borka, V., Milogradov-Turin, J., & Urošević, D. 2008, Astron. Nachr., 329, 397
Borken, R. J., & Iwan, D.-A. C. 1977, ApJ, 218, 511
Bot, C., Ysard, N., Paradis, D., et al. 2010, A&A, 523, A20
Brandt, T. D., & Draine, B. T. 2012, ApJ, 744, 129
Brouw, W. N., & Spoelstra, T. A. T. 1976, A&AS, 26, 129
Brown, J. C., & Taylor, A. R., 2001, ApJ, 563, L31
Carretti, E. 2011, J. Astrophys. Astron., 32, 457
Casassus, S., Cabrera, G. F., Förster, F., et al. 2006, ApJ, 639, 951
Casassus, S., Dickinson, C., Cleary, K., et al. 2008, MNRAS, 391, 1075
Chen, W. P., & Graham, J. A. 1993, ApJ, 409, 319
Condon, J. J. 1992, ARA&A, 30, 575
Davies, R. D., Elliott, K. H., & Meaburn, J. 1976, MmRAS, 81, 89
Davies, R. D., Dickinson, C., Banday, A. J., et al. 2006, MNRAS, 370, 1125
de Geus, E. J., 1992, A&A, 262, 258

de Oliveira-Costa, A., Tegmark, M., Davies, R. D., et al. 2004, ApJ, 606, L89
de Oliveira-Costa, A., Tegmark, M., Gaensler, B. M., et al. 2008, MNRAS, 388, 247
de Zeeuw, P. T., Hoogerwerf, R., de Bruijne, J. H. J., Brown, A. G. A., & Blaauw, A. 1999, AJ, 117, 354
Dickinson, C., Davies, R. D., & Davis, R. J. 2003, MNRAS, 341, 369
Dickinson, C., Eriksen, H. K., Banday, A. J., et al. 2009, ApJ, 705, 1607
Dickinson, C., Peel, M., & Vidal, M. 2011, MNRAS, 418, L35
Dobler, G. 2012, ApJ, 750, 17
Dobler, G., & Finkbeiner, D. P. 2008a, ApJ, 680, 1222
Dobler, G., & Finkbeiner, D. P. 2008b, ApJ, 680, 1235
Dobler, G., Finkbeiner, D. P., Cholis, I., Slatyer, T., & Weiner, N. 2010, ApJ, 717, 825
Dong, R., & Draine, B. T. 2011, ApJ, 727, 35
Draine, B. T. 2011, Physics of the Interstellar and Intergalactic Medium (Princeton University Press)
Draine, B. T., & Hensley, B. 2012, ApJ, 757, 103
Draine, B. T., & Lazarian, A. 1998, ApJ, 508, 157
Draine, B. T., & Lazarian, A. 1999, ApJ, 512, 740
Eriksen, H. K., Jewell, J. B., Dickinson, C., et al. 2008, ApJ, 676, 10
Fich, M., Blitz, L., & Stark, A. A. 1989, ApJ, 342, 272
Finkbeiner, D. P. 2003, ApJS, 146, 407
Finkbeiner, D. P. 2004, ApJ, 614, 186
Finkbeiner, D. P., Davis, M., & Schlegel, D. J. 1999, ApJ, 524, 867
Freyberg, M. J., & Egger, R. 1999, in Highlights in X-ray Astronomy, eds. B. Aschenbach, & M. J. Freyberg, 278
Frisch, P. C. 1981, Nature, 293, 377
Frisch, P. C., Redfield, S., & Slavin, J. D. 2011, ARA&A, 49, 237
Fukui, Y., Okamoto, R., Kaji, R., et al. 2014, ApJ, 796, 59
Fuskeland, U., Wehus, I. K., Eriksen, H. K., & Næss, S. K. 2014, ApJ, 790, 104
Gaensler, B. M. 1998, ApJ, 493, 781
Gaensler, B. M., Madsen, G. J., Chatterjee, S., & Mao, S. A. 2008, PASA, 25, 184
Génova-Santos, R., Rubiño-Martín, J. A., Rebolo, R., et al. 2015, MNRAS, 452, 4169
Ghosh, T., Banday, A. J., Jaffe, T., et al. 2012, MNRAS, 422, 3617
Gold, B., Odegard, N., Weiland, J. L., et al. 2011, ApJS, 192, 15
Górski, K. M., Hivon, E., Banday, A. J., et al. 2005, ApJ, 622, 759
Haffner, L. M., Reynolds, R. J., Tufte, S. L., et al. 2003, ApJS, 149, 405
Harju, J., Haikala, L. K., Mattila, K., et al. 1993, A&A, 278, 569
Harris, J., & Zaritsky, D. 2009, AJ, 138, 1243
Haslam, C. G. T., Salter, C. J., Stoffel, H., & Wilson, W. E. 1982, A&AS, 47, 1
Hauser, M. G., Arendt, R. G., Kelsall, T., et al. 1998, ApJ, 508, 25
Haverkorn, M., Brown, J. C., Gaensler, B. M., & McClure-Griffiths, N. M. 2008, ApJ, 680, 362
Heiles, C. 1984, ApJS, 55, 585
Heiles, C. 1998, in The Local Bubble and Beyond, ed. D. Breitschwerdt, M. J. Freyberg, & J. Truemper (Berlin: Springer Verlag), Lect. Not. Phys., 506, 227
Hensley, B. S., & Draine, B. T. 2015, ArXiv e-prints [arXiv:1505.02157v1], unpublished
Hensley, B. S., Draine, B. T., & Meisner, A. M. 2016, ApJ, 827, 25
Hilditch, R. W., Howarth, I. D., & Harries, T. J. 2005, MNRAS, 357, 304
Hoang, T., Lazarian, A., & Martin, P. G. 2013, ApJ, 779, 152
Israel, F. P., Wall, W. F., Raban, D., et al. 2010, A&A, 519, A67
Iwan, D. 1980, ApJ, 239, 316
Jarosik, N., Bennett, C. L., Dunkley, J., et al. 2011, ApJS, 192, 14
Jonas, J. L., Baart, E. E., & Nicolson, G. D. 1998, MNRAS, 297, 977
Jordan, C. H., Walsh, A. J., Lowe, V., et al. 2015, MNRAS, 448, 2344
Kalberla, P. M. W., Burton, W. B., Hartmann, D., et al. 2005, A&A, 440, 775
Kataoka, J., Tahara, M., Totani, T., et al. 2013, ApJ, 779, 57
Kim, S.-H., Martin, P. G., & Hendry, P. D. 1994, ApJ, 422, 164
King, O. G., Jones, M. E., Blackhurst, E. J., et al. 2014, MNRAS, 438, 2426
Klein, U., Haynes, R. F., Wielebinski, R., & Meinert, D. 1993, A&A, 271, 402
Kogut, A., Dunkley, J., Bennett, C. L., et al. 2007, ApJ, 665, 355
Kun, M. 2007, in IAU Symp., 237, eds. B. G. Elmegreen, & J. Palous, 119
Lagache, G. 2003, A&A, 405, 813
Laing, R. A. 1980, MNRAS, 193, 439
Lallement, R., Vergely, J.-L., Valette, B., et al. 2014, A&A, 561, A91
Lang, W. J., & Masheder, M. R. W. 1998, PASA, 15, 70
Lang, W. J., Masheder, M. R. W., Dame, T. M., & Thaddeus, P. 2000, A&A, 357, 1001
Large, M. I., Quigley, M. J. S., & Haslam, C. G. T. 1962, MNRAS, 124, 405
Lawson, K. D., Mayer, C. J., Osborne, J. L., & Parkinson, M. L. 1987, MNRAS, 225, 307
Lazarian, A., & Draine, B. T. 2000, ApJ, 536, L15
Leach, S. M., Cardoso, J., Baccigalupi, C., et al. 2008, A&A, 491, 597
Leahy, J. P. 1991, in Beams and Jets in Astrophysics, ed. P. A. Hughes (Cambridge University Press), 100
Leahy, J. P., Bersanelli, M., D'Arcangelo, O., et al. 2010, A&A, 520, A8
Leitch, E. M., Readhead, A. C. S., Pearson, T. J., & Myers, S. T. 1997, ApJ, 486, L23
Liu, H., Mertsch, P., & Sarkar, S. 2014, ApJ, 789, L29
López-Caraballo, C. H., Rubiño-Martín, J. A., Rebolo, R., & Génova-Santos, R. 2011, ApJ, 729, 25
Macellari, N., Pierpaoli, E., Dickinson, C., & Vaillancourt, J. E. 2011, MNRAS, 418, 888
Maddalena, R. J., & Morris, M. 1987, ApJ, 323, 179
Magnani, L., Blitz, L., & Mundy, L. 1985, ApJ, 295, 402
Mathewson, D. S., & Ford, V. L. 1970, MmRAS, 74, 139
McGee, R. X., & Newton, L. M. 1972, Austr. J. Phys., 25, 619
Meisner, A. M., & Finkbeiner, D. P. 2014, ApJ, 781, 5
Mertsch, P., & Sarkar, S. 2013, JCAP, 6, 41
Meyerdierks, H., Heithausen, A., & Reif, K. 1991, A&A, 245, 247
Milogradov-Turin, J., & Urošević, D. 1997, Bull. Astron. Belgrade, 155, 41
Miville-Deschênes, M., & Lagache, G. 2005, ApJS, 157, 302
Montier, L., Plaszczynski, S., Levrier, F., et al. 2015, A&A, 574, A136
Murphy, E. J., Bremseth, J., Mason, B. S., et al. 2012, ApJ, 761, 97
Neuhäuser, R., & Forbrich, J. 2008, in Handbook of Star Forming Regions, Volume II, ed. B. Reipurth, 735
Ogburn, IV, R. W. 2014, ArXiv e-prints [arXiv:1409.7354]
Oppermann, N., Junklewitz, H., Robbers, G., et al. 2012, A&A, 542, A93
Orlando, E., & Strong, A. 2013, MNRAS, 436, 2127
Page, L., Hinshaw, G., Komatsu, E., et al. 2007, ApJS, 170, 335
Paladini, R., Davies, R. D., & De Zotti, G. 2004, MNRAS, 347, 237
Peterson, D. E., Caratti o Garatti, A., Bourke, T. L., et al. 2011, ApJS, 194, 43
Pietrzyński, G., Graczyk, D., Gieren, W., et al. 2013, Nature, 495, 76
Planck Collaboration XIII. 2011, A&A, 536, A13
Planck Collaboration XVII. 2011, A&A, 536, A17
Planck Collaboration XIX. 2011, A&A, 536, A19
Planck Collaboration XX. 2011, A&A, 536, A20
Planck Collaboration XXI. 2011, A&A, 536, A21
Planck Collaboration II. 2014, A&A, 571, A2
Planck Collaboration IX. 2014, A&A, 571, A9
Planck Collaboration XI. 2014, A&A, 571, A11
Planck Collaboration XII. 2014, A&A, 571, A12
Planck Collaboration I. 2016, A&A, 594, A1
Planck Collaboration II. 2016, A&A, 594, A2
Planck Collaboration III. 2016, A&A, 594, A3
Planck Collaboration IV. 2016, A&A, 594, A4
Planck Collaboration V. 2016, A&A, 594, A5
Planck Collaboration VI. 2016, A&A, 594, A6
Planck Collaboration VII. 2016, A&A, 594, A7
Planck Collaboration VIII. 2016, A&A, 594, A8
Planck Collaboration IX. 2016, A&A, 594, A9
Planck Collaboration X. 2016, A&A, 594, A10
Planck Collaboration XI. 2016, A&A, 594, A11
Planck Collaboration XII. 2016, A&A, 594, A12
Planck Collaboration XIII. 2016, A&A, 594, A13
Planck Collaboration XIV. 2016, A&A, 594, A14
Planck Collaboration XV. 2016, A&A, 594, A15
Planck Collaboration XVI. 2016, A&A, 594, A16
Planck Collaboration XVII. 2016, A&A, 594, A17
Planck Collaboration XVIII. 2016, A&A, 594, A18
Planck Collaboration XIX. 2016, A&A, 594, A19
Planck Collaboration XX. 2016, A&A, 594, A20
Planck Collaboration XXI. 2016, A&A, 594, A21
Planck Collaboration XXII. 2016, A&A, 594, A22
Planck Collaboration XXIII. 2016, A&A, 594, A23
Planck Collaboration XXIV. 2016, A&A, 594, A24
Planck Collaboration XXV. 2016, A&A, 594, A25
Planck Collaboration XXVI. 2016, A&A, 594, A26
Planck Collaboration XXVII. 2016, A&A, 594, A27
Planck Collaboration XXVIII. 2016, A&A, 594, A28
Planck Collaboration Int. IX. 2013, A&A, 554, A139
Planck Collaboration Int. XII. 2013, A&A, 557, A53
Planck Collaboration Int. XIV. 2014, A&A, 564, A45
Planck Collaboration Int. XV. 2014, A&A, 565, A103
Planck Collaboration Int. XVII. 2014, A&A, 566, A55
Planck Collaboration Int. XIX. 2015, A&A, 576, A104
Planck Collaboration Int. XX. 2015, A&A, 576, A105
Planck Collaboration Int. XXII. 2015, A&A, 576, A107
Planck Collaboration Int. XXIII. 2015, A&A, 580, A13
Planck Collaboration Int. XXX. 2016, A&A, 586, A133
Platania, P., Burigana, C., Maino, D., et al. 2003, A&A, 410, 847

Puspitarini, L., & Lallement, R. 2012, A&A, 545, A21
Puspitarini, L., Lallement, R., Vergely, J.-L., & Snowden, S. L. 2014, A&A, 566, A13
Quigley, M. J. S., & Haslam, C. G. T. 1965, Nature, 208, 741
Reed, B. C. 2003, AJ, 125, 2531
Reich, P., & Reich, W. 1988, A&AS, 74, 7
Reich, P., Testori, J. C., & Reich, W. 2001, A&A, 376, 861
Reich, P., Reich, W., & Testori, J. C. 2004, in The Magnetized Interstellar Medium, eds. B. Uyaniker, W. Reich, & R. Wielebinski, 63
Remazeilles, M., Delabrouille, J., & Cardoso, J.-F. 2011a, MNRAS, 410, 2481
Remazeilles, M., Delabrouille, J., & Cardoso, J.-F. 2011b, MNRAS, 418, 467
Remazeilles, M., Dickinson, C., Banday, A. J., Bigot-Sazy, M.-A., & Ghosh, T. 2015, MNRAS, 451, 4311
Rezaeikh, S., Javadi, A., Khosroshahi, H., & van Loon, J. T. 2014, MNRAS, 445, 2214
Rubiño-Martín, J. A., López-Caraballo, C. H., Génova-Santos, R., & Rebolo, R. 2012a, Adv. Astron., 2012
Rubiño-Martín, J. A., Rebolo, R., Aguiar, M., et al. 2012b, in SPIE Conf. Ser., 8444
Rygl, K. L. J., Brunthaler, A., Sanna, A., et al. 2012, A&A, 539, A79
Salter, C. J. 1983, Bull. Astron. Soc. India, 11, 1
Santos, F. P., Corradi, W., & Reis, W. 2011, ApJ, 728, 104
Schlafly, E. F., Green, G., Finkbeiner, D. P., et al. 2015, ApJ, 799, 116
Selig, M., Vacca, V., Oppermann, N., & Enßlin, T. A. 2015, A&A, 581, A126
Sharpless, S. 1959, ApJS, 4, 257
Shaver, P. A., McGee, R. X., Newton, L. M., Danks, A. C., & Pottasch, S. R. 1983, MNRAS, 204, 53
Silsbee, K., Ali-Haïmoud, Y., & Hirata, C. M. 2011, MNRAS, 411, 2750
Snowden, S. L., Egger, R., Freyberg, M. J., et al. 1997, ApJ, 485, 125
Sofue, Y. 1977, A&A, 60, 327
Sofue, Y. 1994, ApJ, 431, L91
Sofue, Y. 2015, MNRAS, 447, 3824
Spoelstra, T. A. T. 1972, A&A, 21, 61
Strong, A. W., Moskalenko, I. V., & Ptuskin, V. S. 2007, Annu. Rev. Nucl. Part. Sci., 57, 285
Strong, A. W., Orlando, E., & Jaffe, T. R. 2011, A&A, 534, A54
Su, M., Slatyer, T. R., & Finkbeiner, D. P. 2010, ApJ, 724, 1044
Takekawa, S., Oka, T., Tanaka, K., et al. 2014, ApJS, 214, 2
Taylor, A. R., & Salter, C. J. 2010, in The Dynamic Interstellar Medium: A Celebration of the Canadian Galactic Plane Survey, eds. R. Kothes, T. L. Landecker, & A. G. Willis, ASP Conf. Ser., 438, 402
Tibbs, C. T., Watson, R. A., Dickinson, C., et al. 2010, MNRAS, 402, 1969
Tibbs, C. T., Paladini, R., & Dickinson, C. 2012, Adv. Astron., 2012, 41
Tibbs, C. T., Scaife, A. M. M., Dickinson, C., et al. 2013, ApJ, 768, 98
van der Laan, H. 1962, MNRAS, 124, 179
van Leeuwen, F. 2007, Hipparcos, the New Reduction of the Raw Data, Astrophys. Space Sci. Lib., 350 (Berlin: Springer)
Vergely, J.-L., Valette, B., Lallement, R., & Raimond, S. 2010, A&A, 518, A31
Vidal, M., Dickinson, C., Davies, R. D., & Leahy, J. P. 2015, MNRAS, 452, 656
Vidal, M., Leahy, J. P., & Dickinson, C. 2016, MNRAS, in press [arXiv:1410.4436]
von Hausegger, S., Liu, H., Mertsch, P., & Sarkar, S. 2016, J. Cosmol. Astropart. Phys., 3, 023
Wade, C. M. 1957, AJ, 62, 148
Wardle, J. F. C., & Kronberg, P. P. 1974, ApJ, 194, 249
Watson, R. A., Rebolo, R., Rubiño-Martín, J. A., et al. 2005, ApJ, 624, L89
Weaver, H. 1979, in The Large-Scale Characteristics of the Galaxy, ed. W. B. Burton, IAU Symp., 84, 295
Wehus, I. K., Fuskeland, U., Eriksen, H. K., et al. 2016, A&A, in press, DOI: 10.1051/0004-6361/201525659
Wenger, M., Ochsenbein, F., Egret, D., et al. 2000, A&AS, 143, 9
Whitney, B. A., Sewilo, M., Indebetouw, R., et al. 2008, AJ, 136, 18
Whittet, D. C. B., Prusti, T., Franco, G. A. P., et al. 1997, A&A, 327, 1194
Willingale, R., Hands, A. D. P., Warwick, R. S., Snowden, S. L., & Burrows, D. N. 2003, MNRAS, 343, 995
Witt, A. N., Gold, B., Barnes, III, F. S., et al. 2010, ApJ, 724, 1551
Woermann, B., Gaylard, M. J., & Otrupcek, R. 2000, MNRAS, 315, 241
Wolleben, M. 2007, ApJ, 664, 349
Wolleben, M., Landecker, T. L., Reich, W., & Wielebinski, R. 2006, A&A, 448, 411
Wong, T., Hughes, A., Ott, J., et al. 2011, ApJS, 197, 16
Wood, K., & Reynolds, R. J. 1999, ApJ, 525, 799
Ysard, N., Miville-Deschênes, M. A., & Verstraete, L. 2010, A&A, 509, L1
Zhang, C. Y., Laureijs, R. J., Chlewicki, G., Wesselius, P. R., & Clark, F. O. 1989, A&A, 218, 231

[1] APC, AstroParticule et Cosmologie, Université Paris Diderot, CNRS/IN2P3, CEA/lrfu, Observatoire de Paris, Sorbonne Paris Cité, 10 rue Alice Domon et Léonie Duquet, 75205 Paris Cedex 13, France
[2] Aalto University Metsähovi Radio Observatory and Dept of Radio Science and Engineering, PO Box 13000, 00076 Aalto, Finland
[3] African Institute for Mathematical Sciences, 6-8 Melrose Road, Muizenberg, Cape Town, South Africa
[4] Agenzia Spaziale Italiana Science Data Center, via del Politecnico snc, 00133 Roma, Italy
[5] Aix Marseille Université, CNRS, LAM (Laboratoire d'Astrophysique de Marseille) UMR 7326, 13388 Marseille, France
[6] Astrophysics Group, Cavendish Laboratory, University of Cambridge, J J Thomson Avenue, Cambridge CB3 0HE, UK
[7] Astrophysics & Cosmology Research Unit, School of Mathematics, Statistics & Computer Science, University of KwaZulu-Natal, Westville Campus, Private Bag X54001, 4000 Durban, South Africa
[8] Atacama Large Millimeter/submillimeter Array, ALMA Santiago Central Offices, Alonso de Cordova 3107, Vitacura, Casilla 763 0355, Santiago, Chile
[9] CGEE, SCS Qd 9, Lote C, Torre C, 4° andar, Ed. Parque Cidade Corporate, CEP 70308-200, Brasília, DF, Brazil
[10] CITA, University of Toronto, 60 St. George St., Toronto, ON M5S 3H8, Canada
[11] CNRS, IRAP, 9 Av. colonel Roche, BP 44346, 31028 Toulouse Cedex 4, France
[12] CRANN, Trinity College, Dublin, Ireland
[13] California Institute of Technology, Pasadena, California, USA
[14] Centre for Theoretical Cosmology, DAMTP, University of Cambridge, Wilberforce Road, Cambridge CB3 0WA, UK
[15] Centro de Estudios de Física del Cosmos de Aragón (CEFCA), Plaza San Juan, 1, planta 2, 44001 Teruel, Spain
[16] Computational Cosmology Center, Lawrence Berkeley National Laboratory, Berkeley, California, USA
[17] Consejo Superior de Investigaciones Científicas (CSIC), Madrid, Spain
[18] DSM/Irfu/SPP, CEA-Saclay, 91191 Gif-sur-Yvette Cedex, France
[19] DTU Space, National Space Institute, Technical University of Denmark, Elektrovej 327, 2800 Kgs. Lyngby, Denmark
[20] Département de Physique Théorique, Université de Genève, 24 Quai E. Ansermet, 1211 Genève 4, Switzerland
[21] Departamento de Astrofísica, Universidad de La Laguna (ULL), 38206 La Laguna, Tenerife, Spain
[22] Departamento de Física, Universidad de Oviedo, Avda. Calvo Sotelo s/n, Oviedo, Spain
[23] Department of Astronomy and Astrophysics, University of Toronto, 50 Saint George Street, Toronto, Ontario, Canada
[24] Department of Astrophysics/IMAPP, Radboud University Nijmegen, PO Box 9010, 6500 GL Nijmegen, The Netherlands
[25] Department of Physics & Astronomy, University of British Columbia, 6224 Agricultural Road, Vancouver, British Columbia, Canada
[26] Department of Physics and Astronomy, Dana and David Dornsife College of Letter, Arts and Sciences, University of Southern California, Los Angeles, CA 90089, USA
[27] Department of Physics and Astronomy, University College London, London WC1E 6BT, UK
[28] Department of Physics, Florida State University, Keen Physics Building, 77 Chieftan Way, Tallahassee, Florida, USA
[29] Department of Physics, Gustaf Hällströmin katu 2a, University of Helsinki, 00560 Helsinki, Finland
[30] Department of Physics, Princeton University, Princeton, New Jersey, USA
[31] Department of Physics, University of California, Santa Barbara, California, USA
[32] Department of Physics, University of Illinois at Urbana-Champaign, 1110 West Green Street, Urbana, Illinois, USA
[33] Dipartimento di Fisica e Astronomia G. Galilei, Università degli Studi di Padova, via Marzolo 8, 35131 Padova, Italy

[34] Dipartimento di Fisica e Scienze della Terra, Università di Ferrara, via Saragat 1, 44122 Ferrara, Italy
[35] Dipartimento di Fisica, Università La Sapienza, P.le A. Moro 2, 00185 Roma, Italy
[36] Dipartimento di Fisica, Università degli Studi di Milano, via Celoria, 16, 20133 Milano, Italy
[37] Dipartimento di Fisica, Università degli Studi di Trieste, via A. Valerio 2, 34127 Trieste, Italy
[38] Dipartimento di Matematica, Università di Roma Tor Vergata, via della Ricerca Scientifica 1, 00185 Roma, Italy
[39] Discovery Center, Niels Bohr Institute, Blegdamsvej 17, 1165 Copenhagen, Denmark
[40] European Southern Observatory, ESO Vitacura, Alonso de Cordova 3107, Vitacura, Casilla 19001, Santiago, Chile
[41] European Space Agency, ESAC, Planck Science Office, Camino bajo del Castillo, s/n, Urbanización Villafranca del Castillo, Villanueva de la Cañada, Madrid, Spain
[42] European Space Agency, ESTEC, Keplerlaan 1, 2201 AZ Noordwijk, The Netherlands
[43] Gran Sasso Science Institute, INFN, viale F. Crispi 7, 67100 L'Aquila, Italy
[44] HGSFP and University of Heidelberg, Theoretical Physics Department, Philosophenweg 16, 69120 Heidelberg, Germany
[45] Haverford College Astronomy Department, 370 Lancaster Avenue, Haverford, Pennsylvania, USA
[46] Helsinki Institute of Physics, Gustaf Hällströmin katu 2, University of Helsinki, 00560 Helsinki, Finland
[47] INAF – Osservatorio Astrofisico di Catania, via S. Sofia 78, Catania, Italy
[48] INAF – Osservatorio Astronomico di Padova, Vicolo dell'Osservatorio 5, Padova, Italy
[49] INAF – Osservatorio Astronomico di Roma, via di Frascati 33, Monte Porzio Catone, Italy
[50] INAF – Osservatorio Astronomico di Trieste, via G.B. Tiepolo 11, Trieste, Italy
[51] INAF/IASF Bologna, via Gobetti 101, Bologna, Italy
[52] INAF/IASF Milano, via E. Bassini 15, Milano, Italy
[53] INFN, Sezione di Bologna, viale Berti Pichat 6/2, 40127 Bologna, Italy
[54] INFN, Sezione di Ferrara, via Saragat 1, 44122 Ferrara, Italy
[55] INFN, Sezione di Roma 1, Università di Roma Sapienza, Piazzale Aldo Moro 2, 00185 Roma, Italy
[56] INFN, Sezione di Roma 2, Università di Roma Tor Vergata, via della Ricerca Scientifica 1, 00185 Roma, Italy
[57] INFN/National Institute for Nuclear Physics, via Valerio 2, 34127 Trieste, Italy
[58] IPAG: Institut de Planétologie et d'Astrophysique de Grenoble, Université Grenoble Alpes, IPAG; CNRS, IPAG, 38000 Grenoble, France
[59] IUCAA, Post Bag 4, Ganeshkhind, Pune University Campus, Pune 411 007, India
[60] Imperial College London, Astrophysics group, Blackett Laboratory, Prince Consort Road, London, SW7 2AZ, UK
[61] Infrared Processing and Analysis Center, California Institute of Technology, Pasadena, CA 91125, USA
[62] Institut Néel, CNRS, Université Joseph Fourier Grenoble I, 25 rue des Martyrs, 38042 Grenoble, France
[63] Institut Universitaire de France, 103 Bd Saint-Michel, 75005 Paris, France
[64] Institut d'Astrophysique Spatiale, CNRS, Univ. Paris-Sud, Université Paris-Saclay, Bât. 121, 91405 Orsay Cedex, France
[65] Institut d'Astrophysique de Paris, CNRS (UMR7095), 98 bis Boulevard Arago, 75014 Paris, France
[66] Institut für Theoretische Teilchenphysik und Kosmologie, RWTH Aachen University, 52056 Aachen, Germany
[67] Institute of Astronomy, University of Cambridge, Madingley Road, Cambridge CB3 0HA, UK
[68] Institute of Theoretical Astrophysics, University of Oslo, Blindern, 0371 Oslo, Norway
[69] Instituto de Astrofísica de Canarias, C/Vía Láctea s/n, 38200 La Laguna, Tenerife, Spain
[70] Instituto de Física de Cantabria (CSIC-Universidad de Cantabria), Avda. de los Castros s/n, 39005 Santander, Spain
[71] Istituto Nazionale di Fisica Nucleare, Sezione di Padova, via Marzolo 8, 35131 Padova, Italy
[72] Jet Propulsion Laboratory, California Institute of Technology, 4800 Oak Grove Drive, Pasadena, California, USA
[73] Jodrell Bank Centre for Astrophysics, Alan Turing Building, School of Physics and Astronomy, The University of Manchester, Oxford Road, Manchester, M13 9PL, UK
[74] Kavli Institute for Cosmological Physics, University of Chicago, Chicago, IL 60637, USA
[75] Kavli Institute for Cosmology Cambridge, Madingley Road, Cambridge, CB3 0HA, UK
[76] Kazan Federal University, 18 Kremlyovskaya St., 420008 Kazan, Russia
[77] LAL, Université Paris-Sud, CNRS/IN2P3, 91898 Orsay, France
[78] LERMA, CNRS, Observatoire de Paris, 61 Avenue de l'Observatoire, Paris, France
[79] Laboratoire AIM, IRFU/Service d'Astrophysique – CEA/DSM – CNRS – Université Paris Diderot, Bât. 709, CEA-Saclay, 91191 Gif-sur-Yvette Cedex, France
[80] Laboratoire Traitement et Communication de l'Information, CNRS (UMR 5141) and Télécom ParisTech, 46 rue Barrault, 75634 Paris Cedex 13, France
[81] Laboratoire de Physique Subatomique et Cosmologie, Université Grenoble-Alpes, CNRS/IN2P3, 53 rue des Martyrs, 38026 Grenoble Cedex, France
[82] Laboratoire de Physique Théorique, Université Paris-Sud 11 & CNRS, Bâtiment 210, 91405 Orsay, France
[83] Lawrence Berkeley National Laboratory, Berkeley, California, USA
[84] Lebedev Physical Institute of the Russian Academy of Sciences, Astro Space Centre, 84/32 Profsoyuznaya st., 117997 Moscow, GSP-7, Russia
[85] Max-Planck-Institut für Astrophysik, Karl-Schwarzschild-Str. 1, 85741 Garching, Germany
[86] Max-Planck-Institut für Extraterrestrische Physik, Giessenbachstraße, 85748 Garching, Germany
[87] McGill Physics, Ernest Rutherford Physics Building, McGill University, 3600 rue University, Montréal, QC, H3A 2T8, Canada
[88] National University of Ireland, Department of Experimental Physics, Maynooth, Co. Kildare, Ireland
[89] Nicolaus Copernicus Astronomical Center, Bartycka 18, 00-716 Warsaw, Poland
[90] Niels Bohr Institute, Blegdamsvej 17, 1165 Copenhagen, Denmark
[91] Nordita (Nordic Institute for Theoretical Physics), Roslagstullsbacken 23, 106 91 Stockholm, Sweden
[92] Optical Science Laboratory, University College London, Gower Street, London, UK
[93] SISSA, Astrophysics Sector, via Bonomea 265, 34136 Trieste, Italy
[94] SMARTEST Research Centre, Università degli Studi e-Campus, via Isimbardi 10, 22060 Novedrate (CO), Italy
[95] School of Physics and Astronomy, Cardiff University, Queens Buildings, The Parade, Cardiff, CF24 3AA, UK
[96] School of Physics and Astronomy, University of Nottingham, Nottingham NG7 2RD, UK
[97] Sorbonne Université-UPMC, UMR7095, Institut d'Astrophysique de Paris, 98 bis Boulevard Arago, 75014 Paris, France
[98] Space Research Institute (IKI), Russian Academy of Sciences, Profsoyuznaya Str, 84/32, 117997 Moscow, Russia
[99] Space Sciences Laboratory, University of California, Berkeley, California, USA
[100] Special Astrophysical Observatory, Russian Academy of Sciences, Nizhnij Arkhyz, Zelenchukskiy region, 369167 Karachai-Cherkessian Republic, Russia
[101] Sub-Department of Astrophysics, University of Oxford, Keble Road, Oxford OX1 3RH, UK

[102] The Oskar Klein Centre for Cosmoparticle Physics, Department of Physics, Stockholm University, AlbaNova, 106 91 Stockholm, Sweden
[103] Theory Division, PH-TH, CERN, 1211 Geneva 23, Switzerland
[104] UPMC Univ. Paris 06, UMR7095, 98 bis Boulevard Arago, 75014 Paris, France
[105] Université de Toulouse, UPS-OMP, IRAP, 31028 Toulouse Cedex 4, France
[106] Universities Space Research Association, Stratospheric Observatory for Infrared Astronomy, MS 232-11, Moffett Field, CA 94035, USA
[107] University of Granada, Departamento de Física Teórica y del Cosmos, Facultad de Ciencias, 18071 Granada, Spain
[108] University of Granada, Instituto Carlos I de Física Teórica y Computacional, 18071 Granada, Spain
[109] W. W. Hansen Experimental Physics Laboratory, Kavli Institute for Particle Astrophysics and Cosmology, Department of Physics and SLAC National Accelerator Laboratory, Stanford University, Stanford, CA 94305, USA
[110] Warsaw University Observatory, Aleje Ujazdowskie 4, 00-478 Warszawa, Poland

Appendix A: Simple ILC method

The well-known ILC methods return an image of a component with a known spectrum in the presence of other components whose spectra are either not explicitly considered (Bennett et al. 2003) or only known in a subset of cases (Remazeilles et al. 2011a,b). In Sect. 3 we have the more limited aim of *eliminating* one or two of the major components with known spectra at low frequencies (CMB and free-free emission), and returning a map reasonably close to the sky at 28.4 GHz with these components omitted.

We model the maps as sums of components with spatially-invariant and known spectra, plus noise and other unmodelled foreground emission:

$$\tilde{T}_{jk} = M_{ki} A_{ij} + N_{jk} + O_{jk} \tag{A.1}$$

where the indices are i for component, j for pixel and k for band. A_{ij} is the amplitude. The mixing matrix $M_{ki} = f_i(\nu_k)/U_k C_{ik}$, where $f_i(\nu_k)$ is the spectral form in Rayleigh-Jeans brightness temperature at the band reference frequency ν_k, U_k is the unit conversion from Rayleigh-Jeans to thermodynamic temperature, and C_{ik} is the colour correction (Planck Collaboration IX 2014; Planck Collaboration II 2016)[15]. For the CMB, component 0, we have $M_{k0} = 1$.

Our aim is to find the weights for the frequency maps that satisfy the conditions

$$\sum_k M_{ki} w_k = 0 \tag{A.2}$$

for the components to be eliminated, subject to the normalization condition

$$\sum_k M_{k3} w_k = M_{03} \tag{A.3}$$

where band $k = 0$ is 30 GHz and component $i = 3$ corresponds to a $\beta = -3$ power law, roughly appropriate for synchrotron emission, but also quite close to the effective spectrum of spinning dust. We omit maps with frequencies in the range 50–120 GHz, where the foreground components are weak and their spectrum (especially the dust components) is not well defined. The weakest point of our modelling is the assumption of a fixed spectral shape for the thermal dust, but this component is very weak below 50 GHz so that errors in the dust spectrum there have little effect; the spectrum is mainly used in the interpolation from 353 to 143 GHz needed to generate a dust-cleaned CMB template.

We solve Eqs. (A.2) and (A.3) by restricting the analysis to n frequency maps, where n components are dealt with, to make M_{ki} square, and then

$$\boldsymbol{w} = M^{-1} \begin{pmatrix} 0 \\ \vdots \\ M_{03} \end{pmatrix}. \tag{A.4}$$

In our final application, we have more bands than constraints and so we found the weights by maximizing the S/N for our reference component:

$$S/N = \left(\sum_k w_k M_{k3} \right) \Bigg/ \left(\sum_k w_k^2 \sigma_k^2 \right)^{1/2}, \tag{A.5}$$

where, to keep the weights spatially uniform, we take σ_k^2 as the median pixel variance for band k. We split the bands into a set k' whose weights are varied by the fitting routine (`AMOEBA` in IDL), and a set k whose weights are found by linear regression. Our constraint is now written

$$\sum_k M_{ki} w_k = \delta_{i3} M_{03} - \sum_{k'} M_{k'i} w'_k. \tag{A.6}$$

Each `AMOEBA` iteration provides a trial set of w'_k values that are used to find w_k via

$$w_k = \sum_i M_{ki}^{-1} \left(\delta_{i3} M_{03} - \sum_{k'} M_{k'i} w_{k'} \right), \tag{A.7}$$

and the full set of weights is then used to evaluate the S/N.

[15] Colour corrections and unit conversions for WMAP were derived in the same way as for the LFI, using the released WMAP bandpasses. Colour corrections were based on the spectral index of the model evaluated at ν_k, except that we used the explicit dust colour corrections provided by the `UC_CC` code for the HFI bands (Planck Collaboration IX 2014).